

THE OPTICAL DESIGN OF A VISIBLE ADAPTIVE OPTICS SYSTEM FOR THE  
MAGELLAN TELESCOPE

by

Derek Kopon

---

Copyright © Derek Kopon 2012

A Dissertation Submitted to the Faculty of the

DEPARTMENT OF ASTRONOMY

In Partial Fulfillment of the Requirements

For the Degree of

DOCTOR OF PHILOSOPHY

In the Graduate College

THE UNIVERSITY OF ARIZONA

2012

THE UNIVERSITY OF ARIZONA  
GRADUATE COLLEGE

As members of the Dissertation Committee, we certify that we have read the dissertation  
prepared by Derek Kopon

entitled The Optical Design of a Visible Adaptive Optics System for the Magellan  
Telescope

and recommend that it be accepted as fulfilling the dissertation requirement for the  
Degree of Doctor of Philosophy

\_\_\_\_\_ Date: 9/24/12  
Hubert Martin

\_\_\_\_\_ Date: 9/24/12  
Olivier Guyon

\_\_\_\_\_ Date: 9/24/12  
Josh Eisner

\_\_\_\_\_ Date: 9/24/12  
Glenn Schneider

\_\_\_\_\_ Date: 9/24/12  
Laird Close

Final approval and acceptance of this dissertation is contingent upon the candidate's  
submission of the final copies of the dissertation to the Graduate College.

I hereby certify that I have read this dissertation prepared under my direction and  
recommend that it be accepted as fulfilling the dissertation requirement.

\_\_\_\_\_ Date: 9/24/12  
Dissertation Director: Laird Close

### STATEMENT BY AUTHOR

This dissertation has been submitted in partial fulfillment of requirements for an advanced degree at the University of Arizona and is deposited in the University Library to be made available to borrowers under rules of the Library.

Brief quotations from this dissertation are allowable without special permission, provided that accurate acknowledgment of source is made. Requests for permission for extended quotation from or reproduction of this manuscript in whole or in part may be granted by the copyright holder.

SIGNED: Derek Kopon

## ACKNOWLEDGEMENTS

Many people contributed to making my time at Steward both enjoyable and rewarding. One of my main reasons for leaving private industry and returning to graduate school was because I missed the joy and innate curiosity of people who are motivated primarily by a love of learning and discovery. Everyone creates the atmosphere of scientific inquiry at Steward: the faculty, staff, graduate students, postdocs, and the visitors who pass through for a day or two to share their latest discoveries.

I thank Laird Close, who has been my advisor since I arrived at Steward. Laird is selfless with his time and has a reputation among the graduate students for being an excellent advisor. Laird is generous with his advice, a tireless advocate for his students, and puts a great deal of effort into the student's development not only from an academic and research perspective, but also in their career goals and professional development.

I also thank my mentoring/prelim/thesis committee: Buddy Martin, Josh Eisner, Olivier Guyon, and Glenn Schneider. I am particularly grateful to Buddy Martin who, along with Laird, wrote letters of recommendation for countless scholarship applications, travel grants, and fellowships.

I thank the members of the Magellan AO team: Laird Close, Jared Males, Kate Follette, Katie Morzinski, and Victor Gasho here in Steward; Tyson Hare and Alan Uomoto at Carnegie; Dave Ossip, Povilas Palunas, and the rest of the Magellan telescope staff; and Piero Salinari, Simone Esposito, Armando Ricardi, Marco Xompero, Enrico Pinna, Lorenzo Busoni, Carmelo Arcidiacono, Alfio Puglisi, Runa Briguglio (who gave



me a thrilling ride from the Porta Romana to the Arcetri observatory on the back of his Vespa), and the rest of the staff at Arcetri. Allora, molto grazie!

I thank Michelle Cournoyer for her help over the last five years in navigating the ins and outs of the department and the Graduate College.

I received support from the TRIF Imaging Fellowship, which is administered by the Department of Medical Imaging, and from the SPIE, which awarded me a number of scholarships and travel grants, including the 2009 Price and Smith Optical Design Award. The Magellan AO project also received support from the NSF ATI and TSIP programs.

## DEDICATION

To my family: Mom, Dad, Owen, Colette, my grandparents, and all the rest.

Also to Yervant Terzian, the busiest man in the world who always has time for an undergraduate.

## TABLE OF CONTENTS

LIST OF FIGURES .....	9
LIST OF TABLES .....	12
ABSTRACT .....	13
 CHAPTER 1 INTRODUCTION .....	 15
1.1 Adaptive Secondary Mirrors .....	16
1.2 Enabling Technologies for Visible AO .....	20
1.2.1 Pyramid Wavefront Sensing .....	21
1.2.2 Atmospheric Dispersion Correction .....	22
1.2.3 Spectral Differential Imaging .....	23
1.2.4 Real-Time Frame Selection .....	24
1.3 Tower Testing and Off-Sky Calibration .....	26
1.4 Science Motivations for Visible AO .....	26
1.4.1 Imaging the Surface of Betelgeuse .....	27
 CHAPTER 2 DESIGN, IMPLEMENTATION, AND ON-SKY PERFORMANCE OF AN ADVANCED APOCHROMATIC TRIPLET DISPERSION CORRECTOR FOR THE MAGELLAN ADAPTIVE OPTICS SYSTEM AND VISAO CAMERA ...	 31
2.1 Introduction .....	32
2.2 The Need for an Advanced ADC .....	37
2.3 ADC Design and Analysis .....	38
2.3.1 The 2-Triplet Design .....	38
2.3.2 Pupil Shear .....	44
2.4 Laboratory Performance .....	46
2.5 ADC On-Sky Performance .....	48
2.6 The Zero-Deviation Design .....	50
2.7 Status .....	53
2.8 Conclusion .....	55
2.9 Appendix: Sample ADC Clocking Angle Look-up Tables .....	56
 CHAPTER 3 STATUS UPDATE AND CLOSED-LOOP PERFORMANCE OF THE MAGELLAN ADAPTIVE OPTICS VISAO CAMERA .....	 64
3.1 Introduction: Magellan Simultaneous Visible and IR Adaptive Optics ..	65
3.2 The W-Unit: Pyramid Wavefront Sensing and the VisAO Camera ....	67
3.2.1 Pyramid Wavefront Sensor .....	70
3.2.2 Advanced Triplet ADC .....	72
3.2.3 VisAO Optics .....	74
3.2.4 SDI High-Resolution Imaging .....	77
3.2.5 Coronagraphic Image Plane Spots .....	80
3.3 The Arcetri Tower Tests .....	81
3.4 Results .....	84

3.5	Conclusion .....	86
CHAPTER 4 THE MOVABLE GUIDER PROBE: WIDE-FIELD AND SHACK-HARTMANN GUIDING .....		88
CHAPTER 5 THE CALIBRATION RETURN OPTIC TOWER TEST .....		99
5.1	Test Setup and Design Challenges .....	101
5.2	CRO Cup and Mount Design .....	107
5.3	Gun Laser and Alignment in the Tower .....	109
CHAPTER 6 DESIGN OF A 20 MAS FIBER ARRAY IFS FOR THE VISAO CAMERA .....		112
6.1	Introduction: Magellan Visible Adaptive Optics, Imaging, and IFS ..	112
6.2	The Integral Field Spectrograph Design .....	113
APPENDIX A STRAY LIGHT ANALYSIS AND MITIGATION .....		119
A.1	W-Unit and VisAO Ghosts .....	119
A.2	Baffling .....	120
A.3	Detailed Ghosting Analysis .....	121
APPENDIX B AN ALTERNATIVE WIDE FIELD LENS DESIGN .....		127
APPENDIX C QUARTZ AND CALCITE WOLLASTON DESIGNS .....		134
C.1	Introduction .....	134
C.2	The Quartz Design .....	135
C.3	The Calcite Design .....	137
C.4	Conclusion .....	139
REFERENCES .....		142

## LIST OF FIGURES

1.1	Schematic comparing a typical AO system and an adaptive secondary system .	18
1.2	Photograph of the MMT adaptive secondary mirror . . . . .	19
1.3	Atmospheric chromatic dispersion . . . . .	23
1.4	COAS simulation of the Magellan AO system Strehl ratio at 700 nm . . . . .	25
1.5	H-band contour image reconstruction of Betelgeuse take with IOTA . . . . .	29
2.1	Raytrace of the Magellan Clay telescope . . . . .	33
2.2	The W-unit optical board . . . . .	35
2.3	Raytrace of the VisAO camera . . . . .	36
2.4	Raytrace of the pyramid wavefront sensor . . . . .	37
2.5	Uncorrected atmospheric dispersion at the Magellan focal plane at 50° from zenith . . . . .	41
2.6	The conventional 2-doublet ADC design and our 2-triplet design . . . . .	41
2.7	Comparison of spot diagrams for the 2-doublet design and the 2-triplet design .	42
2.8	Comparison of rms spot size vs. zenith angle for the 2-doublet and 2-triplet designs . . . . .	44
2.9	Chromatic pupil shear as a function of zenith angle . . . . .	45
2.10	Laboratory test setup for verifying the ADC dispersion . . . . .	47
2.11	Theoretical vs. laboratory performance of the triplet ADC . . . . .	48
2.12	On-sky data from the LBT demonstrating the triplet ADC performance . . . . .	50
2.13	Beam deviation as a function of zenith angle for the zero-deviation ADC . . . . .	52
2.14	The ADC in its Arcetri-made actuated rotation mount . . . . .	54
2.15	The mounted ADC integrated into the W-Unit board . . . . .	55
3.1	The Magellan adaptive optics system . . . . .	66
3.2	Diagram of the W-Unit optical board components . . . . .	69
3.3	The PWFS GUI and pupil images . . . . .	71
3.4	Photograph of the fabricated triplet ADC . . . . .	73
3.5	Drawing of the ADC in its rotation mount . . . . .	73
3.6	Photograph of the fully assembled W-Unit . . . . .	76
3.7	Photograph of the quartz Wollaston prism installed in the W-Unit . . . . .	78
3.8	Close-up model of the SDSS and coronagraph/SDI filter wheels . . . . .	79
3.9	Photograph of the coronagraph/SDI wheel with optics installed . . . . .	79
3.10	Drawing of a chrome-on-glass coronagraphic spot . . . . .	80
3.11	Drawing of a second chrome-on-glass coronagraphic spot . . . . .	81
3.12	The Arcetri ASM tower test . . . . .	83
3.13	PSF of closed loop tower test . . . . .	85
3.14	Closed loop performance at 982 nm of the complete AO system in the Arcetri test tower . . . . .	86
4.1	The NAS assembly with the W-Unit and guider probe . . . . .	89
4.2	The guider assembly . . . . .	91

4.3	Ray trace of our custom 50" FOV acquisition camera . . . . .	91
4.4	Spot diagrams of the 50" FOV lens . . . . .	92
4.5	Photograph of the lenses, tube, and filter . . . . .	93
4.6	Photograph of the previous guider with stock SLR lens . . . . .	93
4.7	Drawing of the new guider with custom lens . . . . .	94
4.8	Field curvature and distortion for the wide-field guider lens . . . . .	94
4.9	Wavefront error as a function of field angle for the wide-field guider lens . . . .	95
4.10	Photo of the NAS mounted on the telescope . . . . .	96
4.11	Photo of guider assembly mounted on the telescope . . . . .	97
4.12	Vignetting as a function of field angle for the guider probe . . . . .	98
5.1	Raytrace of the CRO . . . . .	100
5.2	ASM fringes taken with the simultaneous phase measuring interferometer during mirror flattening . . . . .	100
5.3	The Arcetri test tower . . . . .	102
5.4	View from the bottom of the tower to the ASM and CRO . . . . .	103
5.5	The ASM hexapod used in the Arcetri tower and at the LBT . . . . .	104
5.6	Raytrace of the Magellan Gregorian telescope . . . . .	105
5.7	The Magellan ASM mounting structure . . . . .	105
5.8	Model of the ASM and CRO truss assembly . . . . .	106
5.9	5-axis piezo stage . . . . .	108
5.10	Kinematic CRO mounting plates . . . . .	108
5.11	Photograph of the ASM with the CRO truss assembly . . . . .	110
5.12	Rail-mounted gun laser boresight reference and CRO alignment fiducial . . . .	111
5.13	The assembled CRO mount and the gun laser . . . . .	111
6.1	IFS schematic . . . . .	114
6.2	IFS and VisAO block layout . . . . .	115
6.3	Raytrace of IFS and removable triplets . . . . .	116
6.4	Spot diagrams of VisAO IFS focal plane fiber entrance . . . . .	117
6.5	Custom aspheric lenslet design for coupling to the LDSS3 F/11 slit . . . . .	118
A.1	Image taken with coronagraphic occulting spot blocking y-band PSF . . . . .	120
A.2	Example of an out-of-focus ghost at the VisAO focal plane . . . . .	123
B.1	VisAO camera alternative wide-field lens design . . . . .	129
B.2	CCD47 narrow field spot diagrams . . . . .	130
B.3	CCD47 wide-field spot diagrams . . . . .	131
B.4	Footprint diagram of the telescope pupil . . . . .	132
B.5	Vignetting as a function of field angle for the wide field lens . . . . .	133
C.1	Drawing of the principle of Wollaston operation . . . . .	135
C.2	Raytrace of the quartz Wollaston . . . . .	136
C.3	Optical performance of the quartz Wollaston . . . . .	137

C.4	Raytrace of the calcite Wollaston . . . . .	138
C.5	Raytrace of both polatizations through the calcite Wollaston . . . . .	139
C.6	Surface map of one of the calcite Wollastons . . . . .	140
C.7	$H_u$ data showing SDI subtraction . . . . .	141

## LIST OF TABLES

2.1	Triplet ADC optical prescription . . . . .	39
2.2	Zero-deviation triplet ADC optical prescription . . . . .	43
2.3	Calculated ADC clocking angles as a function of airmass . . . . .	52
3.1	VisAO optical components . . . . .	75
A.1	VisAO ghosts . . . . .	123



## ABSTRACT

The Magellan Adaptive Optics system will achieve first light in November of 2012. This AO system contains several subsystems including the 585-actuator concave adaptive secondary mirror, the Calibration Return Optic (CRO) alignment and calibration system, the CLIO 1-5  $\mu\text{m}$  IR science camera, the movable guider camera and active optics assembly, and the W-Unit, which contains both the Pyramid Wavefront Sensor (PWFS) and the VisAO visible science camera. In this dissertation, we present details of the design, fabrication, assembly, alignment, and laboratory performance of the VisAO camera and its optical components. Many of these components required a custom design, such as the Spectral Differential Imaging Wollaston prisms and filters and the coronagraphic spots. One component, the Atmospheric Dispersion Corrector (ADC), required a unique triplet design that had until now never been fabricated and tested on sky. We present the design, laboratory, and on-sky results for our triplet ADC.

We also present details of the CRO test setup and alignment. Because Magellan is a Gregorian telescope, the ASM is a concave ellipsoidal mirror. By simulating a star with a white light point source at the far conjugate, we can create a double-pass test of the whole system without the need for a real on-sky star. This allows us to test the AO system closed loop in the Arcetri test tower at its nominal design focal length and optical conjugates. The CRO test will also allow us to calibrate and verify the system off-sky at the Magellan telescope during commissioning and periodically thereafter.

We present a design for a possible future upgrade path for a new visible Integral Field Spectrograph. By integrating a fiber array bundle at the VisAO focal plane, we can send light to a pre-existing facility spectrograph, such as LDSS3, which will allow 20 mas spatial sampling and  $R \sim 1,800$  spectra over the band 0.6-1.05  $\mu\text{m}$ . This would be the highest spatial resolution IFU to date, either from the ground or in space.

## CHAPTER 1

### INTRODUCTION

From Galileo's first telescope in 1609 to the space telescopes and giant ground-based telescopes of today, it is no exaggeration to say that paradigm shifts in astronomy are driven almost entirely by advances in instrumentation. Astronomy is a science that pushes every technology to its limit. Astronomers want infinite spectral coverage, infinitely fine spatial resolution, and infinite telescope sensitivity. With each increase in capacity in these three areas, new science is achieved and new discoveries are made. High spatial-resolution imaging, which is the topic of this dissertation, is entering a renaissance with complex adaptive optics systems coming on-line that are finally allowing large ground based telescopes to reach their diffraction limit, even in the visible. With each advance in imaging resolution, we can see sharper images of solar system planets, resolve more detail in extended sources such as galaxies, probe further into the inner regions of circumstellar disks, and search closer to host stars for their surrounding planets and low-mass companions.

Until the launch of the Hubble Space Telescope in 1990, all large astronomical telescopes had been ground-based and were limited in their spatial resolution by the seeing limit of the atmosphere. This limit for a very good mountaintop site on a stable night is typically  $\sim 0.5$  arcsec, which is roughly the diffraction limit of a small 20 cm diameter telescope. The 2.4 m diameter Hubble primary, once corrected for spherical aberration, allowed a huge resolution improvement over the atmospheric seeing limit and

enabled all kinds of high-resolution science that was not possible with the atmosphere-limited ground-based telescopes.

In the late 1990s, advances in mirror manufacturing allowed the fabrication of large ( $\geq 6.5$  meter) primary mirrors and the creation of giant ground-based telescopes. Concurrently, advances in computer processor speed and deformable optics technology enabled the first adaptive optics (AO) systems to come on-line on these telescopes. Now, the AO technology has just reached a point where these large telescopes can reach their diffraction limit, surpassing even the exquisite resolution of Hubble. The Magellan Clay telescope is 2.7x times larger than HST and therefore will make images 2.7x sharper at the same  $\lambda$ . However, all the existing (operational) cameras on HST do not Nyquist sample wavelengths less than  $1\mu\text{m}$ . Our VisAO camera makes images  $>4.7\text{x}$  better than HST in terms of pixel resolution. In general, HST will be limited to resolution of  $\sim 60$  mas at best (1.5 pixels FWHM limit to drizzle restoration). On the other hand, we should achieve images with FWHM=18mas at  $0.6\mu\text{m}$  (although at much lower Strehl). We expect that our VisAO camera will make images  $\sim 3.3\text{-}2.7\text{x}$  sharper in FWHM than HST from  $0.6\text{-}1.0\mu\text{m}$  (at the same  $\lambda$  for each) due to our much smaller pixels and larger aperture.

### 1.1 Adaptive Secondary Mirrors

All AO systems require some type of deformable optic capable of introducing aberrations into the wavefront of the telescope in order to cancel the aberrations created by the atmosphere. In many AO systems, this deformable optic is located at a reimaged pupil that is created by adding collimating optics after the focus of the telescope (see Figure

1.1). Because a secondary mirror is already located at a pupil, making the secondary deformable eliminates the need for all of the collimating optics. Having fewer warm surfaces in the optical path significantly reduces the sky background for IR science.

An additional benefit of adaptive secondary mirrors (ASMs) is the finer actuator pitch that is allowed by their large size. The relatively large size of secondary mirrors compared to typical optics located after the telescope focal plane allows for a finer pitch on the pupil. This means that non-contact voice-coil actuated continuous face sheet thin-shell glass mirrors, such as those used at the MMT and the LBT can have sufficient pitch to allow good AO correction, despite the fact that the actual physical actuator pitch is coarser than other deformable mirror (DM) technologies that may use segmented face sheets or stacked piezo actuators. Non-contact continuous face sheet DMs are advantageous because they scatter less light and can still operate close to their nominal performance even with a few dead actuators.

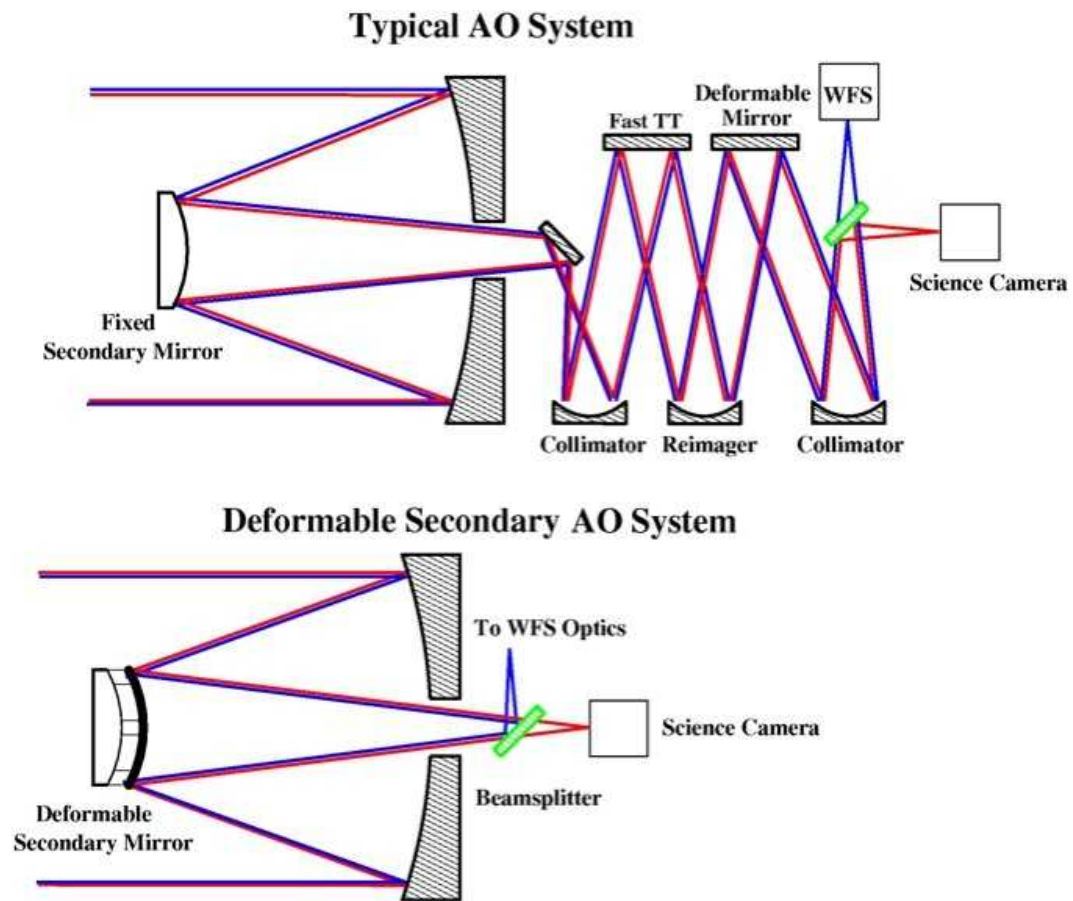


Figure 1.1 Upper figure: schematic of a typical AO system that adds collimating optics and deformable mirrors to the optical path of a telescope. Lower figure: an adaptive secondary mirror eliminates the need for several optical surfaces. By having fewer warm optical surfaces, the infrared noise background of the telescope is greatly reduced. Figure courtesy of Professor Matt Kenworthy, Leiden University.

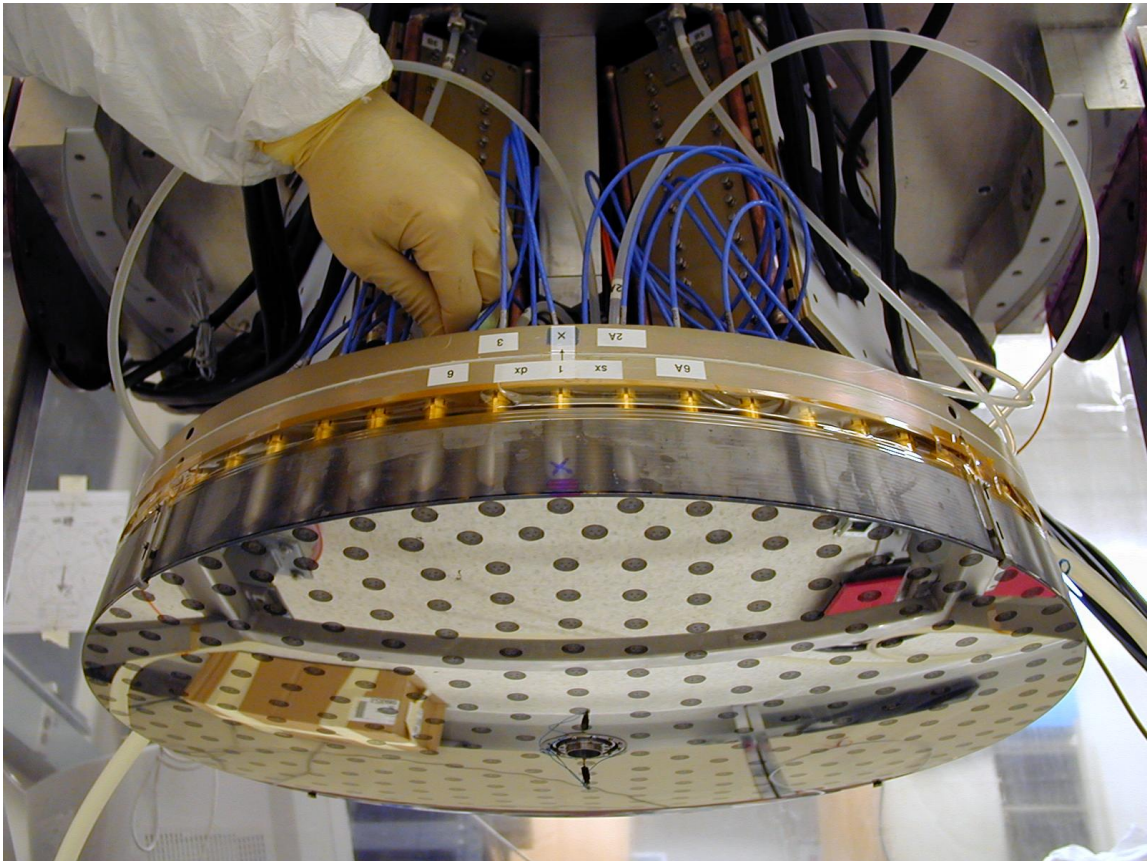


Figure 1.2 The MMT 336 actuator adaptive secondary mirror. Because the MMT is a Cassegrain telescope, the ASM is a convex hyperboloid. The voice coil actuators control the shape of the 2 mm thick thin glass shell that “floats” on a magnetic field approximately 30  $\mu\text{m}$  from the thick glass reference body. Photo courtesy of Guido Brusa.

The first ASM commissioned on-sky is the 336-actuator, 64 cm ASM at the MMT (Figure 1.2), which is regularly used for infrared science with the CLIO (1-5  $\mu\text{m}$ ) and MIRAC4 (8-28  $\mu\text{m}$ ) science instruments. This ASM is a thin-shell (2 mm thick) glass mirror that uses voice-coils to actuate the 336 magnets glued to the back of the shell. See Figure 1.2.

The second generation thin-shell ASM came on-sky in 2010 at the LBT. This shell is thinner (1.5 mm compared to 2 mm), which allows more deflection for an equivalent

voice coil actuator force. The LBT shell has more actuators (672 compared to 336) and a larger diameter (91 cm diameter compared to 64 cm). In addition, the LBT adaptive secondary is a concave ellipsoid because of the Gregorian design of the LBT. This concave shape allows a retroreflecting optic to be placed at the intermediate focus of the telescope in order to enable off-sky testing, something not possible with the MMT ASM.

The Magellan AO system is a virtual clone of the LBT system, with the same optical prescription for the ASM, similar wavefront sensor, and the same core real-time control software and hardware. The Magellan ASM has a slightly smaller diameter (85 cm) and therefore fewer actuators (585), but the actuator pitch in the pupil at Magellan is actually slightly finer than the LBT.

Because of this advantageous actuator spacing, the excellent seeing at the Magellan site (0.8'' or better 75% of the time), and other enabling characteristics of the Magellan AO system (MagAO), we have designed and built the VisAO camera, which has several unique attributes. In particular this camera will achieve excellent high-resolution imaging over the band 500-1000 nm (unlike most AO cameras which only work in the lower resolution infrared). The VisAO camera is the main focus of this dissertation.

## 1.2 Enabling Technologies for Visible AO

In general, from an AO instrumentation perspective, everything is more difficult at shorter wavelengths. Optical alignment is less forgiving, telescope jitter is more significant, wavefront sensing must be more precise, actuator response time must be faster, etc. For all of these reasons, AO at visible wavelengths has historically been very



difficult. This dissertation and Kopon et al. 2009 discuss some of the enabling technologies that will allow VisAO to push to these shorter wavelengths.

### 1.2.1 Pyramid Wavefront Sensing

The pyramid wavefront sensor (PWFS) is very important for visible AO because of its potential for diffraction-limited performance and variable sensitivity. A Shack-Hartmann (SH) sensor is diffraction-limited by the size of a pupil sub- aperture, i.e. the pitch of the lenslet array. The PWFS uses the full pupil aperture and is only diffraction-limited by the size of the primary mirror. Since the wavefront sensing wavelengths are essentially the same as the science wavelengths ( $\sim 0.7 \mu\text{m}$ ), it is essential that the wavefront sensor be as close to the diffraction limit as possible (Esposito et al. 2000).

Another advantage of the PWFS that makes it crucial for visible AO is the dynamic range provided by the modulation of the piezo fast steering mirror. The fast steering mirror is located very close to the pupil and is used to scan (in a circle) the image of the guide star around the tip of the pyramid. The amplitude of this scan can be adjusted to a large value for a highly aberrated wavefront and a smaller value for a partially corrected wavefront. As wavefront correction becomes better, the amplitude of the scan can be decreased in order to increase sensitivity. This is in contrast to a SH sensor, whose sensitivity is essentially fixed by the lenslet pitch (but can be degraded by bad seeing). The dynamic range provided by the PWFS should allow us to use  $\sim 2$  mag fainter guide stars than would be allowed by the SH sensor, in addition to allowing us to come very close to diffraction-limited correction (Esposito et al. 2001).

Because we intend to observe at least part of the time at the same wavelengths at which the PWFS operates, we will be reducing the modulation radius of the guide star around the pyramid tip to close to  $\sim\lambda/D$ . At this tight radius, any amount of atmospheric dispersion that is greater than the diffraction limit at the wavefront sensing wavelengths will cause the spot to elongate, with different parts of the spot hitting different facets of the pyramid during the modulation. Avoiding this source of error is one consideration driving our Atmospheric Dispersion Corrector design, which will improve our PWFS performance in addition to enabling visible AO science.

### 1.2.2 Atmospheric Dispersion Correction

Atmospheric dispersion is the variation of index of refraction as a function of wavelength for light traveling through the atmosphere at an oblique angle (Figure 1.3). Atmospheric dispersion is zero for a star directly overhead and is at a maximum for a star just above the horizon, traveling through the atmosphere at a steep angle. This effect is a function of temperature, humidity, elevation, and pressure. In our design work, we used a special surface in our Zemax optical model in order to simulate the effect of the atmospheric dispersion.

While atmospheric dispersion can be an issue at IR wavelengths, it is much more significant at visible wavelengths. Completely ignoring the effect over the band 500-1000 nm will result in an elongation of the VisAO PSF of 1.3 arcsec (compared to the first Airy minimum radius of 20 mas at 500 nm). Therefore this effect will prevent any sort of diffraction-limited imaging in the visible over any appreciable wavelength band.

Because we are both wavefront sensing (very broad band) and performing AO science at visible wavelength, it is doubly important that we understand and correct for this effect. In Chapter 2, we present our unique triplet atmospheric dispersion corrector, which outperforms conventional designs by  $\sim 56\%$  in rms spot size. This design has been fabricated and tested on-sky.

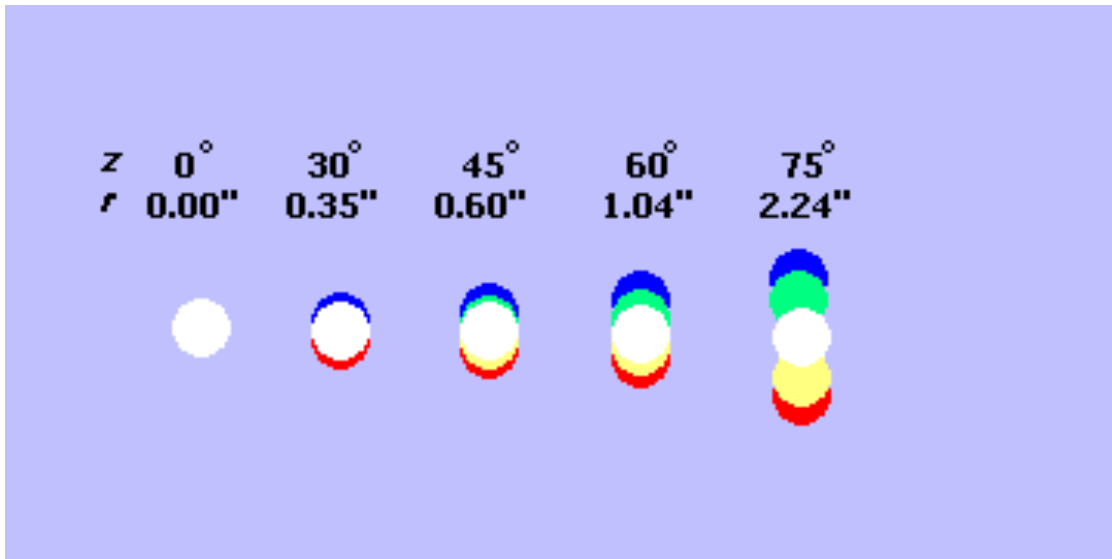


Figure 1.3 Atmospheric chromatic dispersion elongates the PSF as a function of zenith angle. Figure from: [http://exoplanet.as.arizona.edu/~lclose/a302/lecture5/Lecture\\_5.html](http://exoplanet.as.arizona.edu/~lclose/a302/lecture5/Lecture_5.html)

### 1.2.3 Spectral Differential Imaging

For science cases involving imaging in a specific visible spectral line, a powerful technique for noise suppression and speckle mitigation is Spectral Differential Imaging (see Close et al. 2005, Marois et al. 2006, Biller et al. 2007). This technique involves splitting the unpolarized science beam into two images of orthogonal (o and e) polarizations using a Wollaston prism. The two beams travel virtually the same optical path, thereby minimizing non-common path aberrations (and space on the optical bench).

Just before the focal plane, one beam passes through a narrow band filter centered on the spectral line of interest and the other passes through a narrow band filter of equivalent spectral width centered on a wavelength just off of the wavelength of interest (i.e. a continuum wavelength). These two images are then subtracted and the remaining image should be free of speckles and other broadband noise sources.

In Chapter 3 we discuss SDI in the context of the VisAO camera. We also include the details of our Wollaston optical designs in Appendix D.

#### 1.2.4 Real-Time Frame Selection

An important enabling technology for diffraction limited AO imaging in the visible is the real-time frame selection (RTFS) technology developed by Jared Males (Males et al. 2012, Males et al. 2010, Kopon et al. 2009). This technique will not be discussed further in this dissertation, but is an important capability of the VisAO camera. The CAOS AO simulations of the Magellan system performed by Males show a strong temporal variability in our expected visible Strehl ratio. Over a few hundred millisecond, the Strehl can vary as high as 40% and as low as 5% (see Figure 1.4). Some groups have attempted to overcome the blurring effect of these periods of low Strehl by reading out their CCD faster than the time scale of the variation and then shifting and adding the good images. However, this technique, known as Lucky Imaging, comes with requisite read noise hit associated from reading the CCD out so quickly (see, for example, Law et al. 2009).

Males et al. have developed a fast asynchronous shutter that is located in front of the VisAO detector that will block periods of low Strehl light using AO telemetry to predict periods of low and high Strehl (Figure 1.4). This technique will allow us to only

integrate on the high-Strehl light, while avoiding the read-noise hit of Lucky Imaging techniques.

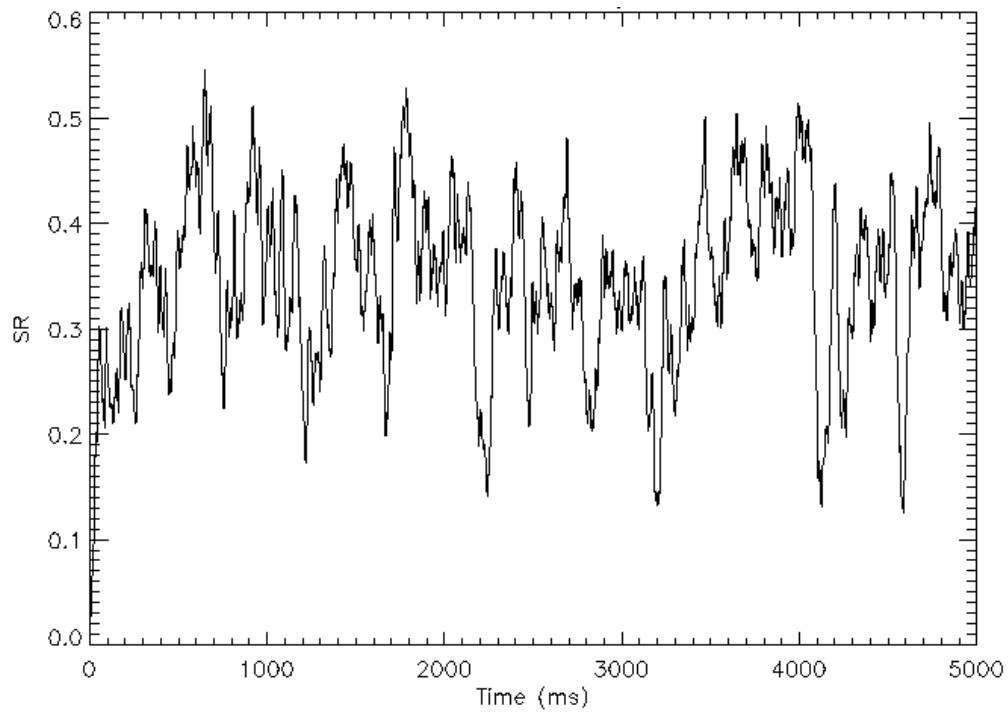


Figure 1.4 COAS simulation of the Magellan AO system Strehl ratio at 700 nm performed by Jared Males (figure taken from Kopon et al. 2009). The Strehl ratio (SR) varies significantly over time scales of 100's of milliseconds.

### 1.3 Tower Testing and Off-Sky Calibration

As mentioned earlier, one of the major drawbacks of the MMT first-generation ASM is that its convex shape prevents any sort of off-sky calibration. A real star is needed to illuminate the ASM and the wavefront sensor. Because the ASM can only be illuminated by an actual star, its performance cannot be measured without atmospheric turbulence as part of the test.

The LBT, the Magellan telescope, and future giant telescopes, such as the GMT, use concave secondaries with intermediate foci. This configuration allows an off-sky double-pass optical test to be performed by placing a calibration point source at the far focal plane and a retroreflecting optic at the intermediate focal plane. However, this test requires extremely sensitive alignment over a very large optical path. In Chapter 5 we present the details of our alignment techniques and engineering solutions to performing this test.

### 1.4 Science Motivations for Visible AO

There are many science cases that motivate the push towards high-resolution AO imaging at shorter wavelengths ( $500 \text{ nm} < \lambda < 1000 \text{ nm}$ ). The Magellan AO system is a single natural guide star system and will therefore have very good resolution over a small ( $\sim 8$  arcsec) field of view, limited by isoplanatism. Therefore, the main science cases are those that provide a bright guide star within the narrow field of view and benefit from high angular resolution.

Folette et al. 2010 discusses several of these science cases in detail, in addition to discussing the advantages of an Integral Field Spectrograph upgrade to the VisAO

camera at some point in the future. We discuss one possible upgrade design in Chapter 6. Some of the science cases that we are developing for the VisAO camera include: imaging the surface of nearby supergiants, such as Betelgeuse; imaging the inner regions of circumstellar disks; and imaging solar system objects such as Titan's atmosphere or asteroids. The future IFS upgrade (which is the planned focus of a future NSF proposal) will allow us to resolve the spectra of tight ( $\sim 0.02''$ ) astrometric binaries, study the forbidden line region of Herbig Ae/Be stars, study the kinematics of nearby AGN and their surrounding stellar populations, and many other cases.

#### 1.4.1 Imaging the Surface of Betelgeuse

The red supergiant Betelgeuse has an angular diameter in the optical of  $\sim 43$  mas (Perrin et al., 2004). When compared to the 8.5 mas pixels of our VisAO CCD47, this makes it an excellent candidate for direct imaging using a narrow band filter and possibly Spectral Differential Imaging (SDI). Because of its large angular diameter and brightness (R-band magnitude  $\sim -1$ ), Betelgeuse has historically been a favorite target for optical and near-IR interferometry (Haubois et al. 2009 or Young et al. 1992, for example) and non-redundant aperture masking on large-aperture telescopes (Wilson et al. 1992). These techniques have consistently measured an angular diameter on the order of  $\sim 45$ -55 mas, depending on wavelength and the variation in diameter due to stellar variability. They have also consistently measured hot spots on the stellar surface, generally numbering 1-3, that vary in brightness, number, and location over time scales of months (Young et al. 2000). These hot spots typically account for 15-20% of the total flux in the visible. The generally accepted interpretation is that these hot spots are associated with large-scale

convective phenomena (Schwarzschild, 1975). However, recent studies show that the variation of spot brightness as a function of wavelength may be inconsistent with simply modeling the spots as regions of higher temperature, as predicted by models of convective cells (Young et al. 2000).

While almost all recent interferometric and aperture masking studies show the existence of these bright spots, many of them obtain different results for the number, location, or brightness of these features, either because the features have changed over time or because of the difference in observational techniques and sensitivities. It is difficult to piece all of these studies together into a coherent picture because of their wide variation in wavelength, angular resolution, observation technique, and data reduction method. Part of the reason for this lack of continuity in the monitoring of the surface features of Betelgeuse is the effort involved in imaging a stellar surface using interferometry. For instance, recent imaging of the surface of Betelgeuse in H-band with IOTA required 6 nights using 5 different interferometer configurations in order to get sufficient uv coverage (Figure 1.5). The IOTA instrument has since been disassembled.



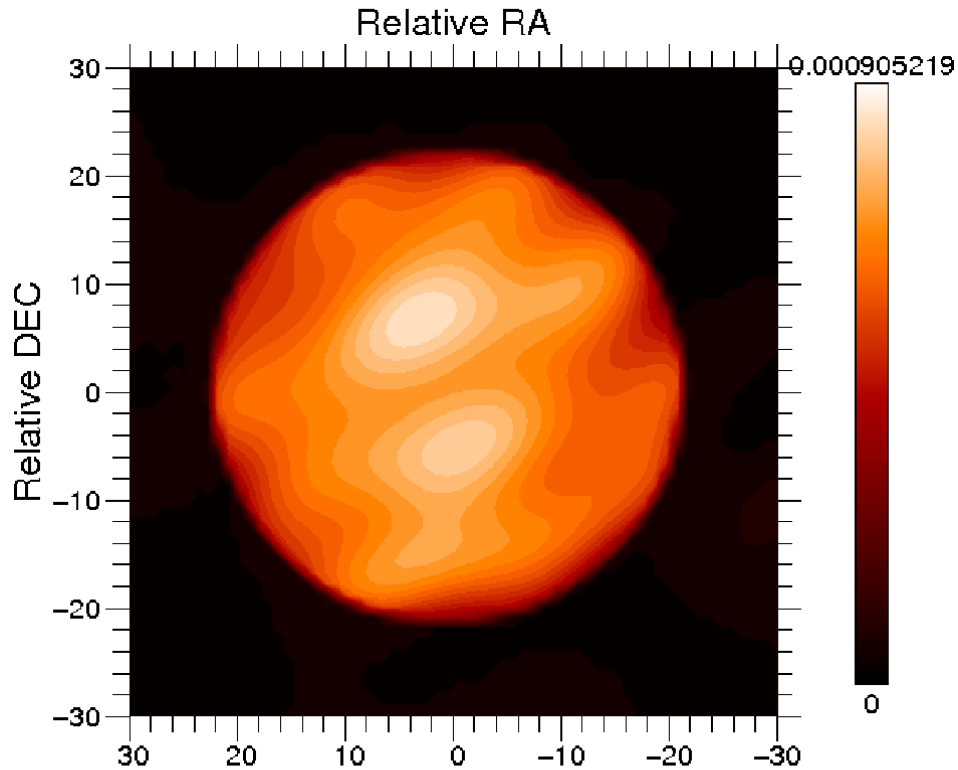


Figure 1.5 H-band contour image reconstruction of the surface of Betelgeuse taken with the IOTA interferometer. The brighter of the two spots has an estimated angular diameter of 11 mas, which is the same order of magnitude as the resolution limit of the interferometer. The fainter of the two spots is unresolved. Figure taken from Habois et al., 2009.

There is strong evidence that these surface bright spots vary in brightness and location over the course of months. There is also strong evidence that the brightness of these spots relative to the rest of the stellar surface varies with wavelength in a manner that may be inconsistent with a thermal distribution. Observations made with the COAST interferometer at 700, 905, and 1290 nm show strong surface features in the visible, but a smooth symmetric disk in the near-IR (Young et al. 2000). However, later observations at H-band with IOTA show two strong spots, one with an estimated angular

diameter of  $\sim 11$  mas, the other unresolved. To achieve a more consistent understanding of the nature of these bright spots, what is called for is a monitoring campaign with a sampling cadence on the order of months at multiple wavelengths with consistent observational techniques.

The Magellan AO VisAO camera is ideally suited for this task. With an appropriately chosen neutral density filter and the use of the fast shutter, an image of the surface of Betelgeuse can be taken in a matter of seconds. Multiple narrow band filters can provide spectral coverage from  $\sim 500$ - $1000$  nm. While the highest resolution interferometers have better resolution than VisAO (IOTA achieved 11 mas resolution at H-band in its highest resolution configuration with a 38 meter baseline), the broad visible wavelength coverage, ease of use, and short integration time make our 8.5 mas pixels and  $\sim 22$  mas resolution at 700 nm very competitive. With multiple Magellan AO runs planned per year, a multiyear monitoring campaign with images at multiple wavelengths could yield valuable information about the nature and dynamical timescale of these brightness features.

## CHAPTER 2

### DESIGN, IMPLEMENTATION, AND ON-SKY PERFORMANCE OF AN ADVANCED APOCHROMATIC TRIPLET DISPERSION CORRECTOR FOR THE MAGELLAN ADAPTIVE OPTICS SYSTEM AND VISAO CAMERA

*This chapter contains work that was submitted for publication in the Publication of the Astronomical Society of the Pacific in June of 2012 and work that was published by Kopon, et al. in the 2008 Proceedings of the SPIE. The Zero-Deviation design is also described in provisional patent UA 11-085 “Zero-Deviation Advanced Triplet Atmospheric Dispersion Corrector.” All optical designs and analysis presented in this paper are the original work of the author, with the exception of the Arcetri 2-doublet ADC design, the pyramid wavefront sensor, and the Magellan telescope.*

We present the novel design, laboratory verification, and on-sky performance of our Triplet Atmospheric Dispersion Corrector (ADC), which is an important component of the Magellan Adaptive Optics system, scheduled for first light on the Magellan Telescope in late 2012. High-precision broadband atmospheric dispersion correction at visible wavelengths is essential both for wavefront sensing on fainter guide stars, and for performing visible AO science using our VisAO camera. Comparing broadband rms on-axis spot size, our unique triplet design performs 58% better over the wavelength band 500-1000 nm at high (1.6) airmass than conventional doublet designs. This design has

been fabricated, tested in the lab, and integrated into the VisAO system, which recently completed final system tests and pre-ship review at the Arectri Observatory in Florence, Italy. We present on-sky results of the ADC in operation with the LBT AO system. We also present the design of a zero-beam-deviation triplet ADC, which will be important to future AO systems that require precise alignment of the optical axis at all airmasses in addition to excellent dispersion correction. Until now, the 1<sup>st</sup>-order chromatic correction of conventional doublet designs has been sufficient because AO systems were not yet at the point where they could approach the visible diffraction limit on large telescopes. However, now that AO systems are approaching that limit, our apochromatic (2<sup>nd</sup>-order chromatic correction) is needed.

## 2.1 Introduction

Current adaptive optics (AO) imaging systems on large ground-based telescopes are just now approaching truly diffraction-limited high-Strehl ( $\sim 40\%$  at  $i'$ -band) performance in the visible and near-IR bands (Close et al. 2010). Consequently, heretofore-ignored effects, such as secondary color caused by atmospheric dispersion, will need to be mitigated very precisely. Many of the science cases for ground-based diffraction-limited imaging are photon-starved (such as the imaging of faint circumstellar dust disks or the detection of faint extrasolar planets), thereby driving the need for broadband imaging. To achieve these goals, current 8-meter class and future 30-meter class telescopes will require excellent broadband chromatic performance (Goncharov et al. 2007). Additionally, increased sky coverage can be achieved if AO can be performed on fainter

guide stars, thereby also driving the need for dispersion correction to enable broadband wavefront sensing.

The Magellan Clay Telescope is a 6.5-meter Gregorian telescope located in Las Campanas Observatory in Chile (Figure 2.1). The Magellan AO system consists of an 850 mm diameter thin (1.6 mm) shell adaptive secondary mirror with 585 actuators, a pyramid wavefront sensor (PWFS), an infrared science camera (either the BLINC-MIRAC4 10  $\mu\text{m}$  camera (Skemer et al. 2009) or the CLIO 5  $\mu\text{m}$  camera (Sivanandam et al. 2006), depending on the science case), and our VisAO visible (500-1000 nm) science

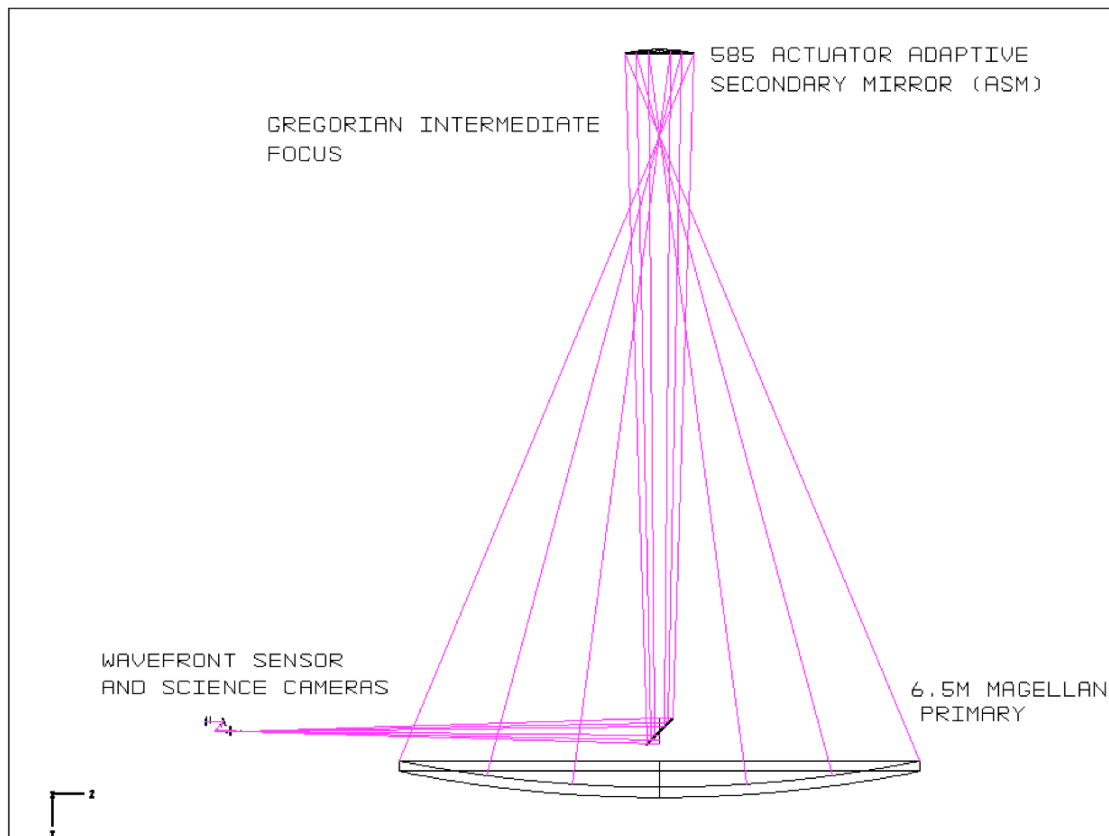


Figure 2.1 The raytrace of the Magellan Clay telescope showing the 6.5 m primary mirror, the deformable adaptive secondary mirror, and the focal plane instruments, including the PWFS, VisAO camera, and infrared science camera.

CCD camera (Kopon et al. 2009 and 2012, Males et al. 2012). The secondary mirror and wavefront sensor are the same in design and optical prescription as those of the LBT (Esposito et al. 2010). A dichroic beamsplitter located before the Nasmyth focus allows us to simultaneously perform IR and visible science. The ADC provides common path chromatic correction on the visible light beam for both the pyramid wavefront sensor and the VisAO science camera. For more information on the Magellan AO system see Close et al. (2012).

The PWFS and VisAO camera are both mounted on the same optical board called the W-unit (Figure 2.2), which receives visible light from the dichroic (Kopon et al. 2009). The W-unit is mounted on a stable and precise 3-axis stage that patrols a 2.3' x 3.2' field of view on the sky in order to acquire guide stars. Incoming light passes through a triplet input lens that changes the beam from diverging F/16 to converging F/49. This beam then passes through the ADC before hitting a beamsplitter/dichroic wheel. The transmitted light from the beamsplitter goes to the PWFS and the reflected light goes to the VisAO camera. Figures 2.3 and 2.4 show the raytraces for the VisAO science arm and the PWFS arm of the W-unit.

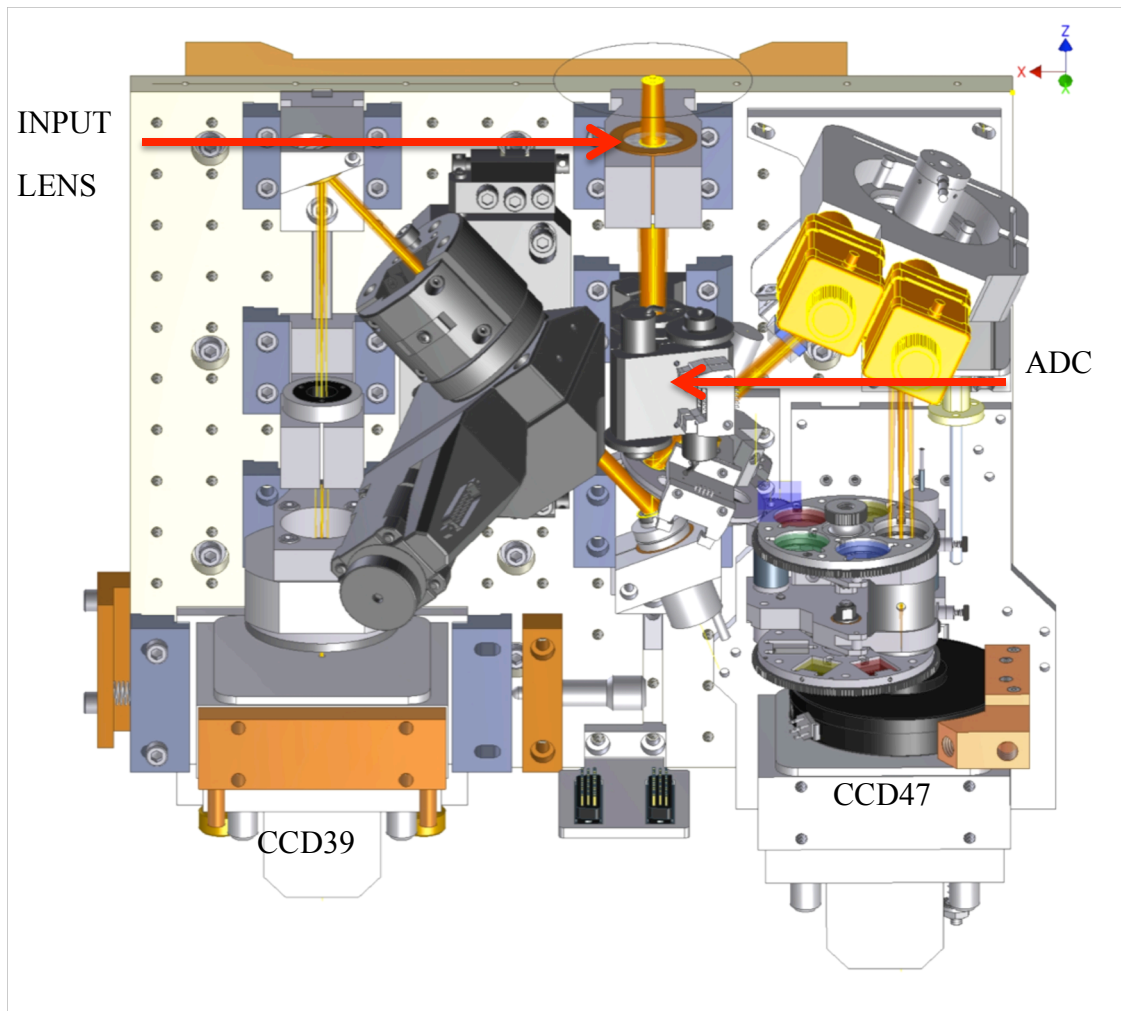


Figure 2.2 The W-Unit optical board. This board contains both the VisAO science camera and the PWFS and can patrol a  $2.3 \times 3.2$  arcmin FOV to acquire science targets and guide stars. The incoming beam from the telescope enters through the triplet input lens at the top of the figure and then passes through the ADC before being split into two channels.

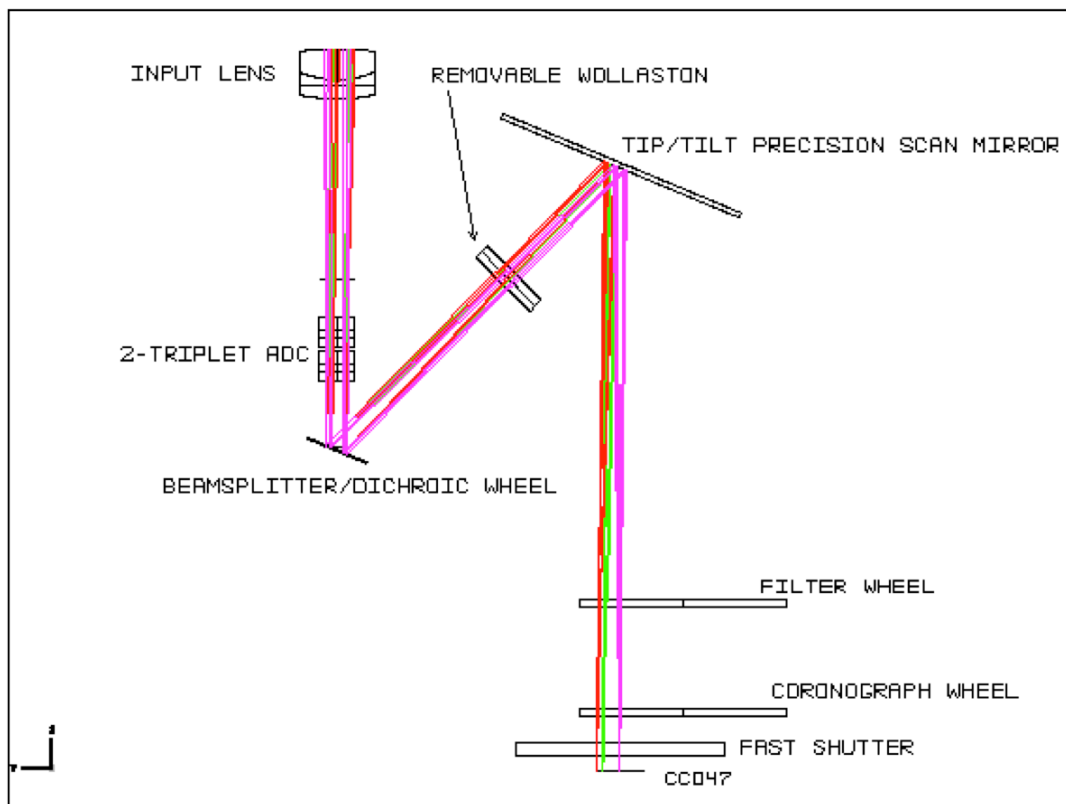


Figure 2.3 The raytrace for the VisAO camera. Light from the F/16 telescope focus passes through the telecentric lens (not shown) and then through a triplet lens at the front of the W-unit optical board. Light reflected by the selectable beamsplitter travels to the CCD47 for visible AO science.



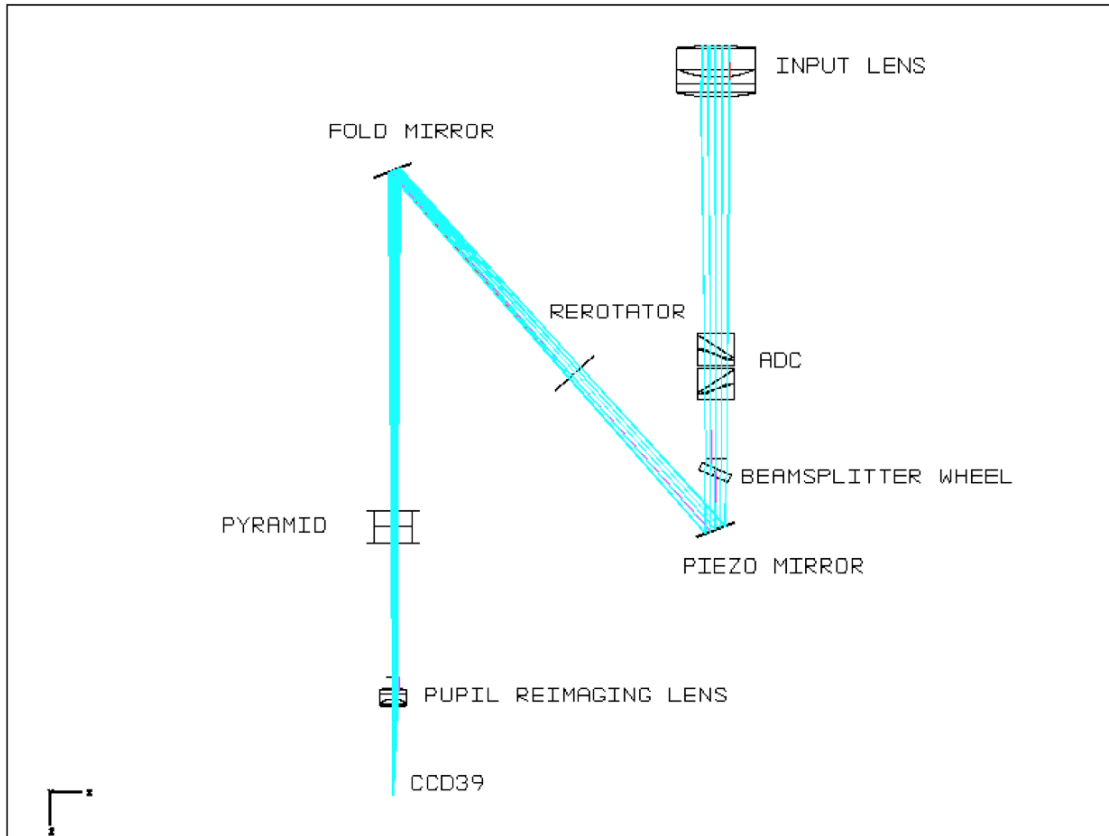


Figure 2.4 The raytrace for the PWFS. The VisAO camera and the PWFS share the triplet lens and the ADC in common. Then light transmitted by the beamsplitter travels to the PWFS and the CCD39.

## 2.2 The Need for an Advanced ADC

The atmospheric dispersion is egregious over the band 500-1000 nm resulting in a PSF that is diffraction-limited (20-40 mas) in the direction parallel to the horizon and 1.3 arcsec in the perpendicular direction (Figure 2.5) at 50° from zenith (1.55 airmass). The mitigation of this dispersion is essential for both wavefront sensing and visible AO science. Traditional linear or 2-doublet ADC designs (also known as Amici prisms) can significantly reduce this 2000  $\mu\text{m}$  of lateral color by correcting primary color (see for

example Phillips et al. 2006 or Wynne 1997), but still do not reach the diffraction limit because of secondary and higher order lateral color (Wallner et al. 1980).

The PWFS is a method of wavefront sensing (Esposito et al. 2000) that has significant advantages over conventional methods such as the Shack-Hartmann sensor or the curvature sensor (Roddier et al. 1988). The PWFS operates by using a fast piezo scan mirror to circularly modulate an image of the guide star around the tip of a 4-sided optical pyramid that is located at the F/49 focal plane. Light passes through each side of the pyramid and forms 4 pupil images in the quadrants of the PWFS CCD detector. By changing the radius of modulation down to  $2 \lambda/D$  (for bright stars) and/or binning the CCD from 28x28 pix/pupil diameter to as low as 4x4 pix/pupil diameter for faint stars, the dynamic range of the PWFS (R mag of -2 to +16) can be easily adjusted based on the science case and guide star magnitude. This is a significant advantage over the Shack-Hartmann method, which has a spatial sampling (and hence a limiting magnitude) fixed by the lenslet pitch. A modulation radius approaching 2 FWHM of the diffraction-limited star image is necessary in order to take full advantage of the dynamic range of the pyramid sensor. This requires a high-performance ADC, which enables finer broadband wavefront sensing on fainter guide stars than would otherwise have been possible at moderate airmasses.

## 2.3 ADC Design and Analysis

### 2.3.1 The 2-Triplet Design

Most ADCs designed and built to date consist of two identical counter-rotating prism doublets made of a crown and flint glass (Wynne 1997), also known as Amici prisms, or

zero-deviation prisms. One method of designing a conventional 2-doublet ADC in the visible band is to match the d-light (587 nm) indices of the two glasses as closely as possible in order to avoid steering the beam away from its incident direction. The wedge angles and glasses of the prisms are chosen to correct primary chromatic aberration at the most extreme design zenith angle. By then rotating the two doublets relative to each other, an arbitrary amount of first-order chromatic aberration can be added to the beam to cancel the dispersive effects of the atmosphere at a given zenith angle. The 2-doublet design corrects the atmospheric dispersion so that the longest and shortest wavelengths overlap each other, thereby correcting the primary chromatism. Second order chromatism is not corrected and is the dominant source of error at higher zenith angles.

**Table 2.1**  
**Doublet ADC Optical Prescription**

Surface	Thickness (mm)	Glass	Tilt Angle (deg)
1	4	C04-64 (Corning)	0
2	4	BAM23 (OHARA)	28.81
3	...	...	0

The 2-Doublet design that we compare our performance to is that initially designed by the Arcetri group for use with the LBT AO system. The prescription for this design is presented in Table 2.1. The glasses used in this design, Corning's c04-64 and Ohara's BAM23 (at present time these have become obsolete glasses and are no longer in

production), are very well matched, with d-light indices of 1.6035 and 1.6072, respectively. The Abbe numbers are very well matched to be symmetrically on either side of 50:  $V_d = 63.402$  for c04-64 and  $V_d = 40.263$  for BAM23. This doublet design corrects first-order chromatism over the design wavelengths very well and is close to an optimal doublet ADC design with well-chosen glasses. To correct higher orders of chromatism, more glasses and thereby more degrees of freedom are needed.

A great deal of effort was put into optimizing glass choice for our triplet design. We performed a Zemax glass substitution optimization that entailed swapping glass in and out and then optimizing the wedge angles to minimize rms spot size at the maximum design zenith angle. Some designs were then discarded because the beam deviation was too large, or the required wedge angles were too large to realistically fabricate without very thick ADCs. The three glass we ultimately chose for our design were Ohara's S-PHM53 (crown), S-TIM8 (flint), and Schott's N-KZFS4 (anomalous dispersion). These glasses have some of the best matched indices of any triplet pair we were able to find in the glass catalogue, with  $n_d = 1.603$ ,  $1.596$ , and  $1.613$ , respectively. The Abbe numbers are also well matched, with  $V = 65.44$ ,  $39.24$ , and  $44.49$ , respectively. The N-KZFS4 has one of the highest anomalous dispersion figures of merit in the glass catalogue. The figure of merit used in Zemax is the  $DP_{g,F}$  value, which measures the deviation of the partial dispersion versus Abbe number from the "normal" line, which fits most glasses. N-KZFS4 has  $DP_{g,F} = -0.01$ , compared to  $.0045$  and  $.0023$  for S-PHM53 and S-TIM8, respectively. For more on anomalous dispersion definitions and glass choice, see <http://www.radiantzemax.com/kb-en/KnowledgebaseArticle50231.aspx>.

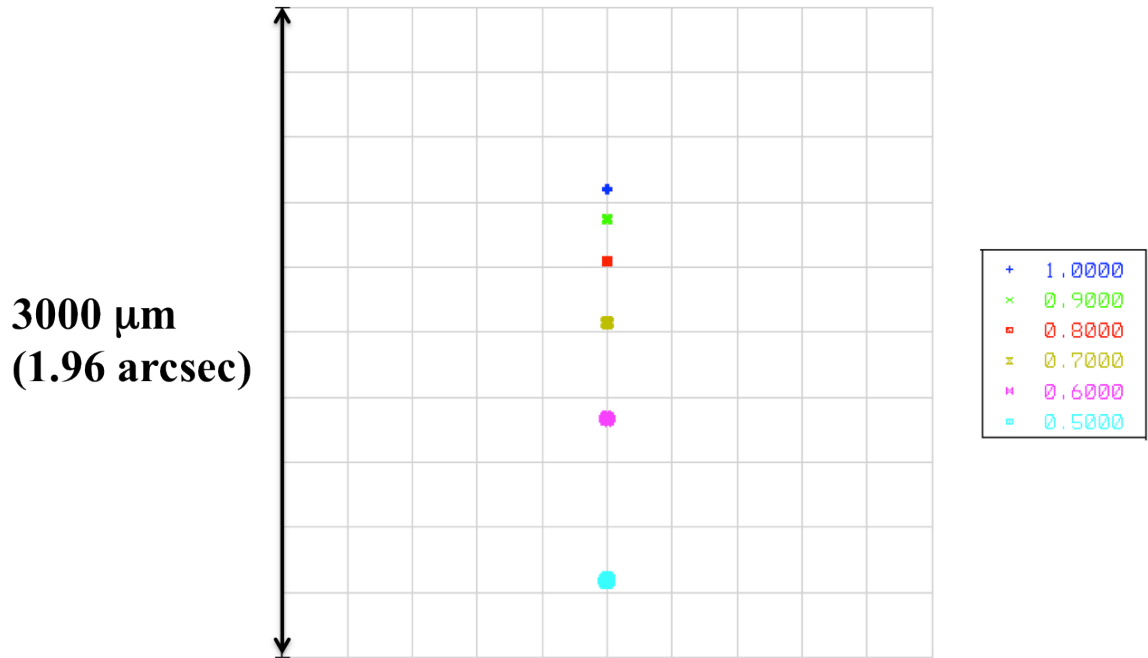


Figure 2.5 Uncorrected atmospheric dispersion at the Magellan focal plane at  $50^\circ$  from zenith (1.55 airmass) over the band 0.5-1.0  $\mu\text{m}$ . The PSF is diffraction-limited in the horizontal direction (20-40 mas) and 1.3 arcsec long in the other. The PWFS would fail to work well on faint stars at this airmass without an ADC. Units are microns with a plate scale of 0.654 mas/ $\mu\text{m}$ .

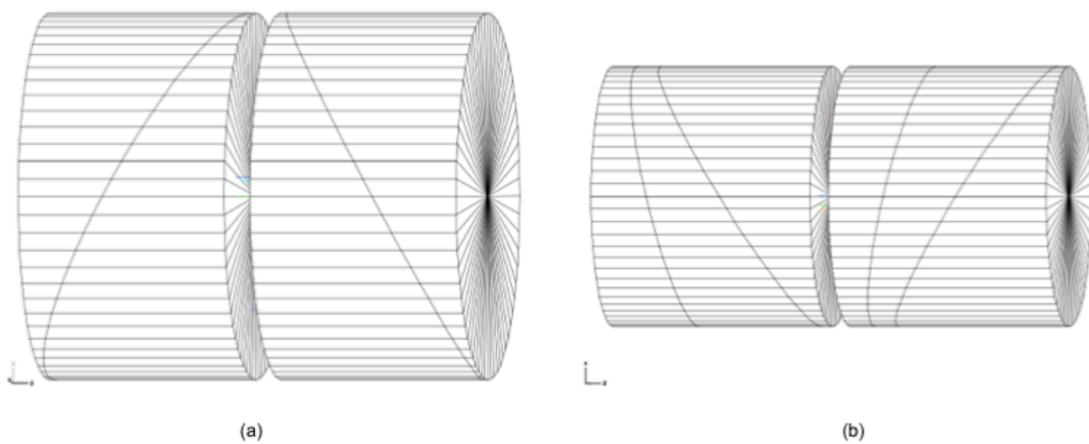


Figure 2.6 (a) The conventional 2-doublet “Amici Prism.” (b) Our 2-triplet design.

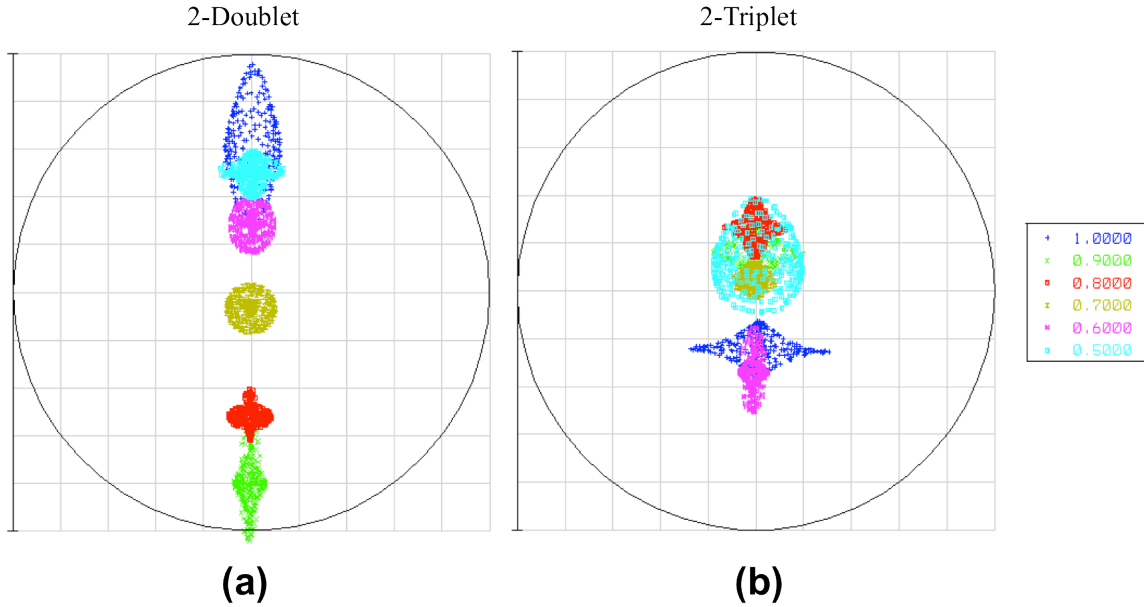


Figure 2.7 (a) Spot diagram of the conventional 2-douplet design over the band 0.5-1.0 microns at  $50^\circ$  from zenith. The longest and shortest wavelengths overlap indicating that primary chromatism is well corrected. (b) Spot diagram of our 2-triplet design at the same wavelengths and zenith angle. Both primary and secondary chromatism are corrected, giving a 56% improvement in rms spot size over the full wavelength band. The circle shows the first airy minimum in the diffraction limit at 500 nm: 39 mas, which is  $59.86 \mu\text{m}$  at the F/49 VisAO focal plane.

In our 2-triplet design (Kopon et al. 2008), a third glass with anomalous dispersion characteristics (Schott's N-KZFS4) is added to the crown/flint pair. Like the doublet, the index of the anomalous dispersion glass was matched as closely as possible to that of the crown and flint. See Table 2.2 for the optical prescription of our as-made triplet ADC. The Zemax optical design software has the ability to simulate the chromatic effects of the atmosphere by placing a model optical surface in front of the Magellan Clay telescope design. This surface simulates atmospheric dispersion with adjustable input parameters for Zenith angle, temperature, elevation, atmospheric pressure, humidity, etc. In our design process, the atmospheric surface was set to  $70^\circ$  zenith angle and the relative

angles of the ADC were set to  $180^\circ$ . The wedge angles of the three prisms in the triplet were then optimized to correct both primary and secondary color over the full wavelength band.

Figure 2.8 shows the relative performance of the 2-doublet and 2-triplet designs. The spike at  $0^\circ$  zenith angle is a result of the residual chromatism of the ADC having no atmospheric dispersion to balance. We observed this zenith spike effect in the lab with the fully assembled VisAO camera.

**Table 2.2**  
**Triplet ADC Optical Prescription**

Surface	Thickness (mm)	Glass	Tilt Angle (deg)
1	5	S-PHM53 (OHARA)	0
2	3	S-TIM8 (OHARA)	32.21
3	4	N-KZFS4 (SCHOTT)	24.51
4	...	...	0

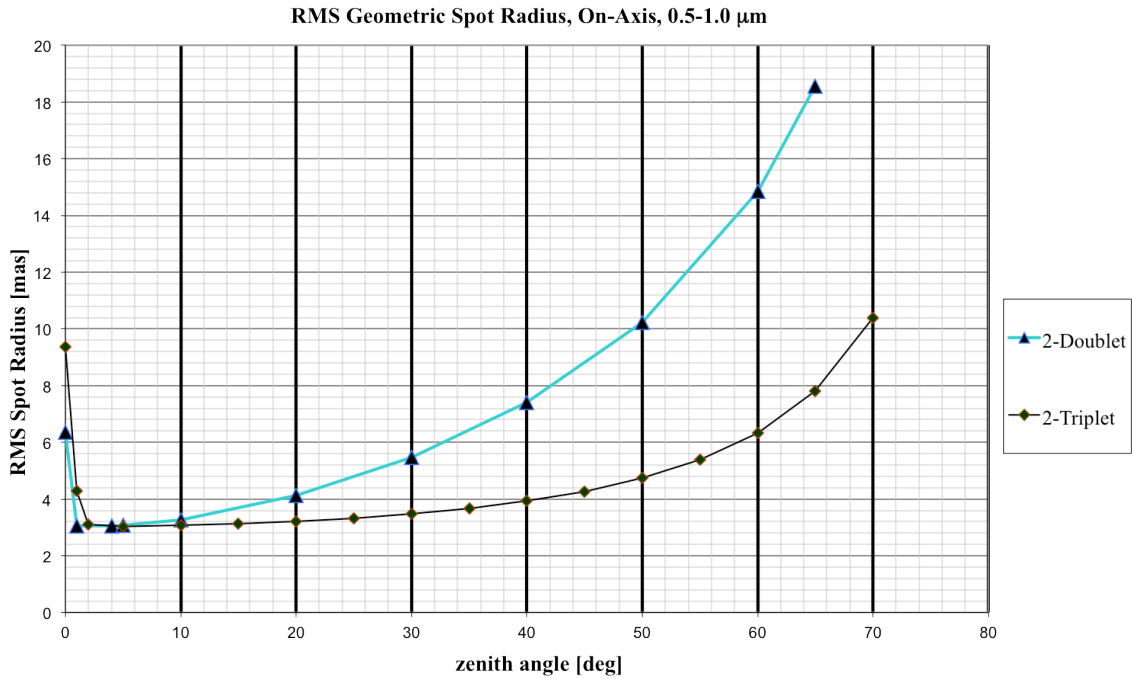


Figure 2.8 Geometric RMS spot size for the wavelength band 0.5-1.0 microns vs. Zenith angle on the sky. At high airmass ( $50^\circ$  zenith angle), our 2-triplet design performs 56% better than the convention doublet design.

### 2.3.2 Pupil Shear

Because the pyramid sensor operates by imaging the pupil, it is essential that any ADC design not introduce any significant chromatic pupil shearing. Chromatic pupil shear of more than  $\sim 10\text{-}20\%$  of the  $24\text{ }\mu\text{m}$  pixel pitch of the CCD39 could interfere with our wavefront sensing. Chromatic imaging effects cause pupil shear to be weakly dependant on field angle, pupil position, and ADC design, and more strongly dependant on zenith angle. In order to quantify the pupil shear, we traced individual rays over the  $0.6\text{-}0.9\text{ }\mu\text{m}$  wavefront sensing band both on-axis and at the edge of the field ( $1.25\text{ arcsec}$ , which is the edge of the FOV seen by the pyramid) at 20 different pupil positions for each field point for a given zenith angle and ADC design. The shear was then calculated as the



maximum distance on the CCD39 between rays of different wavelengths for a given field point and pupil position. The shears calculated with these rays over the two field points and 20 different pupil positions were then averaged and are plotted in Figure 2.9. The standard deviation of all the shears for a given ADC design and zenith angle was small, typically  $\sim 2\%$ . As Figure 2.9 shows, the shear can become significant at higher zenith angles (50% at  $70^\circ$ ). To compensate for this effect, we may need to either use a narrower wavelength band for wavefront sensing, or bin the CCD39 in a coarser sampling mode.

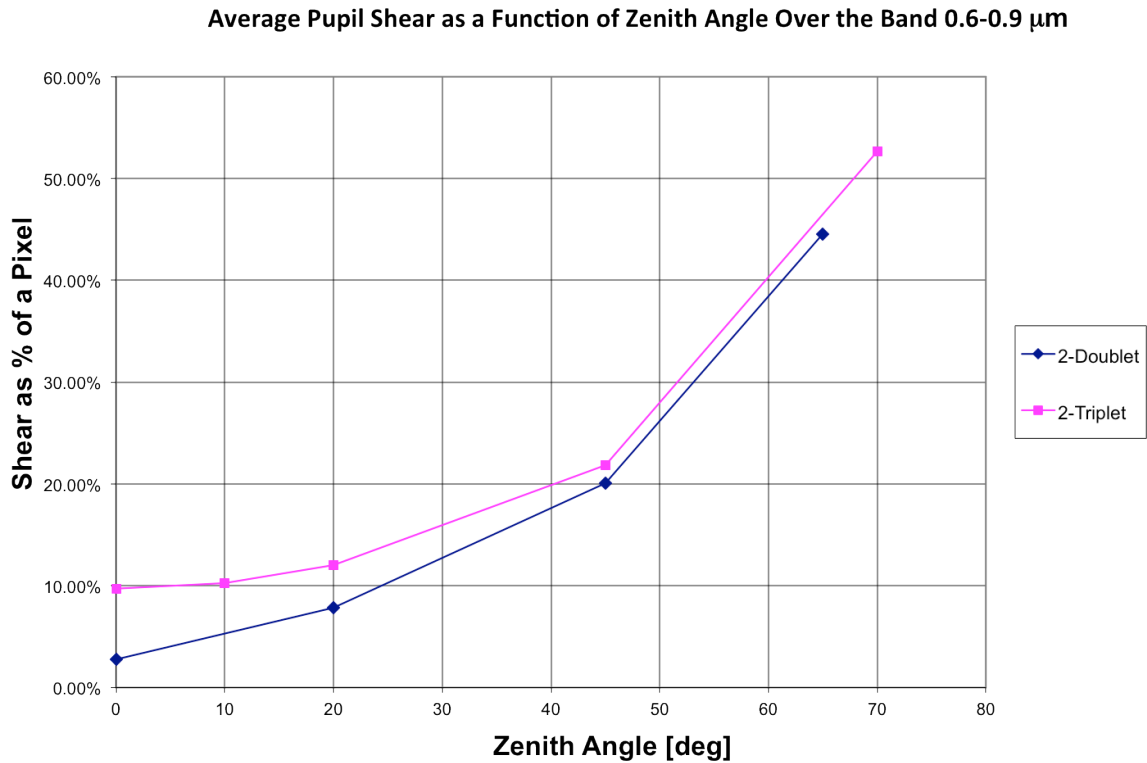


Figure 2.9 Chromatic pupil shear as a function of zenith angle over the 0.6-0.9  $\mu\text{m}$  wavefront sensing band. Each point on the plot is an average of shear values at two different field points and 20 different pupil positions. Each PWFS pixel is 24  $\mu\text{m}$ .

## 2.4 Laboratory Performance

When used on-sky looking at a broadband point source, such as a star, the ADC will be taking a little low resolution spectrum, which has been dispersed by the atmosphere, from the Magellan telescope focal plane and correcting it so that it falls on the CCD47 as a chromatically well-corrected broadband point. However, in our lab we cannot easily and reliably simulate the dispersion effects of the atmosphere in order to generate that spectrum. Therefore, we have designed a test that works in reverse: the ADC takes a white-light point source and disperses it into a spectrum at the focal plane. Using narrow band filters, we measure where various different wavelengths fall on the focal plane and compare these locations to the Zemax predictions (Figures 2.10 and 2.11).

Using a microscope objective and a pair of achromatic doublets, we reimage a fiber white-light source onto a 10 $\mu$ m pinhole. This pinhole serves as the point source that is located where the nominal Magellan telescope F/16 focal plane would be. The point source feeds the W-unit triplet input lens, which converts the beam from a diverging F/16 beam to a converging F/49 beam. This converging white light beam then passes through the ADC triplet prisms, which are in rotating mounts. The focal plane is then imaged with our Electrim EDC-3000D lab CCD. By placing three different narrow-band filters in front of the white light source (532 nm, 850 nm, and 905 nm) and measuring where these wavelengths fall on the focal plane relative to each other for various relative ADC clockings, we are able to measure both the primary and secondary dispersion characteristics of the ADC.

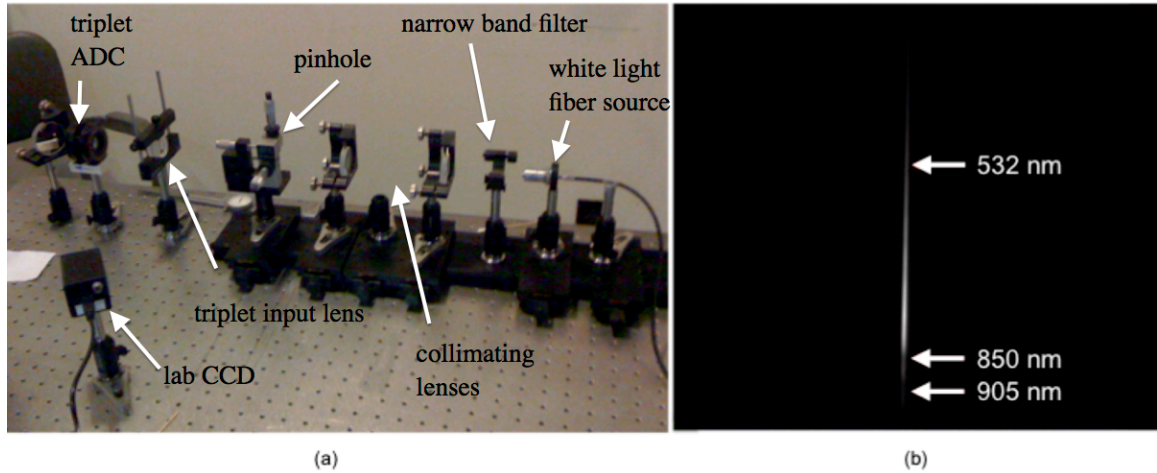


Figure 2.10 (a) Our setup for testing the dispersion characteristics of our triplet ADC. A white light fiber source is collimated and reimaged on a pinhole, which creates an F/16 beam to feed our input lens. The input lens converts the beam to a converging F/49 so that we are operating at the same focal length and beam size as the telescope. The ADCs are rotated to their maximum dispersion position and narrow-band filters are used to select certain wavelengths. (b) The white light source dispersed into a spectrum by the ADCs in their maximum dispersion position. The locations of three wavelengths were measured and compared to the Zemax prediction.

The comparison of this test and the Zemax theoretical predicted curves is shown in Figure 2.11. We expect that the most accurate results are given by the largest ADC relative clocking angle and the largest wavelength difference. In these cases, the ADC spot displacement at these selected wavelengths differs from the Zemax predicted displacement by only  $0.45\% \pm 0.15\%$ , which is comparable to the estimated systematic error of our lab setup. Therefore, the ADC dispersion is correct to within our measurement error, confirming that the ADCs were fabricated and aligned correctly, are chromatically well behaved, and perform as expected.

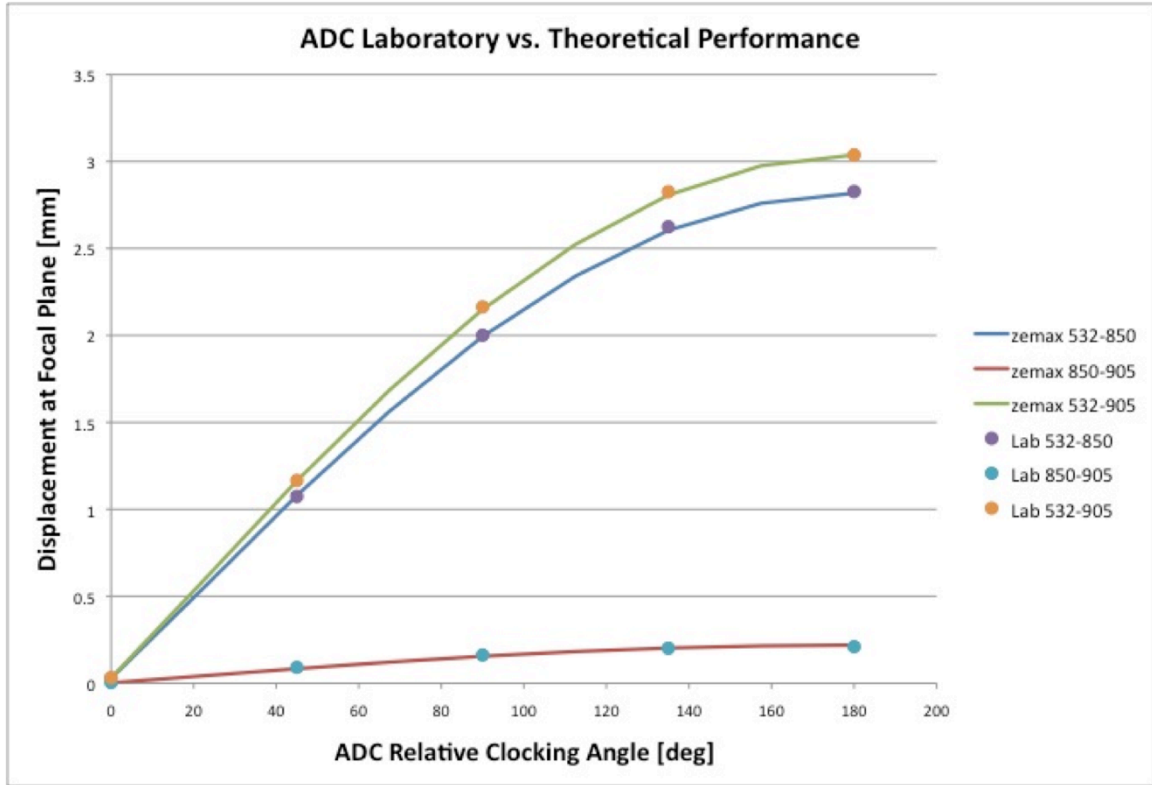


Figure 2.11 Theoretical vs. laboratory performance of the ADC at three different wavelengths. This test was performed in the lab using narrow band filters. Error bars on the data points are smaller than the spots on the plot.

## 2.5 ADC On-Sky Performance

Our triplet ADC, originally designed for the Magellan AO system scheduled to come on-sky in October 2012, has also been adopted by the LBT AO group and the LBTI group. In January of 2012, our Italian collaborators from the Arcetri institute took on-sky data with the LBT AO system and verified the performance of our triplet ADC. The LBT AO system uses the same PWFS and CCD47 as our Magellan system and the optical configuration of the W-unit is virtually identical.

The two PSFs in Fig. 2.12 were taken with the CCD47 of the LBT AO system on LHS 1772, a 7.2 r-band ( $\sim 590\text{-}730$  nm) magnitude star, at 60 degrees from zenith (2 airmasses). A dichroic beamsplitter was used to transmit 600-1000 nm light to the CCD39 PWFS and to reflect the bluer light to the CCD47. Since the response of the CCD47 falls off around 400-450 nm, the wavelength band represented in these images is  $\sim 400\text{-}600$  nm. The AO loop was running at 1 kHz with only 150 modes corrected. Pixel scale is approximately 14 mas/pixel. Natural seeing was poor, roughly 1.7 arcsec. Both images are an average of 20 frames with 0.28 seconds exposure time, with background subtracted. The PSF in Fig. 12a is with the ADC in its nominal position, i.e. zero dispersion. The PSF in Fig. 12b is with the ADC prisms at a relative clocking of 60 degrees in order to correct the atmospheric dispersion.

The uncorrected PSF is elongated by  $\sim 210$   $\mu\text{m}$  due to the atmospheric dispersion and has an ellipticity of 0.16. The corrected image has an ellipticity of 0.03 and shows virtually no atmospheric dispersion. The observer at the telescope performed the ADC correction by eye by clocking the ADC to minimize PSF ellipticity. The “boxy” appearance of the corrected image is a waffle artifact that is the result of the binning of the PWFS and is not an effect of the ADC.

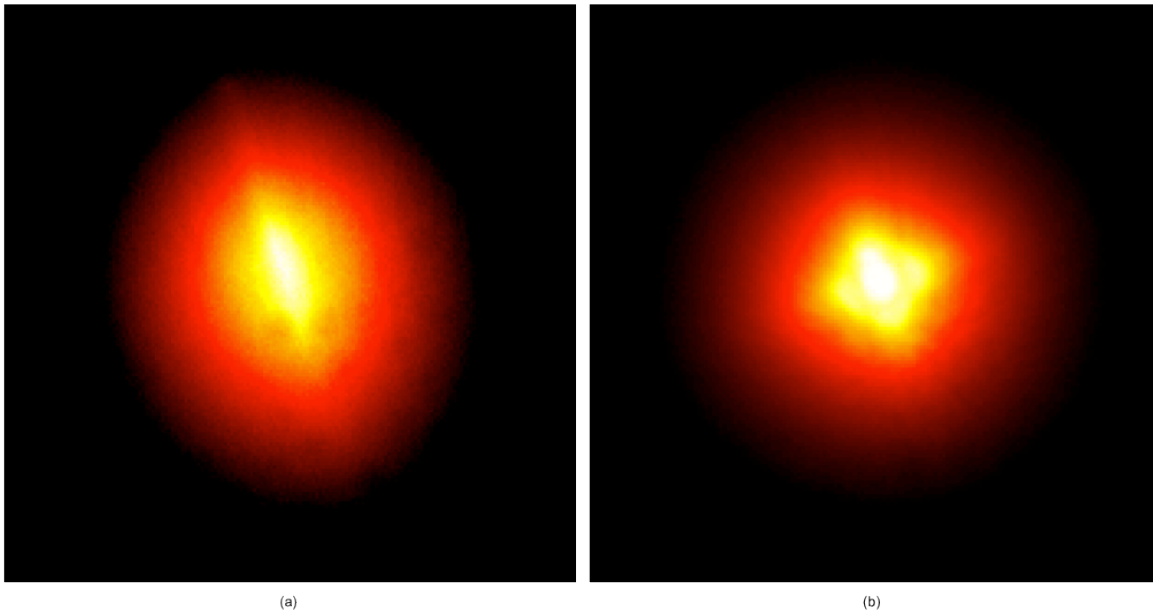


Figure 2.12 On-sky data demonstrating the performance of the triplet ADC on the LBT AO system. (a) The uncorrected elongation of the PSF caused by atmospheric dispersion at 60 degrees from zenith. FWHM is  $\sim 1.13$  arcsec in the dispersed direction and  $\sim 0.9$  arcsec in the undispersed direction. (b) The PSF after having dispersion corrected with the ADC. Natural seeing was poor ( $\sim 1.7$  arcsec).

## 2.6 The Zero-Deviation Design

Ideally, the crown and flint of a 2-doublet ADC, or the crown, flint, and anomalous dispersion glass of our 2-triplet ADC, would be perfectly index matched so that the optical axis of the beam did not deviate at all as it passed through the ADC on the way to the focal plane. In reality, no set of glasses, however carefully chosen, will have perfectly zero optical axis deviation as long as the faces of the ADC are parallel (as they are for most conventional designs). As a result, as the star moves across the sky and the zenith angle/airmass varies, the ADC will rotate to compensate for the atmospheric dispersion and the color-corrected star image will wander around on the focal plane.

Depending on how well the ADC glasses are index-matched, this beam deviation can be insignificant or quite large.

For many typical science cases, this beam deviation is not a concern because the science target can be maintained on the center of the detector through other means. In the case of the VisAO camera, if the star wanders a bit on the CCD, our actuated tip/tilt dither mirror can simply be adjusted to bring the star back to the center of the field. However, for other applications (such as maintaining alignment on the slit of CLIO2's spectrograph), beam deviation can present real problems. For instance, the pyramid wavefront sensor has a pupil rerotator that is precisely aligned to the optical axis of the system, with a very tight tolerance on the angle at which it can accept the incoming beam. An ADC with significant beam deviation can throw the rerotator out of alignment and prevent the wavefront sensor from working at higher airmass. Another example of beam deviation becoming a problem would be a spectrograph with a narrow input slit that requires precise alignment of the star to the slit during long integrations.

To mitigate this beam deviation effect, in Zemax we allowed the angles of the front and back faces of the triplet ADC to be free parameters and optimized our design to have both excellent chromatic performance and zero beam-deviation. With only small angles of tilt on the front and back surfaces of the triplet ADC (whereas before they were perfectly parallel), we were able to force the beam deviation to be zero at all zenith angles. See Table 2.3 for the optical prescription of the zero-deviation ADC. We expect this change to negligibly affect the cost of fabrication of the ADCs, hence we will use this technique for all future designs.

**Table 2.3**  
**Zero-Deviation Triplet ADC Optical Prescription**

Surface	Thickness (mm)	Glass	Tilt Angle (deg)
1	5	S-PHM53 (OHARA)	0.186
2	3	S-TIM8 (OHARA)	32.497
3	4	N-KZFS4 (SCHOTT)	24.844
4	...	...	0.231

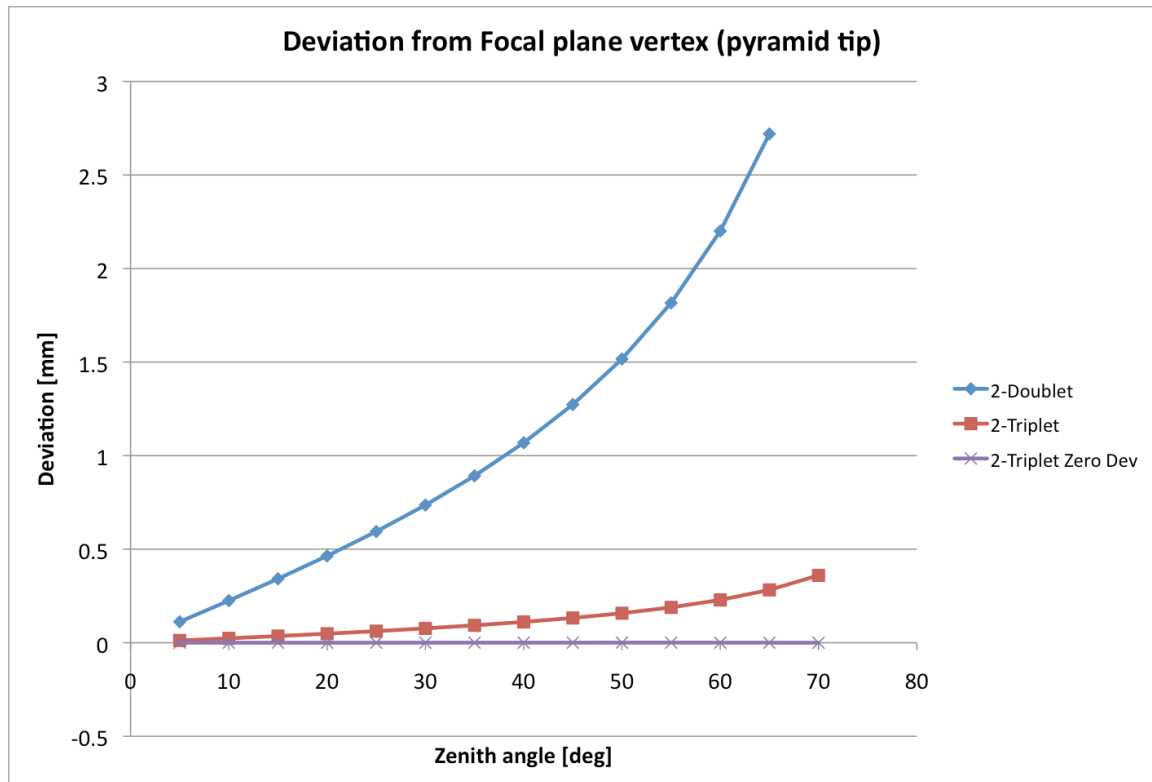


Figure 2.13 Beam deviation in mm as a function of Zenith angle on the sky. Our as-built triplet ADC is ~9 times better than the conventional doublet design. The Zero Deviation design is a further improvement still.



## 2.7 Status

Our triplet ADC has been adopted by Magellan, the LBT, and the LBTI groups with preliminary on-sky results already obtained from LBT. We have tested the ADC at Magellan. In November 2012, we will test the ADC on-sky at Magellan for the first time. I wrote a Zemax macro to generate lookup tables for the ADC clocking angles for a given wavelength band, atmospheric site parameters, and zenith angle increment. Appendix 2.9 gives some sample lookup tables for the waveband 600-1000 nm (our maximum commissioning waveband for wavefront sensing and science) using typical Magellan site parameters for a night in the summer. At low airmass, the ADC clocking angles are not symmetric about zero because, in addition to correcting the atmospheric dispersion, the ADC is compensating for the residual chromatism of the triplet prisms, i.e. the same effect at play in the zenith spike effect. More lookup tables will be generated during commissioning for parameters and bandpasses.

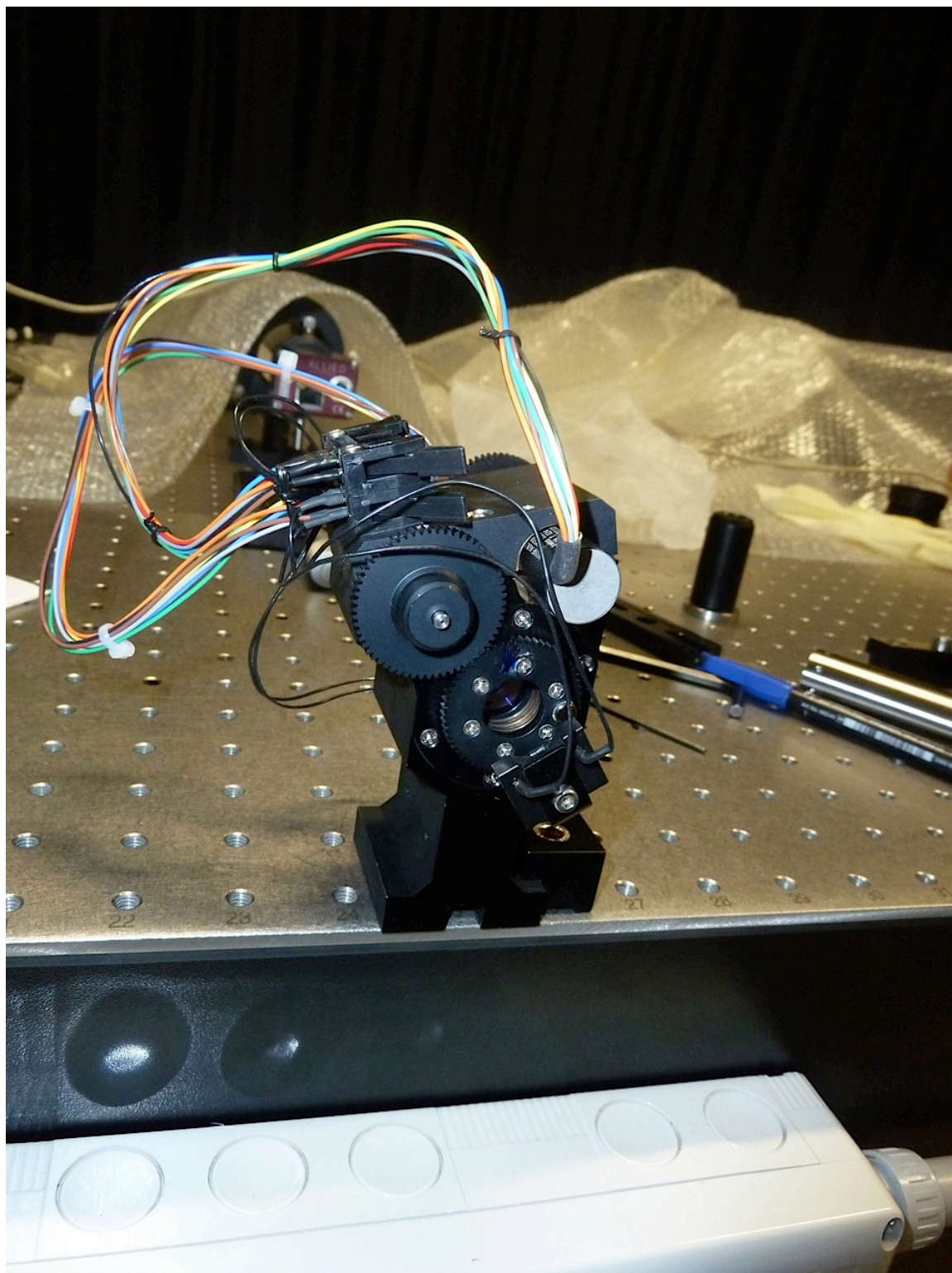


Figure 2.14 The triplet ADC in its Arcetri-fabricated rotation mount.

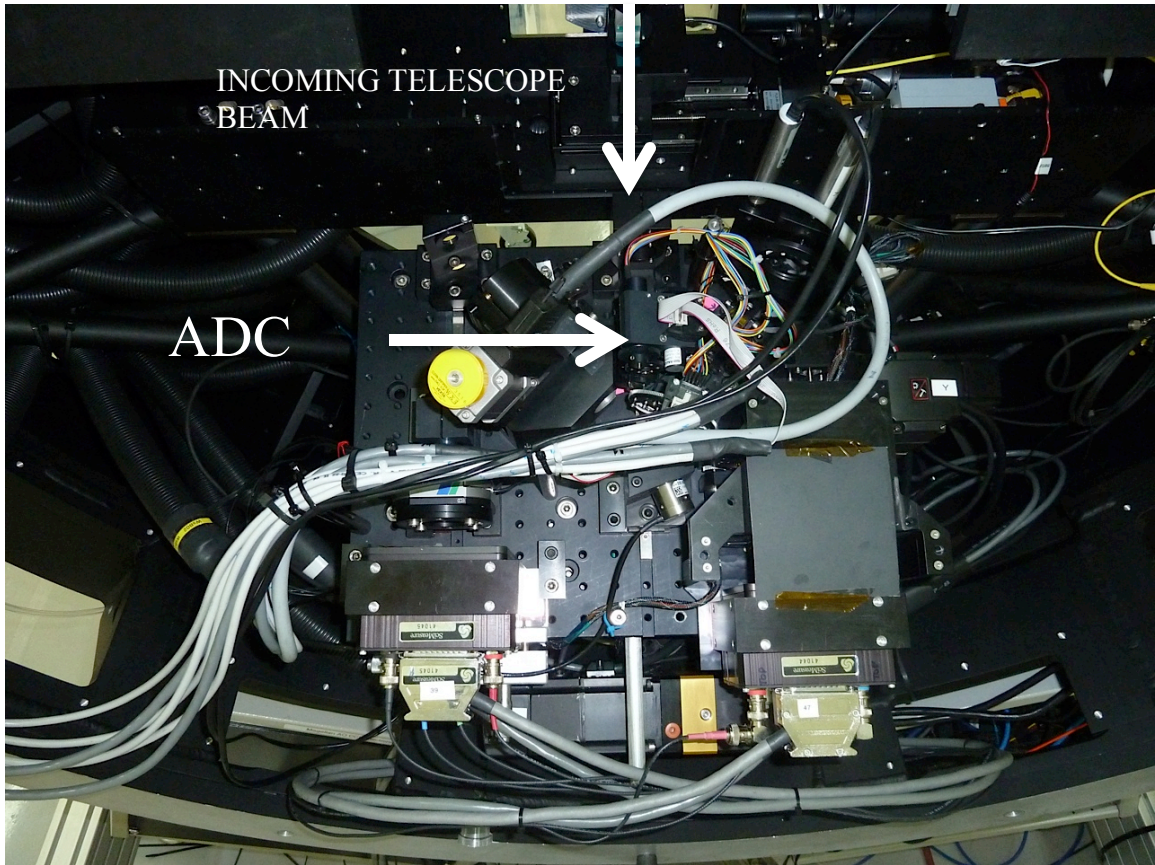


Figure 2.15 The ADC in its mount integrated into the W-Unit.

## 2.8 Conclusion

We discuss the motivation, design, fabrication, laboratory verification, and on-sky performance of our advanced apochromatic triplet ADC for the Magellan AO system. The ADC performs in the lab as predicted and its performance was verified on-sky as a component in the LBT AO system. We also present the design of our novel zero-deviation triplet ADC, which gives the same chromatic performance as our original triplet design and zero beam-deviation at all design zenith angles. This zero-deviation triplet ADC will be essential to the success of future ground-based high-resolution broadband visible imaging and spectroscopy systems. We expect that the design

principles and techniques that we have employed in this project will be useful and relevant for future high-resolution ground-based systems.

## 2.9 Appendix: Sample ADC Clocking Angle Look-up Tables

Executing C:\Program Files\ZEMAX\Macros\Z\_SCAN\_ADC\_ANGLE.ZPL.

Altitude in meters is: 2380.0000  
 Temperature in K is: 283.0000  
 Pressure in millibars is: 765.0000  
 Humidity fraction is: 0.2500  
 Latitude is: 0.0000

First column is zenith angle  
 Second column is clocking angle of ADC1  
 Third column is clocking angle of ADC2  
 Standing at the tertiary looking towards the W-unit, a positive angle is clockwise.

Wavelength band is: 0.6-1.0 um

5.0000	24.8776	22.2294
6.0000	21.0620	17.7897
7.0000	18.4812	14.5946
8.0000	16.6468	12.1517
9.0000	15.2947	10.1933
10.0000	14.2810	8.5731
11.0000	13.5079	7.1923
12.0000	12.9162	5.9906
13.0000	12.4648	4.9259
14.0000	12.1229	3.9666
15.0000	11.8681	3.0897
16.0000	11.6867	2.2811
17.0000	11.5645	1.5255
18.0000	11.4944	0.8156
19.0000	11.4661	0.1403
20.0000	11.4772	-0.5034
21.0000	11.5205	-1.1232
22.0000	11.5936	-1.7225
23.0000	11.6933	-2.3047
24.0000	11.8176	-2.8726
25.0000	11.9635	-3.4303
26.0000	12.1307	-3.9786



27.0000 12.3168 -4.5206  
28.0000 12.5217 -5.0574  
29.0000 12.7440 -5.5914  
30.0000 12.9836 -6.1233  
31.0000 13.2398 -6.6552  
32.0000 13.5125 -7.1880  
33.0000 13.8010 -7.7237  
34.0000 14.1068 -8.2619  
35.0000 14.4281 -8.8059  
36.0000 14.7661 -9.3558  
37.0000 15.1212 -9.9128  
38.0000 15.4934 -10.4784  
39.0000 15.8834 -11.0537  
40.0000 16.2922 -11.6398  
41.0000 16.7202 -12.2383  
42.0000 17.1682 -12.8505  
43.0000 17.6374 -13.4781  
44.0000 18.1288 -14.1224  
45.0000 18.6439 -14.7853  
46.0000 19.1838 -15.4686  
47.0000 19.7505 -16.1740  
48.0000 20.3456 -16.9042  
49.0000 20.9714 -17.6610  
50.0000 21.6299 -18.4475  
51.0000 22.3242 -19.2663  
52.0000 23.0569 -20.1207  
53.0000 23.8315 -21.0145  
54.0000 24.6520 -21.9515  
55.0000 25.5226 -22.9367  
56.0000 26.4486 -23.9751  
57.0000 27.4356 -25.0729  
58.0000 28.4905 -26.2370  
59.0000 29.6212 -27.4757  
60.0000 30.8372 -28.7986  
61.0000 32.1496 -30.2169  
62.0000 33.5719 -31.7444  
63.0000 35.1192 -33.3986  
64.0000 36.8136 -35.1980  
65.0000 38.6787 -37.1697  
66.0000 40.7477 -39.3456  
67.0000 43.0614 -41.7700  
68.0000 45.6792 -44.4992  
69.0000 48.6800 -47.6173  
70.0000 52.1858 -51.2467

DONE.

Executing C:\Program Files\ZEMAX\Macros\Z\_SCAN\_ADC\_ANGLE.ZPL.

Altitude in meters is: 2380.0000  
 Temperature in K is: 293.0000  
 Pressure in millibars is: 765.0000  
 Humidity fraction is: 0.2500  
 Latitude is: 0.0000

First column is zenith angle  
 Second column is clocking angle of ADC1  
 Third column is clocking angle of ADC2  
 Standing at the tertiary looking towards the W-unit, a  
 positive angle is clockwise.

Wavelength band is: 0.6-1.0 um

5.0000	25.7125	23.1729
6.0000	21.7164	18.5699
7.0000	19.0166	15.2752
8.0000	17.0874	12.7564
9.0000	15.6629	10.7449
10.0000	14.5899	9.0855
11.0000	13.7672	7.6751
12.0000	13.1332	6.4514
13.0000	12.6436	5.3689
14.0000	12.2676	4.3963
15.0000	11.9828	3.5104
16.0000	11.7727	2.6941
17.0000	11.6251	1.9348
18.0000	11.5288	1.2204
19.0000	11.4787	0.5454
20.0000	11.4665	-0.0992
21.0000	11.4883	-0.7178
22.0000	11.5406	-1.3147
23.0000	11.6200	-1.8938
24.0000	11.7244	-2.4578
25.0000	11.8511	-3.0103
26.0000	11.9989	-3.5531
27.0000	12.1667	-4.0883
28.0000	12.3527	-4.6182
29.0000	12.5566	-5.1441
30.0000	12.7776	-5.6678

31.0000 13.0151 -6.1906  
32.0000 13.2691 -6.7138  
33.0000 13.5393 -7.2387  
34.0000 13.8252 -7.7670  
35.0000 14.1281 -8.2986  
36.0000 14.4465 -8.8365  
37.0000 14.7818 -9.3807  
38.0000 15.1340 -9.9326  
39.0000 15.5037 -10.4935  
40.0000 15.8912 -11.0650  
41.0000 16.2978 -11.6476  
42.0000 16.7237 -12.2433  
43.0000 17.1702 -12.8533  
44.0000 17.6382 -13.4792  
45.0000 18.1290 -14.1226  
46.0000 18.6439 -14.7853  
47.0000 19.1843 -15.4692  
48.0000 19.7523 -16.1763  
49.0000 20.3496 -16.9088  
50.0000 20.9784 -17.6695  
51.0000 21.6413 -18.4608  
52.0000 22.3411 -19.2860  
53.0000 23.0808 -20.1484  
54.0000 23.8642 -21.0519  
55.0000 24.6955 -22.0009  
56.0000 25.5792 -23.0003  
57.0000 26.5210 -24.0559  
58.0000 27.5270 -25.1741  
59.0000 28.6046 -26.3627  
60.0000 29.7628 -27.6301  
61.0000 31.0113 -28.9874  
62.0000 32.3625 -30.4471  
63.0000 33.8318 -32.0236  
64.0000 35.4363 -33.7364  
65.0000 37.1999 -35.6072  
66.0000 39.1498 -37.6663  
67.0000 41.3237 -39.9504  
68.0000 43.7704 -42.5103  
69.0000 46.5579 -45.4146  
70.0000 49.7849 -48.7628  
DONE.

Executing C:\Program Files\ZEMAX\Macros\Z\_SCAN\_ADC\_ANGLE.ZPL.

Altitude in meters is: 2380.0000  
 Temperature in K is: 288.0000  
 Pressure in millibars is: 765.0000  
 Humidity fraction is: 0.2500  
 Latitude is: 0.0000

First column is zenith angle  
 Second column is clocking angle of ADC1  
 Third column is clocking angle of ADC2  
 Standing at the tertiary looking towards the W-unit, a  
 positive angle is clockwise.

Wavelength band is: 0.5-1.0 um

5.0000	24.2384	21.6374
6.0000	20.5331	17.3235
7.0000	18.0238	14.2156
8.0000	16.2373	11.8352
9.0000	14.9233	9.9291
10.0000	13.9359	8.3494
11.0000	13.1845	7.0045
12.0000	12.6096	5.8335
13.0000	12.1702	4.7949
14.0000	11.8378	3.8592
15.0000	11.5913	3.0048
16.0000	11.4151	2.2156
17.0000	11.2975	1.4792
18.0000	11.2295	0.7858
19.0000	11.2038	0.1279
20.0000	11.2150	-0.5008
21.0000	11.2586	-1.1054
22.0000	11.3310	-1.6899
23.0000	11.4294	-2.2580
24.0000	11.5513	-2.8127
25.0000	11.6949	-3.3565
26.0000	11.8588	-3.8918
27.0000	12.0416	-4.4205
28.0000	12.2424	-4.9444
29.0000	12.4604	-5.4652
30.0000	12.6951	-5.9843
31.0000	12.9461	-6.5032
32.0000	13.2131	-7.0231
33.0000	13.4959	-7.5454
34.0000	13.7946	-8.0711



35.0000 14.1092 -8.6016  
 36.0000 14.4400 -9.1379  
 37.0000 14.7873 -9.6812  
 38.0000 15.1514 -10.2328  
 39.0000 15.5330 -10.7938  
 40.0000 15.9325 -11.3654  
 41.0000 16.3508 -11.9491  
 42.0000 16.7887 -12.5461  
 43.0000 17.2471 -13.1579  
 44.0000 17.7272 -13.7860  
 45.0000 18.2302 -14.4321  
 46.0000 18.7575 -15.0978  
 47.0000 19.3107 -15.7853  
 48.0000 19.8916 -16.4964  
 49.0000 20.5021 -17.2336  
 50.0000 21.1446 -17.9994  
 51.0000 21.8216 -18.7965  
 52.0000 22.5359 -19.6281  
 53.0000 23.2908 -20.4976  
 54.0000 24.0900 -21.4090  
 55.0000 24.9377 -22.3668  
 56.0000 25.8388 -23.3759  
 57.0000 26.7988 -24.4422  
 58.0000 27.8243 -25.5724  
 59.0000 28.9227 -26.7742  
 60.0000 30.1029 -28.0568  
 61.0000 31.3755 -29.4309  
 62.0000 32.7531 -30.9093  
 63.0000 34.2508 -32.5077  
 64.0000 35.8874 -34.2451  
 65.0000 37.6862 -36.1453  
 66.0000 39.6769 -38.2384  
 67.0000 41.8978 -40.5636  
 68.0000 44.4004 -43.1733  
 69.0000 47.2564 -46.1404  
 70.0000 50.5704 -49.5714  
 DONE.

Executing C:\Program Files\ZEMAX\Macros\Z\_SCAN\_ADC\_ANGLE.ZPL.

ADC clocking angles in this table are forced to be equal and opposite.

Altitude in meters is: 2380.0000

Temperature in K is: 288.0000

Pressure in millibars is: 765.0000

Humidity fraction is: 0.2500

First column is zenith angle

Second column is clocking angle of ADC1

Third column is clocking angle of ADC2

Standing at the tertiary looking towards the W-unit,  
a positive angle is clockwise.

Wavelength band is: 0.6000-1.0000 microns

1.0000	0.2832	-0.2832
2.0000	0.5665	-0.5665
3.0000	0.8502	-0.8502
4.0000	1.1344	-1.1344
5.0000	1.4193	-1.4193
6.0000	1.7051	-1.7051
7.0000	1.9919	-1.9919
8.0000	2.2803	-2.2803
9.0000	2.5700	-2.5700
10.0000	2.8612	-2.8612
11.0000	3.1545	-3.1545
12.0000	3.4498	-3.4498
13.0000	3.7473	-3.7473
14.0000	4.0474	-4.0474
15.0000	4.3502	-4.3502
16.0000	4.6559	-4.6559
17.0000	4.9649	-4.9649
18.0000	5.2773	-5.2773
19.0000	5.5934	-5.5934
20.0000	5.9135	-5.9135
21.0000	6.2378	-6.2378
22.0000	6.5668	-6.5668
23.0000	6.9006	-6.9006
24.0000	7.2396	-7.2396
25.0000	7.5841	-7.5841
26.0000	7.9346	-7.9346
27.0000	8.2913	-8.2913
28.0000	8.6548	-8.6548
29.0000	9.0255	-9.0255
30.0000	9.4037	-9.4037
31.0000	9.7900	-9.7900
32.0000	10.1849	-10.1849
33.0000	10.5890	-10.5890

34.0000 11.0029 -11.0029  
35.0000 11.4271 -11.4271  
36.0000 11.8626 -11.8626  
37.0000 12.3098 -12.3098  
38.0000 12.7697 -12.7697  
39.0000 13.2432 -13.2432  
40.0000 13.7310 -13.7310  
41.0000 14.2344 -14.2344  
42.0000 14.7543 -14.7543  
43.0000 15.2921 -15.2921  
44.0000 15.8490 -15.8490  
45.0000 16.4264 -16.4264  
46.0000 17.0260 -17.0260  
47.0000 17.6498 -17.6498  
48.0000 18.2992 -18.2992  
49.0000 18.9768 -18.9768  
50.0000 19.6849 -19.6849  
51.0000 20.4263 -20.4263  
52.0000 21.2037 -21.2037  
53.0000 22.0209 -22.0209  
54.0000 22.8812 -22.8812  
55.0000 23.7897 -23.7897  
56.0000 24.7509 -24.7509  
57.0000 25.7708 -25.7708  
58.0000 26.8558 -26.8558  
59.0000 28.0140 -28.0140  
60.0000 29.2543 -29.2543  
61.0000 30.5875 -30.5875  
62.0000 32.0267 -32.0267  
63.0000 33.5874 -33.5874  
64.0000 35.2889 -35.2889  
65.0000 37.1552 -37.1552  
66.0000 39.2167 -39.2167  
67.0000 41.5132 -41.5132  
68.0000 44.0988 -44.0988  
69.0000 47.0470 -47.0470  
70.0000 50.4677 -50.4677  
DONE.

## CHAPTER 3

### STATUS UPDATE AND CLOSED-LOOP PERFORMANCE OF THE MAGELLAN ADAPTIVE OPTICS VISAO CAMERA

*The Chapter contains work that was originally published by Kopon et al. in the Conference Proceedings of the SPIE 2012, paper 8447-122. I designed and procured all of the VisAO optics, assembled the VisAO camera, and assisted with the assembly and alignment of the pyramid wavefront sensor. I also assisted in the Arcetri tower tests.*

We present laboratory results of the closed-loop performance of the Magellan Adaptive Optics (AO) Adaptive Secondary Mirror (ASM), pyramid wavefront sensor (PWFS), and VisAO visible adaptive optics camera. As described in Chapter 2, the Magellan AO system is a 585-actuator low-emissivity high-throughput system scheduled for first light on the 6.5 meter Magellan Clay telescope in November 2012. Using a dichroic beamsplitter near the telescope focal plane, the AO system will be able to simultaneously perform visible (500-1000 nm) AO science with our VisAO camera and either 8-28  $\mu\text{m}$  or 1-5  $\mu\text{m}$  science using either the BLINC/MIRAC4 or CLIO2 camera, respectively. The ASM, PWFS, and VisAO camera have undergone final system tests in the solar test tower at the Arcetri Institute in Florence, Italy, reaching Strehl ratios of 37% in i'-band with 400 modes and simulated turbulence with  $r_0 = 14$  cm at V-band. We present images and test results of the assembled VisAO system, which includes our

prototype advanced Atmospheric Dispersion Corrector (ADC), prototype calcite Wollaston prisms for SDI imaging, and a suite of beamsplitters, filters, and other optics. We also present images and results of our unique Calibration Return Optic (CRO) test system and the ASM, which has successfully run in closed loop at 1 kHz. The CRO test is a retro reflecting optical test that allows us to test the ASM off-sky in closed-loop using an artificial star formed by a fiber source.

### 3.1 Introduction: Magellan Simultaneous Visible and IR Adaptive Optics

The Magellan Clay telescope (Figure 3.1) is a 6.5 m Gregorian telescope located at the Las Campanas Observatory (LCO) in Chile. In the fall of 2012 we, along with our collaborators at the Arcetri Observatory and the Carnegie Institute, will be commissioning the first Adaptive Optics system on the Magellan telescope. Our AO system uses an 85 cm diameter adaptive secondary mirror with 585 actuators. With the exception of our smaller number of actuators and ASM diameter (585 actuators vs. 672 on LBT), our system is a virtual clone of the recently commissioned LBT AO system (Esposito et al. 2010), using the same secondary optical prescription, control hardware, software, and pyramid wavefront sensor. Because our primary mirror is smaller than the LBT 8 m mirror, we have finer actuator spacing in the pupil and therefore expect excellent Strehls in the IR ( $\sim 90\%$  at H-band), and good Strehls in the longer visible wavelengths ( $\sim 37\%$  at i'-band).

To take advantage of high-Strehl AO correction and the excellent seeing at the Magellan site ( $r_0$  is frequently as high as 20 cm at 550 nm) our first light commissioning

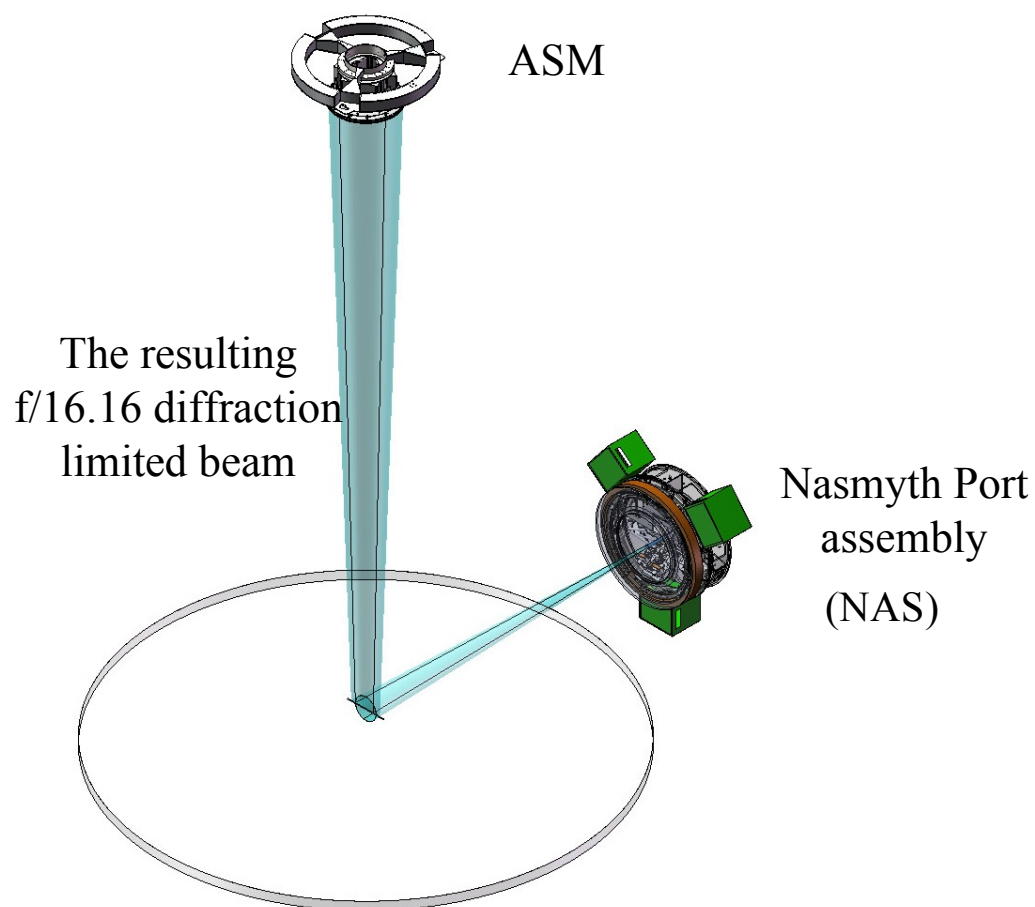


Figure 3.1 Schematic layout of the Magellan telescope, the adaptive secondary mirror, and the science instruments. Note the 6.5 m primary. The f/16.16 beam is shown in blue.

will make use of two science instruments: the CLIO2 1-5  $\mu\text{m}$  camera (see Sivanandam et al. 2006) and our VisAO camera (Kopon et al. 2009). While the original motivation for an adaptive secondary system is to reduce thermal background by reducing the number of warm reflections in the optical train, the fine actuator pitch and fast actuator response will also allow good seeing correction at shorter wavelengths. Our dichroic beamsplitter located near the telescope focal plane will transmit IR light to CLIO2 and will reflect visible light to the W-unit, an optical board containing both the PWFS and VisAO camera. With our predicted  $\sim 37\%$  Strehl at  $i'$ -band and 8.5 mas pixels, we plan to make images  $> 4.7$  times sharper than the highest resolution instrument on HST (none of the instruments currently operational on HST Nyquist sample at less than 1  $\mu\text{m}$ ) over our 8.5 arcsec FOV. A suite of filters, beamsplitters, and other optical components will allow many different observing modes in the visible depending on the science case and the guide star magnitude.

The full system, with all of the VisAO optical components, the ASM, and the PWFS was tested closed loop at 1 kHz in the test tower. All of the hardware has arrived in Chile after passing our pre-ship review and final system testing in Florence, Italy. The hardware has been unpacked and will be installed for first light on the telescope in November of 2012.

### 3.2 The W-Unit: Pyramid Wavefront Sensing and the VisAO Camera

Visible light reflected from the dichroic travels to the W-unit, an optical board mounted on a precision 3-axis translation stage that can patrol a  $2.3 \times 3.2$  arcmin field to acquire guide stars and science targets. The W-unit contains both the PWFS and the VisAO

science camera. The ability to move around this wide field, combined with a telecentric lens that corrects field curvature, allows us to look several minutes away from the guide star with the CLIO2 IR camera, thereby significantly increasing our sky coverage. The visible light reflected from the dichroic to the W-unit passes through a triplet lens that changes the beam from a diverging F/16 beam to a converging F/49 beam. The light then passes through the triplet ADC before reaching the beamsplitter wheel that contains a host of beamsplitters and dichroics. The transmitted light from the beamsplitter wheel goes to the PWFS and the reflected light goes to the VisAO science camera. Having the beamsplitter wheel as late as possible in the optical train minimizes non-common-path errors. The non-common-path errors that do occur are mainly due to the beamsplitters ( $\sim 20$  nm rms). Figure 3.2 shows the layout of the W-unit.



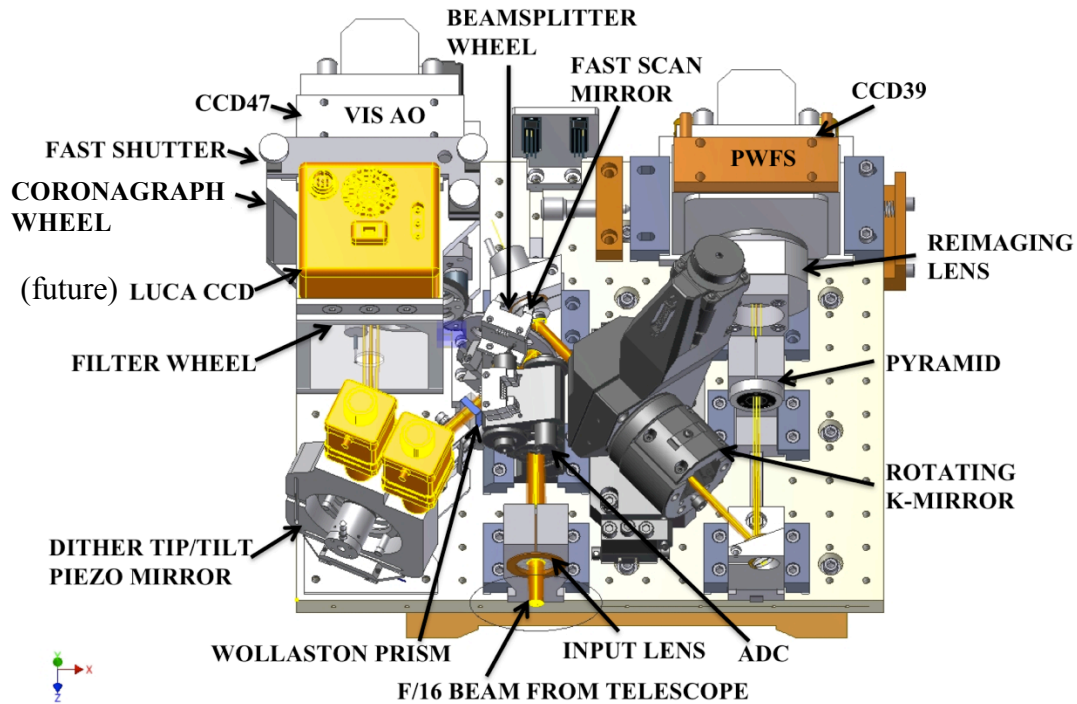


Figure 3.2 The W-unit optical board (also shown in Chapter 2). Incoming light from the telescope enters the input lens and then passes through the ADC before hitting the beamsplitter wheel. Reflected light from the beamsplitter goes to the VisAO science camera. Transmitted light goes to the PWFS.

### 3.2.1 Pyramid Wavefront Sensor

Transmitted light from the beamsplitter wheel enters the PWFS channel and reflects off of a piezo fast steering mirror located near the reimaged pupil that is used to circularly modulate the guide star image around the pyramid tip. Next, the light passes through a K-mirror rerotator that rotates the pupil so that the image of the ASM actuators stays fixed with respect to the CCD39. A K-mirror is a 3-mirror configuration that rotates about the optical axis of an incoming beam and can be used for rotating a telescope pupil. A double pyramid followed by a reimaging lens then forms four pupil images in the quadrants of the CCD39. The resultant image on the CCD39 is four pupil images whose intensity variations can be used to reconstruct the wavefront (Figure 3.3). A detailed description of the operation of the pyramid sensor arm of the W-unit can be found in Esposito et al. 2008. The pyramid sensor is very important for visible AO because of its potential for approaching a telescope's diffraction limit. The ability to change the binning of the CCD39 allows the PWFS to operate over a large dynamic range. The PWFS uses the full pupil aperture and is only diffraction-limited by the size of the primary mirror. By comparison, a Shack-Hartmann (SH) sensor is diffraction-limited by the size of a pupil sub-aperture, i.e. the pitch of its lenslet array. Since the wavefront sensing wavelengths are essentially the same as the science wavelengths ( $\sim 0.7 \mu\text{m}$ ), it is essential that the wavefront sensor operate as close to the diffraction limit as possible (Esposito et al. 2000). The dynamic range provided by the PWFS should allow us to use  $\sim 2$  mag fainter guide stars than would be allowed by the SH sensor, in addition to

allowing us to come very close to diffraction-limited correction (Esposito et al. 2001), even in the visible.

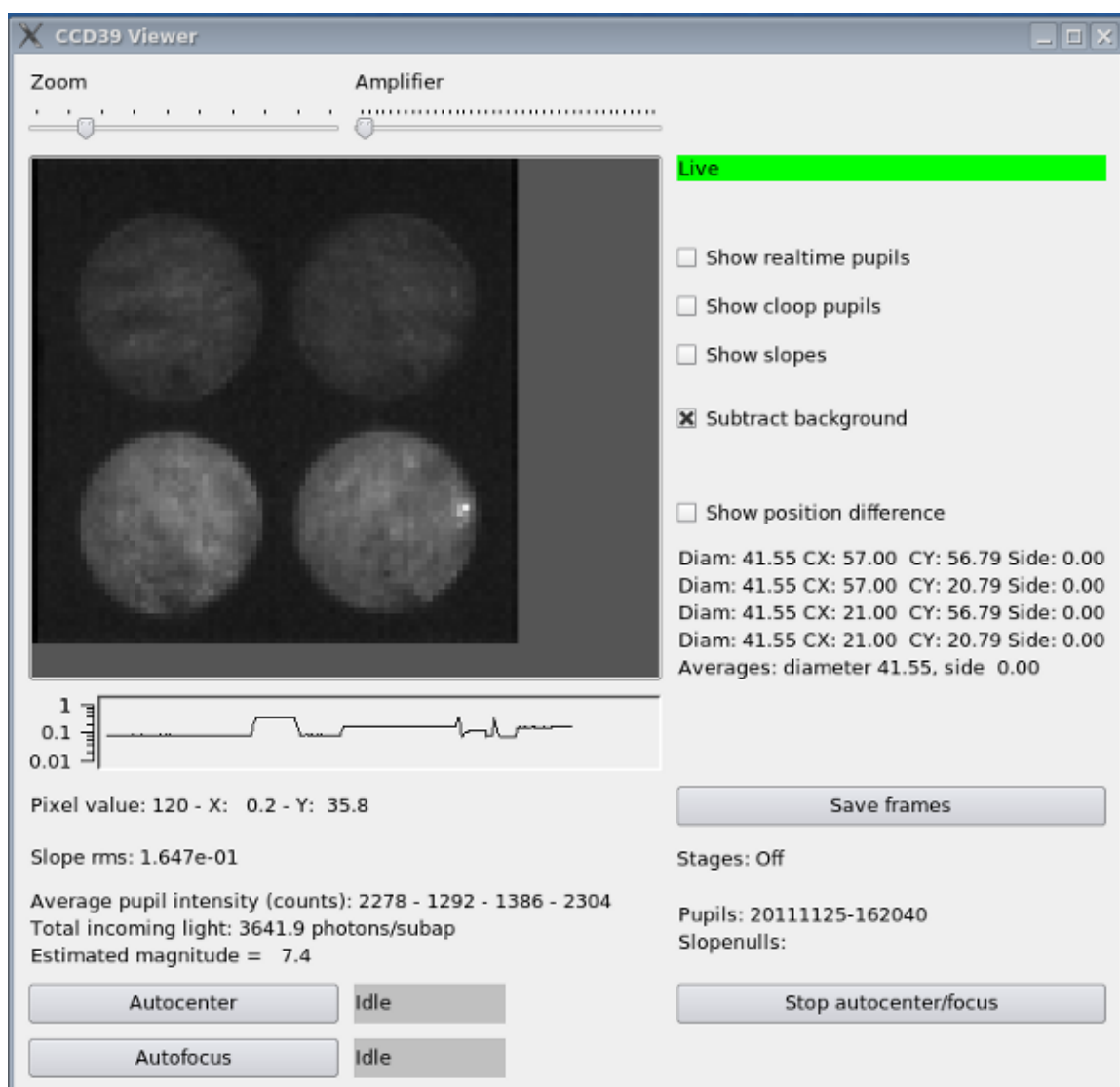


Figure 3.3 The PWFS GUI showing the 4 pupil images taken at the CCD39. The piezo mirror is modulating the point test source around the pyramid tip at 100 Hz.

### 3.2.2 Advanced Triplet ADC

While atmospheric dispersion is generally a small effect compared to the FWHM in the IR over the wavebands at which we are observing, the effect is quite significant at shorter visible wavelengths. There is great scientific incentive to push into the shorter wavelengths and to be able to observe over a wide band in order to see faint companions in scattered light, circumstellar structure in the visible, and many other cases. For instance, over the band 500-1000 nm, atmospheric dispersion at 50° zenith angle creates a PSF that is 1.3 arcsec long in the dispersed direction and diffraction limited (20-40 mas) in the other. Correcting this large amount of dispersion over a large band requires an ADC that can correct both primary and secondary chromatism (see Kopon et al. 2009 and Chapter 2). In addition to correcting the atmospheric dispersion for the VisAO science imaging, the correction is also important for the PWFS. Having a tight, well-corrected image of the guide star on the pyramid tip allows for tighter modulation radii, higher sensitivity, and therefore better AO correction.

We designed, fabricated, and tested a triplet ADC that corrected both primary and secondary chromatism and allows us to reach the broadband diffraction limit (500-1000 nm) out to a Zenith angle of 70 degrees (2.9 air masses). We tested the dispersion and image quality of these optics using a special lab setup consisting of a white light fiber source and several narrow band filters (see Kopon et al. 2010). Our ADC was adopted by our Arcetri collaborators for use on the LBT AO system. Its performance was recently verified on sky at 60 degree zenith angle with the AO system running in closed loop (see Kopon et al. 2012). See Chapter 2 for more on the ADC.



Figure 3.4 The triplet ADC. The ADC is 14 mm in diameter and 12 mm thick.

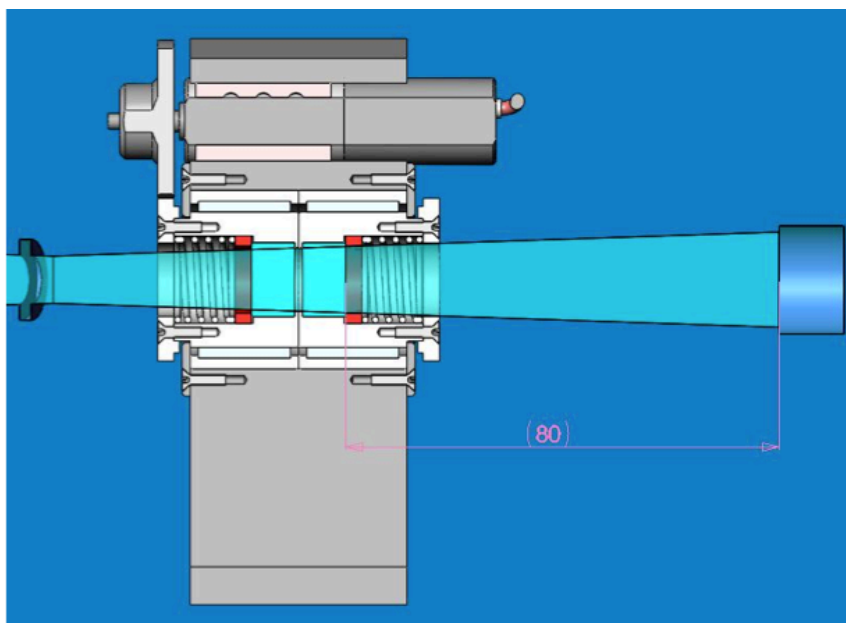


Figure 3.5 The triplet ADC in its mount on the W-Unit optical board. Light enters from the right, passes through the ADC, and forms a pupil to the left in the general vicinity of the beamsplitter/dichroic wheel.

### 3.2.3 VisAO Optics

After passing through the ADC, the light reaches a beamsplitter wheel whose components are listed in Table 3.1. Light reflected from the beamsplitter or dichroic then continues in the VisAO channel where it has the option of passing through a removable Wollaston prism for Spectral Differential Imaging (SDI) (Close et al. 2005). The light then reflects off of a 2-inch diameter silver-coated tip/tilt dither mirror (see Figure 2.3) that can be used to move and center the science target on the CCD47, for example to align a bright central star to the center of a coronagraphic spot. Following the dither mirror, there is a filter wheel containing a suite of circular Sloan filters and a long-pass filter (Table 3.1). Following the Sloan wheel is a baffle tube and then another wheel, which we call the coronagraph wheel. This wheel holds the SDI filter sets and a  $r = 0.2$  arcsec ND3 coronagraphic spot that can be switched in and out based on the science goals.

The last component before the CCD47 is our fast asynchronous shutter. This shutter can serve several purposes. The first is to limit the exposure time for bright objects. For example, our spatial resolution is such that we expect to be able to resolve features on the surfaces of nearby super giants, such as Betelgeuse, which is  $\sim 50$  arcsec diameter at  $\lambda = 700$  nm (Tuthill et al. 1997). A science target this bright will require the fast shutter in order to avoid saturation. A second use of the fast shutter will be for real-time frame selection (RTFS), a technique for blocking low-Strehl light from reaching the CCD47. Simulations of our AO performance using CAOS, an AO simulation code, show that our Strehls in the visible will vary significantly over several hundred ms from as high as 50%

to as low as 10% (Males et al. 2010 and Kopon et al. 2009). By using real-time telemetry to control the fast shutter, we can block the light during periods of low Strehl from

**Table 3.1: VisAO Optical Components**

<b>Position</b>	<b>Beamsplitter (T%/R%)</b>	<b>Filter Wheel</b>	<b>Coronagraph Wheel</b>
<b>1</b>	<b>Bare glass window (96/4)</b>	<b>SDSS z' (0.906 <math>\mu\text{m}</math>)</b>	<b>H<math>\alpha</math> SDI</b>
<b>2</b>	<b>50/50 beamsplitter</b>	<b>SDSS i' (0.761 <math>\mu\text{m}</math>)</b>	<b>[OI] SDI</b>
<b>3</b>	<b>Dichroic (reflect <math>\lambda &lt; 800</math> nm)</b>	<b>SDSS r' (626 <math>\mu\text{m}</math>)</b>	<b>[SII] SDI</b>
<b>4</b>	<b>Dichroic (reflect <math>\lambda &lt; 950</math> nm)</b>	<b>open</b>	<b>Coronagraphic spot pattern “#5”</b>
<b>5</b>	<b>Aluminum puck for taking “darks”</b>	<b>Long-pass “y” (<math>\lambda &gt; 950</math> nm)</b>	<b>Coronagraphic spot pattern “#6”</b>
<b>6</b>	<b>open</b>	<b>-----</b>	<b>open</b>

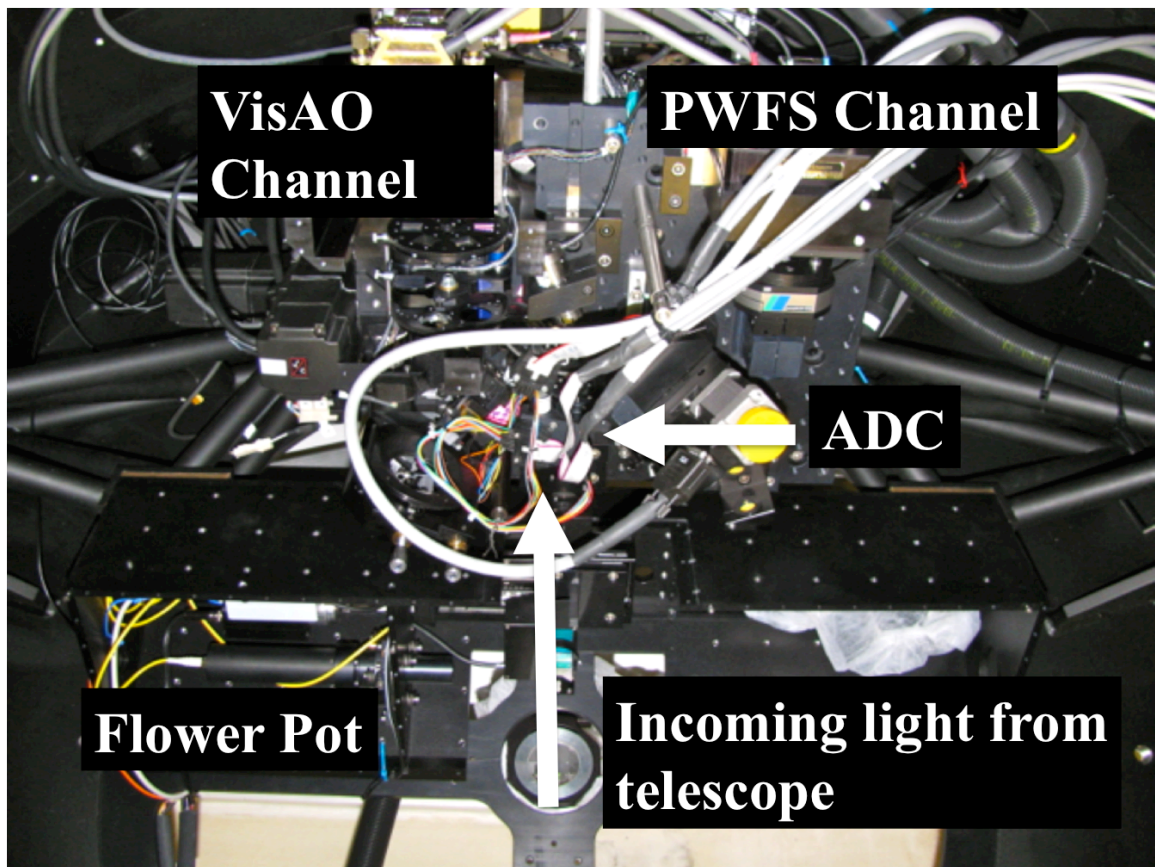


Figure 3.6 The fully assembled W-unit installed in the NAS in Arcetri just before tower testing.



reaching the CCD47. We can therefore achieve the improved resolution of frame selection, combined with the low read noise of a long integration, since the CCD47 is not being read out during this time. For more details on the fast shutter and RTFS, see Males et al. 2012.

### 3.2.4 SDI High-Resolution Imaging

Spectral Differential Imaging (SDI) is a powerful form of speckle suppression that operates by splitting the incoming beam using a low-angle ( $\sim 1.5^\circ$ ) Wollaston prism. This method of beam splitting is useful for high-resolution imaging because it allows both beams to continue on the same optical path, thereby minimizing non-common-path errors to  $\sim 10$  nm rms. By the time the two images reach the focal plane of our camera, they have been deviated by  $\sim 6$  mm, roughly half the size of the focal plane, so they can be imaged in different halves of the same detector. Just before the CCD47, two narrow-band filters can be placed in the coronagraph wheel, each covering half of the focal plane. One of these filters is centered on some wavelength of scientific interest (H $\alpha$  for example) and the other is centered just off of this wavelength at some continuum value. The second image is then subtracted from the first thereby removing the continuum signal and mitigating speckles, revealing whatever faint companions or structures are strongly emitting (or reflecting) the spectral line of interest. For more on specific SDI science cases, see Follette et al. 2010 or Close et al. 2012.

Our Wollaston prism is located on an elevator platform that can raise and lower the prism in and out of the beam. Our initial prototype Wollaston was a custom quartz prism made by Halle in Germany. Because of the low birefringence of quartz, the prism

required a steep ( $\sim 40$  degree) cut angle in order to achieve our required  $\sim 1.5^\circ$  beam deviation angle. This steep cut angle introduced too much astigmatism into the beam. We then proceeded with a prototype calcite prism made by Leysop. The much higher birefringence of calcite allowed a shallow cut angle ( $\sim 3^\circ$ ) that resulted in much less astigmatism, a thinner optic (6 mm), and better image quality.

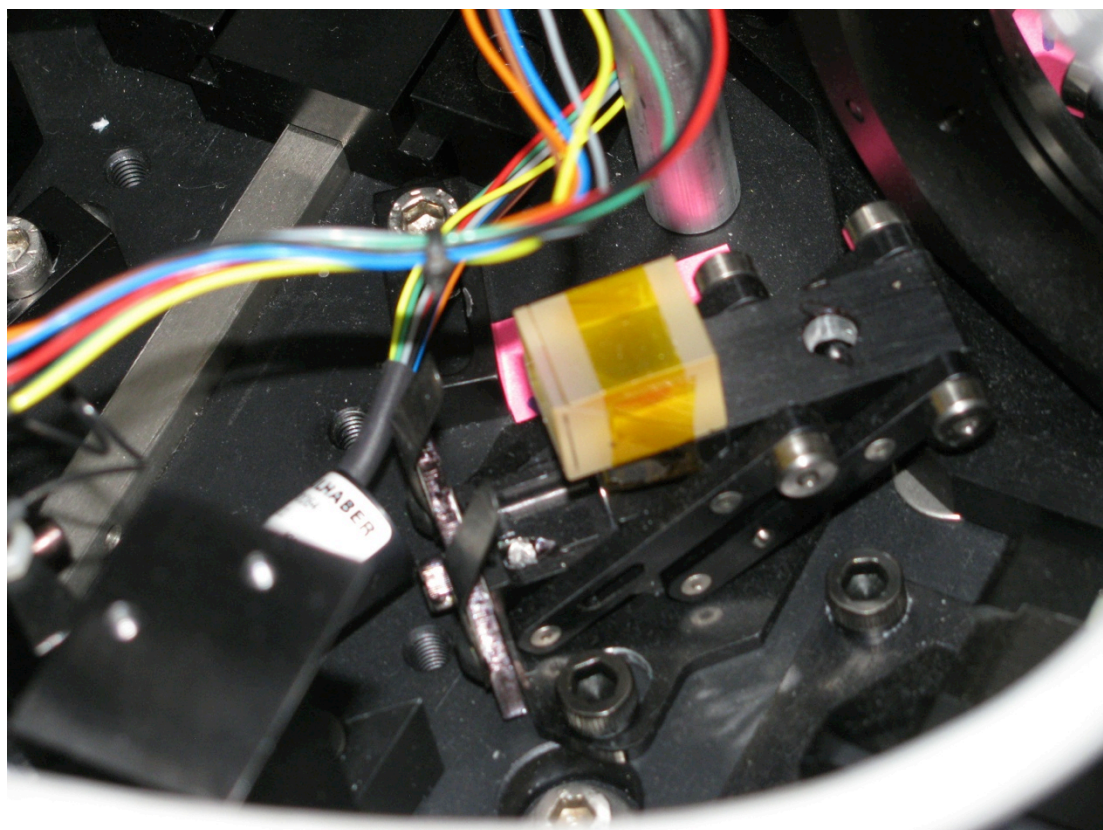


Figure 3.7 The prototype quartz Wollaston prism mounted in the W-unit on its elevator platform for raising and lowering into and out of the beam.

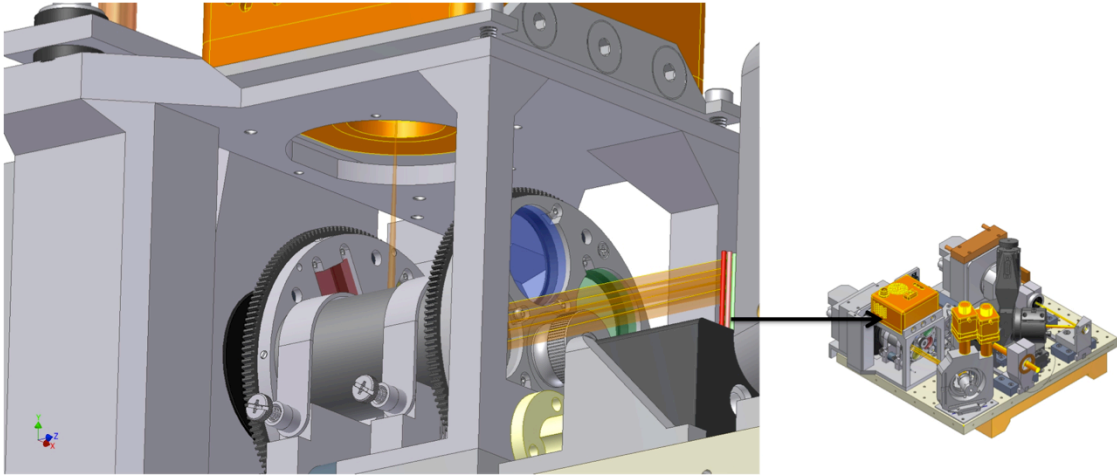


Figure 3.8 Close-up of the Sloan filter wheel, the coronagraph/SDI filter wheel, and the CCD47.

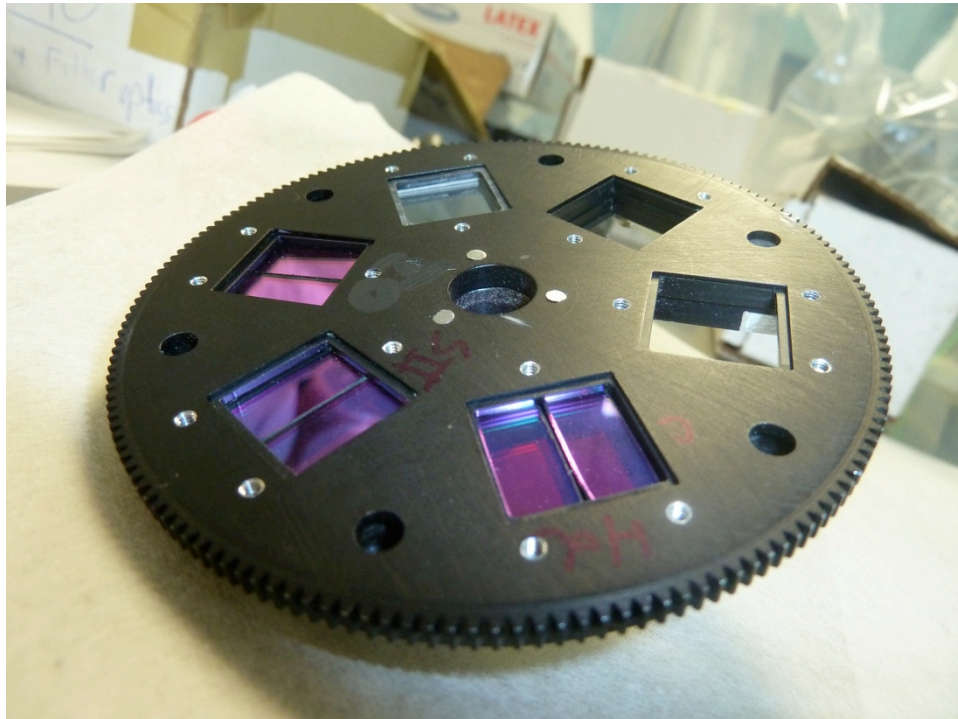


Figure 3.9 The coronagraph wheel with the split SDI filter pairs and one of the chrome coronagraphic spots (at 11 o'clock).

### 3.2.5 Coronagraphic Image Plane Spots

The high spatial resolution and limited FOV of the VisAO camera are specifically well-suited for studying circumstellar structures (disks, jets, etc.) and low-mass companions of stars. Because of this, there is a need to block the bright light of the central star in order to avoid CCD saturation and blooming. To that end, we have designed a series of chrome-on-glass masks that have been optimized for various science cases. For more on chrome-on-glass coronagraphic image plane spots, see Park et al. 2006.

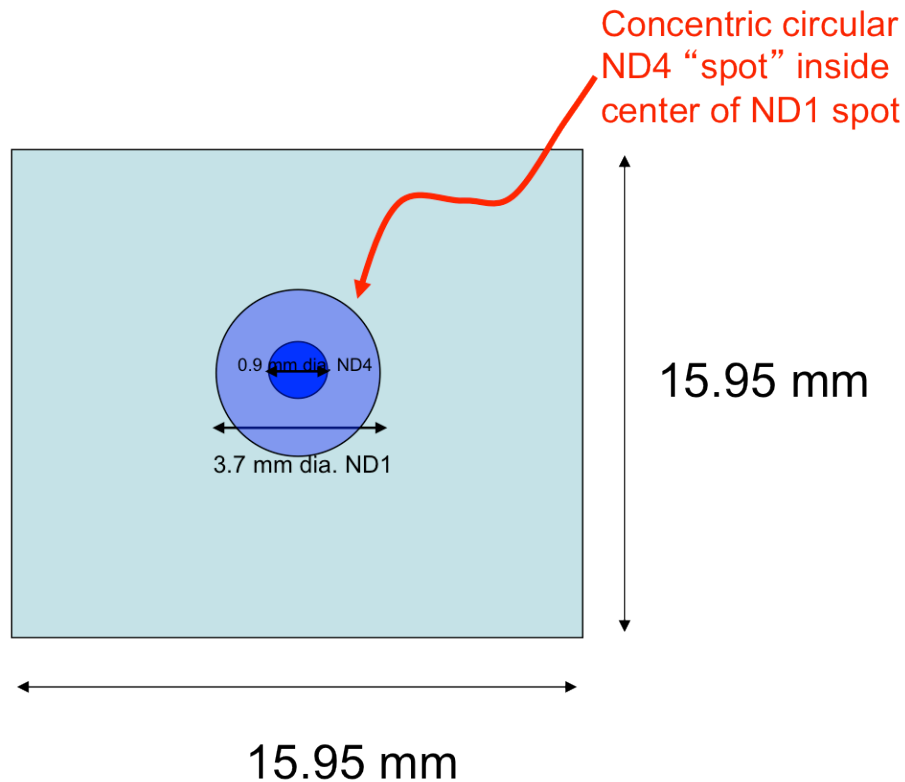


Figure 3.10 One of our custom chrome-on-glass coronagraphic spot designs (not to scale).  $r = 0.1$  arcsec ND4 and  $0.1 < r < 1.0$  arcsec ND1. This design was fabricated incorrectly by the vendor and is currently not being used.

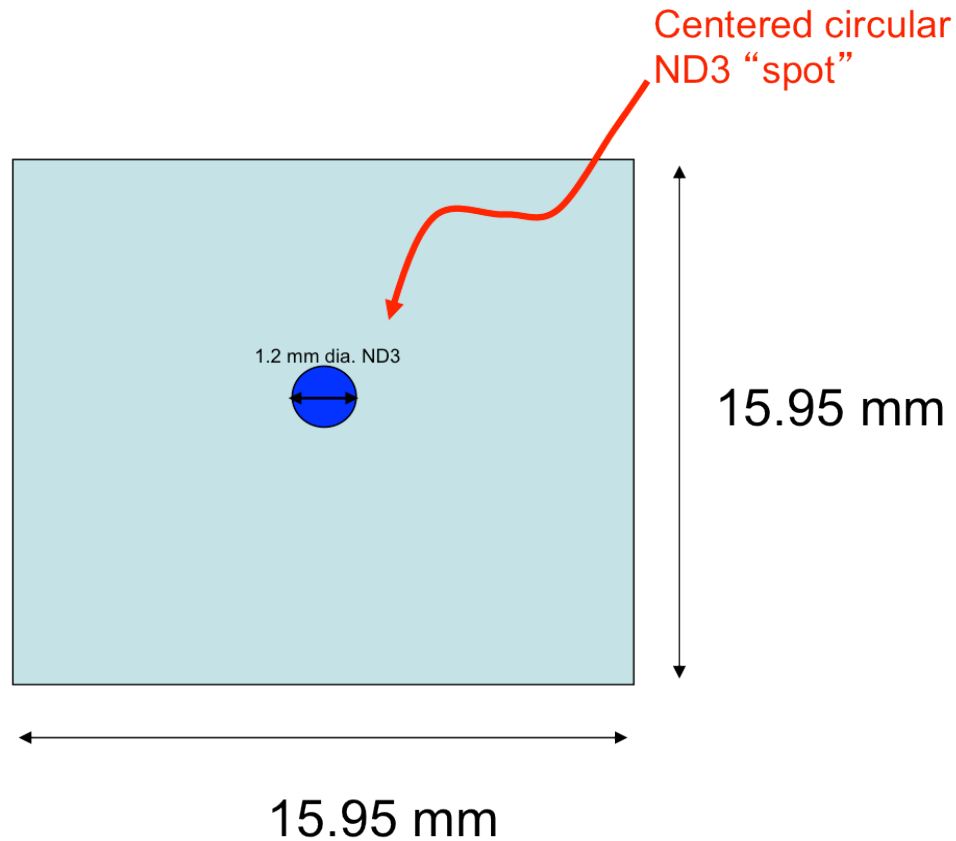


Figure 3.11 The chrome spot pattern  $r = 0.2$  arcsec ND3 chrome on glass.

### 3.3 The Arcetri Tower Tests

From the summer of 2011 through the spring of 2012, the Magellan AO system (the ASM, W-unit, and other hardware) was in Florence, Italy undergoing testing in the Arcetri solar test tower. The Arcetri test tower (Figure 3.12, right) is tall enough (14 m) to allow the ASM to be tested at the same focal distance that it will be used at the Magellan telescope (see also Figure 5.2). The ASM is mounted at the top of the tower and either a 4D interferometer or the W-unit inside the NAS is mounted at the base. Because the ASM is a concave ellipsoid, as required by Magellan's Gregorian design, a

retro-reflecting optic, which we call the Calibration Return Optic (CRO), is mounted at the short ellipsoidal conjugate. This enables a double-pass optical test to be performed.

The 4D interferometer is a simultaneous phase-shifting interferometer that allows interferometric measurements of the secondary surface to be made quickly and reliably in a noisy environment. This setup is used initially to “flatten” the ASM, i.e. to determine the actuator forces required to shape the ASM shell into its nominal ellipsoidal shape and to measure the actuator influence functions. The 4D is then replaced with the NAS (our name for our large mechanical support structure, see Figure 3.1) that holds the W-unit and a white-light fiber source calibration unit called the “flowerpot” (Figure 3.6). The flowerpot fiber is used to stimulate a star that is reflected off of the ASM, then the CRO, then back to the ASM, and finally reimaged at the F/16 focal plane before entering the W-unit, which contains the PWFS and the fully integrated VisAO camera. This setup allows us to run the AO system in closed loop. Turbulence can be simulated using the ASM itself by injecting a pre-calculated phase screen in addition to the AO corrections. This phase screen is designed to simulate a conservative seeing of the Magellan site (FWHM of 0.8” at  $\lambda = 550$  nm, or  $r_0 = 0.14$  m). For more on how turbulence is simulated with the ASM, see Esposito et al. 2010. This test is discussed in more detail in Chapter 5.



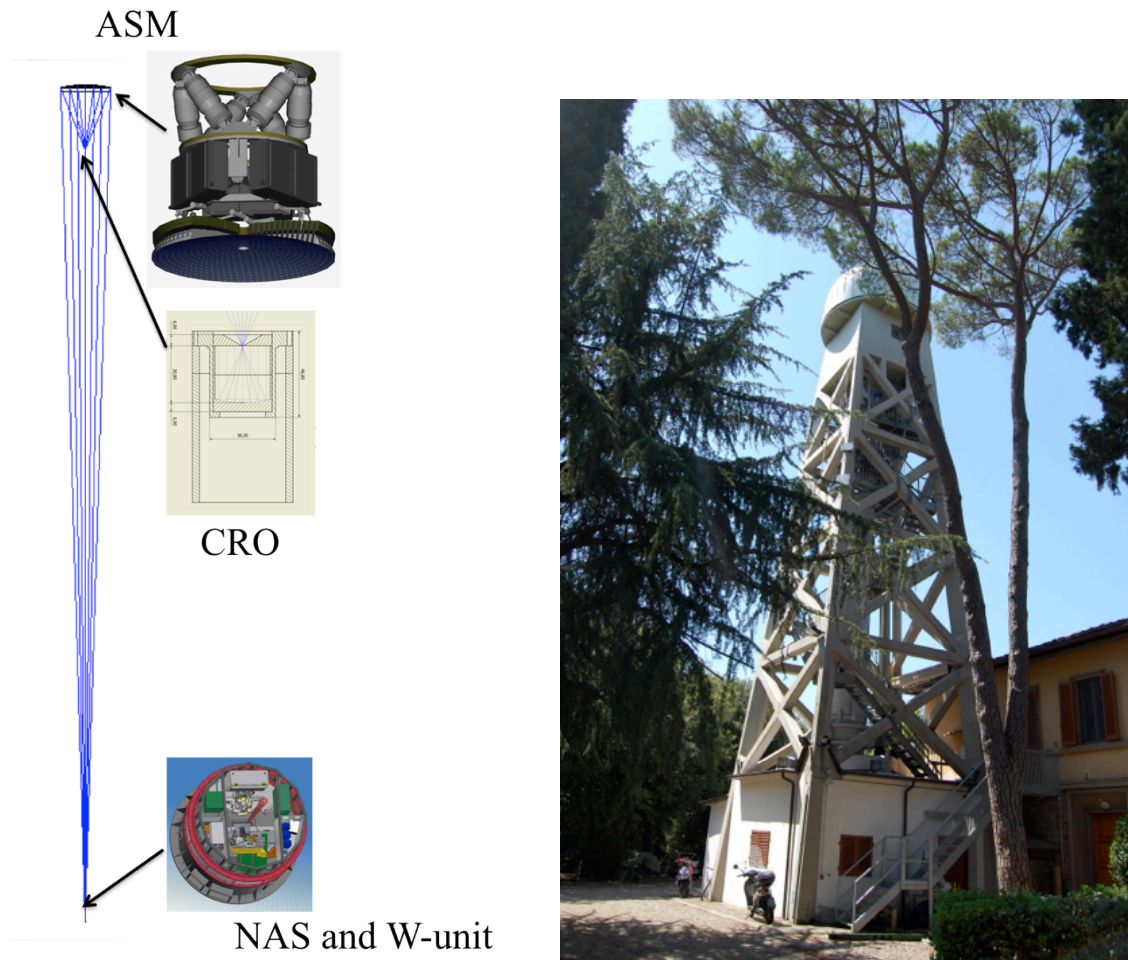


Figure 3.12 The ASM test setup in the Arcetri test tower. The concave secondary allows for a relatively simple double-pass optical test configuration at the same focal length that will be used at the telescope. A calibration source in the NAS at the far focus reflects off of the ASM, then the CRO, then back to the ASM before entering the W-unit for wavefront sensing and technical viewing.

### 3.4 Results

We tested the full AO system in the test tower in a wide variety of wavelengths, levels of turbulence, PWFS binning, etc. By mounting the ASM in the top of the tower and placing a retro-reflecting optic at the short conjugate of the concave ellipsoidal secondary mirror, the entire system can be tested at the nominal ASM focal length in closed loop, without the need for a 6.5m primary mirror. In addition to the vibration of the test tower, additional turbulent “seeing” can be injected into the ASM in order to simulate conditions on the sky at the Magellan telescope in Chile. The AO system can then be used in close loop to remove this turbulence.

The full AO system with all of the optical components, including the ADC in its non-dispersive orientation, performed as predicted with excellent image quality at  $\lambda = 982$  nm and Strehls of 85%. This is excellent performance and should allow us to meet our VisAO science goals.



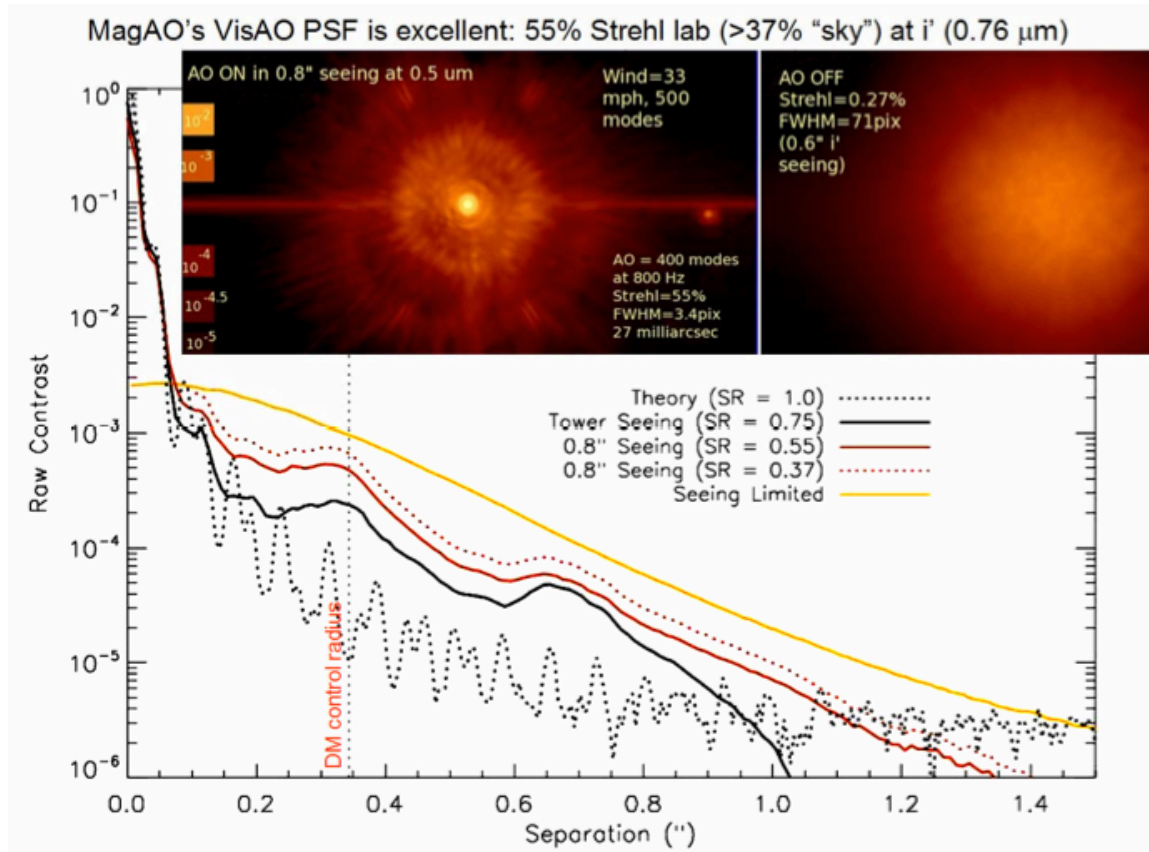


Figure 3.13 Real closed loop end-to-end tower tests of MagAO at i' (0.76  $\mu\text{m}$ ) with VisAO camera. Inset left: A deep 120s exposure with AO "on" (400 controlled modes, 800 Hz) with 500 modes of injected 0.8" V band seeing and 33 mph winds with  $L_0 = 40$  m ( $R = 8.1$  mag "star"). This gives raw Strehl = 55%, which "corrects" to > 37% (122 nm) when considering that mirror fitting error is missing modes >500). Inset right: AO "off" (ASM in nominal position) with same seeing. Yields SR of 27%. These results show there are no significant ghosts in the image. In >75<sup>th</sup> percentile seeing we will achieve > 37% Strehl at i' with bright ( $R < 10$ ) guide stars. From Close et al. 2012.

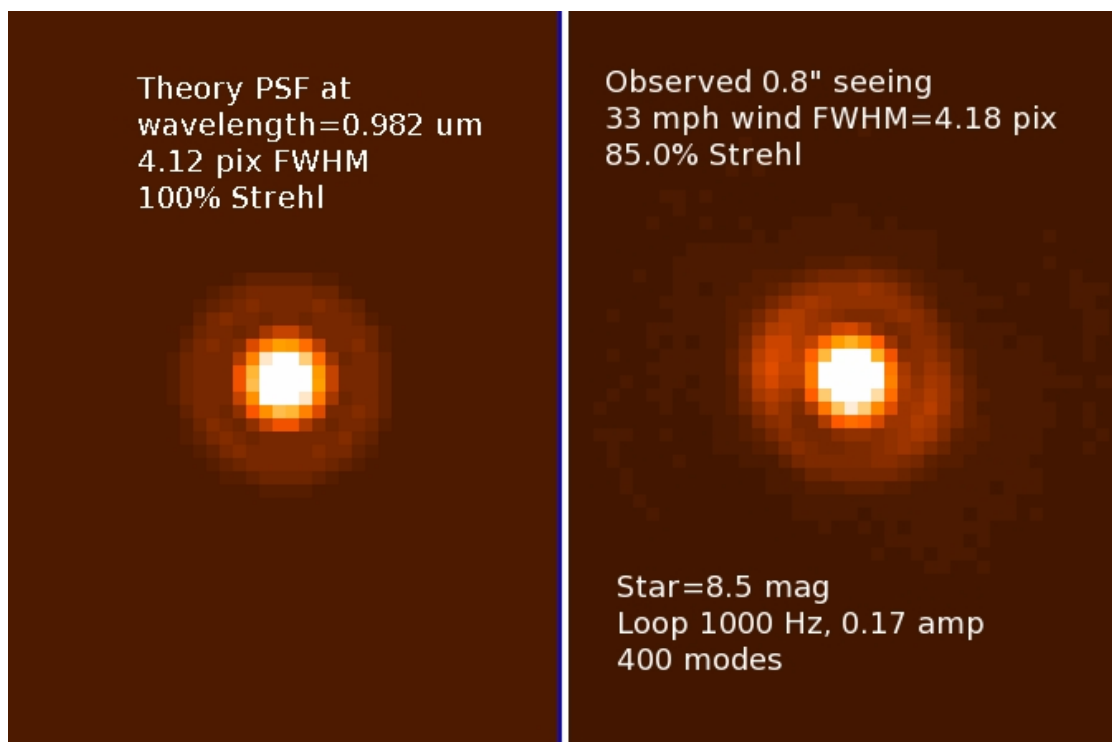


Figure 3.14 Closed loop performance at 982 nm of the complete AO system in the Arcetri test tower. Left: Theoretical PSF at F/52 and 982 nm. Right: AO corrected image of the fiber source with the tower vibration, ambient environment, and injected “seeing” as the sources of turbulence.

### 3.5 Conclusion

The Magellan AO system, recently having passed a successful pre-ship review in Florence, Italy, is scheduled for first light on the Magellan Clay telescope in November 2012. The excellent seeing of the Magellan site, combined with a high-performance adaptive secondary AO system whose capabilities have already been demonstrated with the virtually identical LBT system and with our own tower tests, will provide unprecedented high-resolution images of targets in the southern sky in both the visible and mid-IR bands. The VisAO camera will demonstrate many novel techniques for achieving this high resolution in the visible, many of which are discussed in this

dissertation. These include the advanced triplet ADC, the fast asynchronous shutter for real-time frame selection, the calcite Wollaston prism and corresponding filters for SDI imaging, and our custom chrome-on-glass coronagraphic spots.

## CHAPTER 4

### THE MOVABLE GUIDER PROBE: WIDE-FIELD AND SHACK-HARTMANN GUIDING

*This chapter consists of work originally published by Kopon et al. in the 2009 and 2010 Proceedings of the SPIE. The wide-field lens is my original design. I procured the optics for the wide field lens, assembled it, tested it in the lab, and assisted in installing it on the telescope. The Shack-Hartman wavefront sensor is a modification of a pre-existing Magellan design. I procured a lenslet array from the German company SUSS that has better image quality and a larger format than the AOA lenslet arrays currently used on the other Magellan guiders. I designed the zero-stress invar cell in which the lenslet array mounted (not discussed here). I assembled the SH optics and assisted in installing them on the telescope.*

Each Magellan instrument has its own guider assembly or assemblies, each serving as both a wide-field acquisition and guiding camera and active optics low-order wavefront sensor (Schechter et al. 2002). The guider assemblies have pneumatic slides that switch back and forth between two sets of optics: wide-field imaging optics for acquisition, guiding, and seeing estimates; and a Shack-Hartmann mode with a collimating double lens that reimages the pupil onto a lenslet array in front of the CCD. All of the Magellan guiders currently on the mountain make use of off-the-shelf SLR camera lenses for their wide-field imaging (Figure 4.6). The optical quality of these lenses limits the image quality of the guide camera to 0.4 arcsec FWHM. Since this is of the same magnitude as the seeing, these cameras cannot effectively measure the seeing on good nights. The layout of our guider ring with the positions of the guider probe is shown in Figures 4.1 and 4.2.

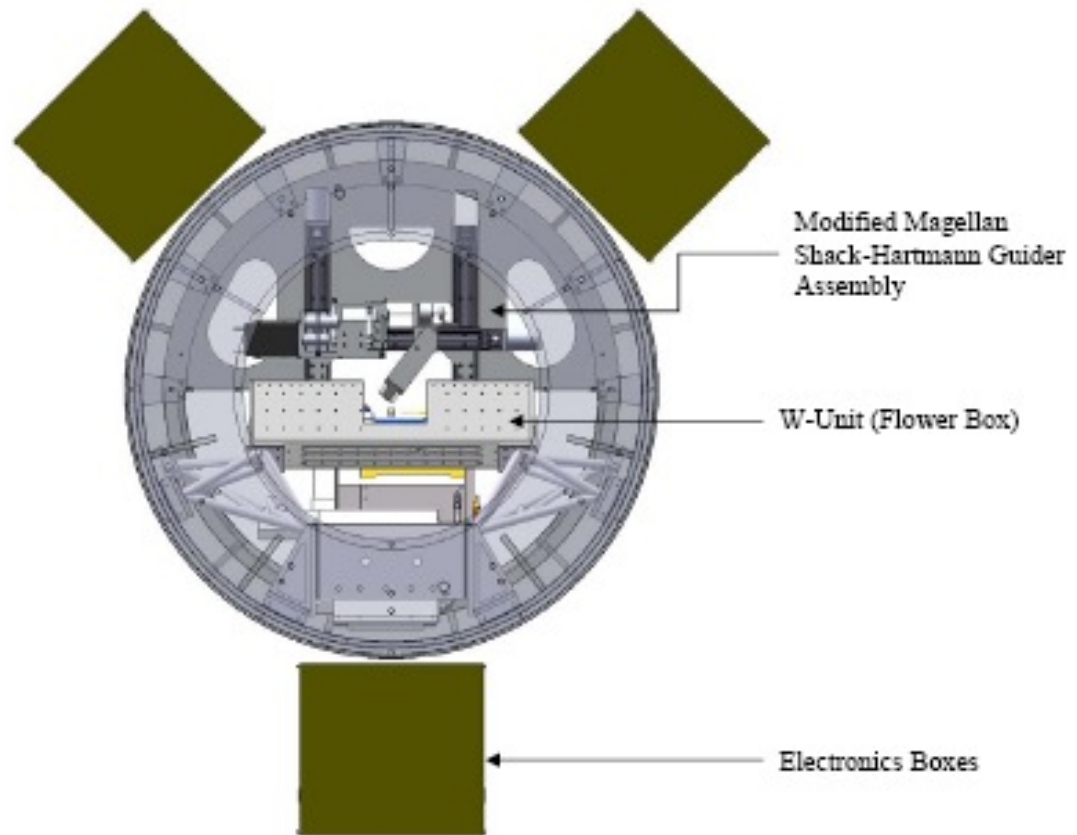


Figure 4.1 The Nasmyth assembly with the W-unit and guider probe.

To overcome this limitation, we have designed a new custom 50" FOV acquisition camera that can be placed in the center of the field (Figures 4.3 and 4.7). The image quality of the new wide-field lens design ( $\sim 0.1$  arcsec) is significantly better than seeing-limited over its 50" field. The wide-field lens is in a tube that is on a mechanical slide that can move in front of the CCD when wide-field acquisition mode is desired. The lens group operates at F/8.25 (giving  $0.05''/\text{pix}$  on each  $13\mu\text{m}$  pixel, but really  $0.10''/\text{pix}$  since  $2\times 2$  binning is standard) and is well corrected for chromatic aberration over the band 550-850 nm. The end of the tube holds a filter that limits the transmitted light to this spectral range. The pneumatic slides allow us to switch easily from the wide-field lens to the SH

mode and back. The spot diagram in Figure 4.4 shows the optical quality of the wide-field camera design. The black square is the size of one of the Magellan 1k x 1k E2V CCD pixels (0.1" x 0.1" when used in standard 2x2 binning). This design residual is far better than even the best ( $\sim 0.25''$ ) optical seeing conditions that are possible at the telescope. Figures 4.8 and 4.9 show that the wavefront quality is excellent over the full field of view and the design wavelengths and the field curvature and distortion is low ( $\sim 1\%$ ). We have also changed the focal length of the collimating lens of the Shack-Hartmann E2V CCD to accept the F/16 beam of our secondary mirror, instead of the standard Magellan F/11 beam. Figure 4.5 shows a photo of the fabricated optics. Figures 4.10 and 4.11 show the full guider assembly installed at the Nasmyth platform at the Magellan telescope. Figure 4.12 shows that the vignetting of the guider probe is only  $\sim 10\%$  at the edge of the field.

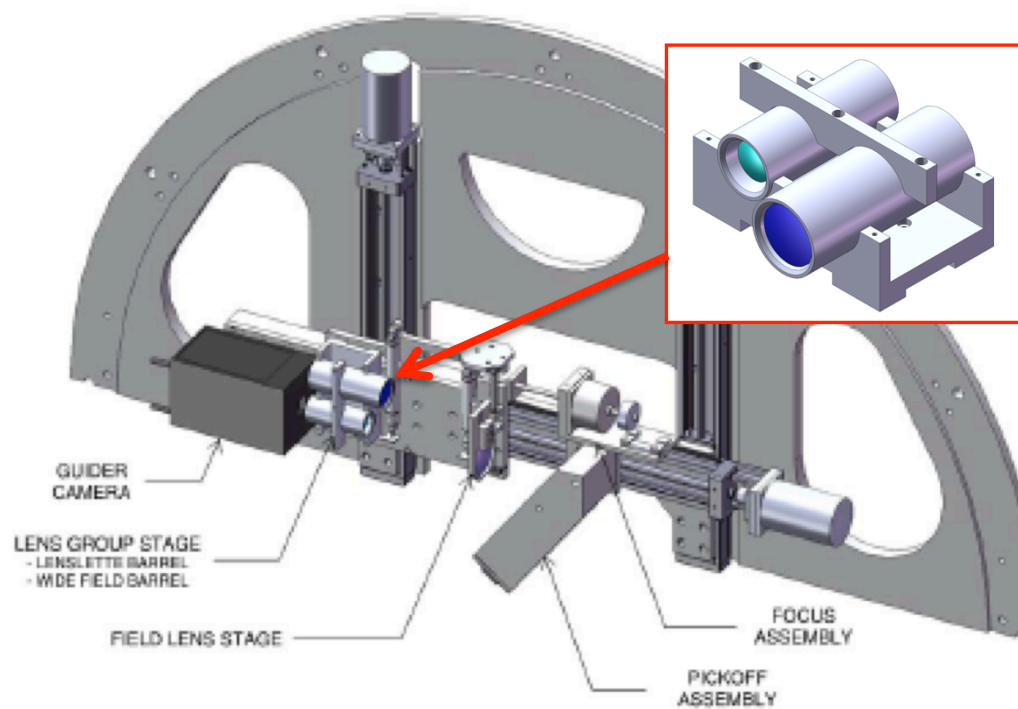


Figure 4.2 The guider assembly. The pickoff mirror sends light from a star within the patrol field to the focus assembly and then the lens group stage where the beam passes through either our custom wide-field lens or a collimating lens followed by a lenslet array for Shack-Hartmann wavefront sensing. Both modes use the same 1k x 1k E2V CCD.

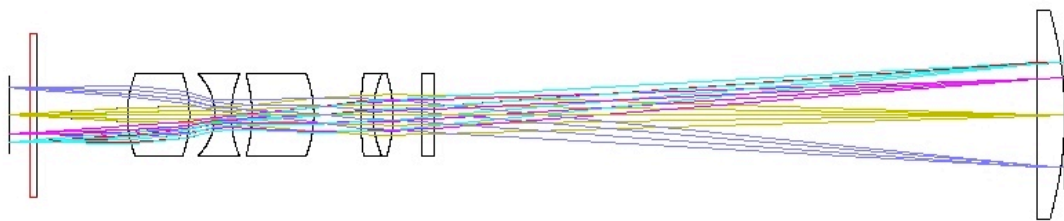


Figure 4.3 Ray trace of our 50" FOV acquisition camera. Light enters from the right through the field lens, which is on a separate mechanical stage at the F/16 Magellan focus. The smaller lenses are in a lens tube that can be moved in and out of the beam to switch between the wide-field imaging mode and the Shack-Hartmann mode.

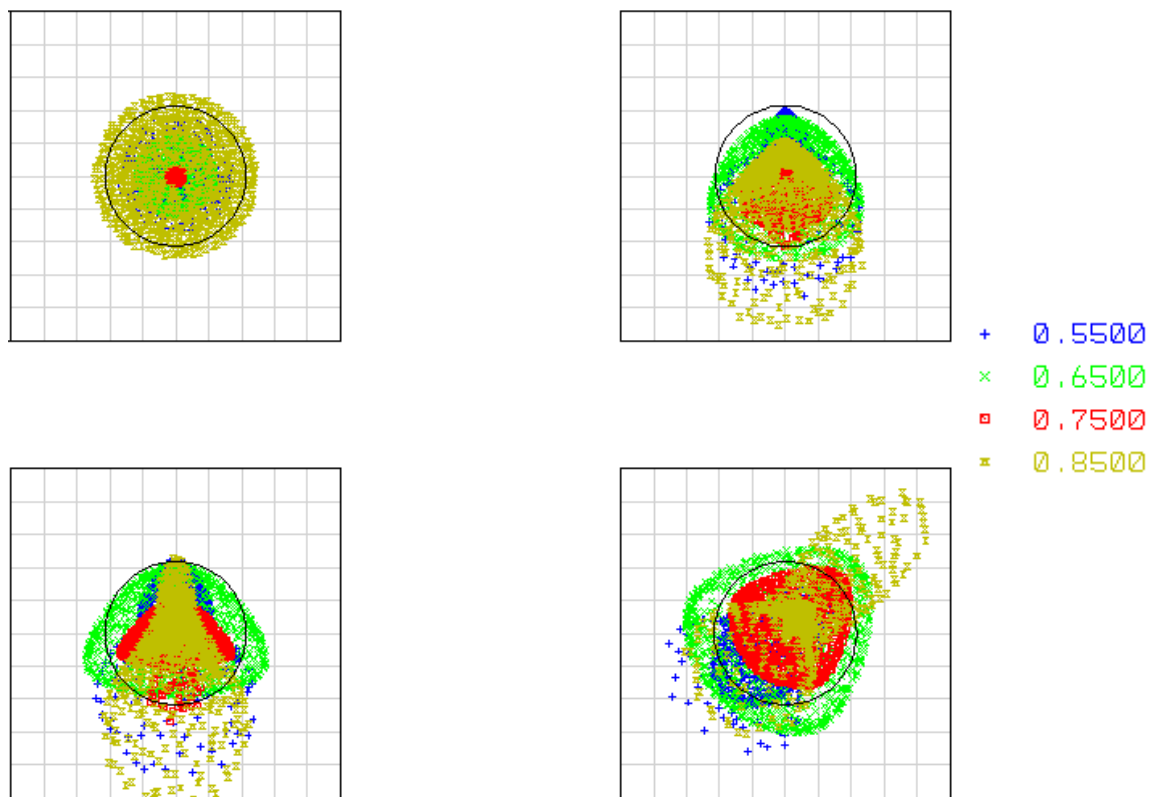


Figure 4.4 Spot diagrams for the wide-field lens over the band 550-850 nm. From top left to bottom right: on-axis, 7/10 field point, CCD edge (25" from on-axis), and CCD corner. The black circle is the 550 nm diffraction limit. The black square is 0.1 arcsec on a side.





Figure 4.5 The custom wide-field singlet lenses (and spares), filter, and lens tube.

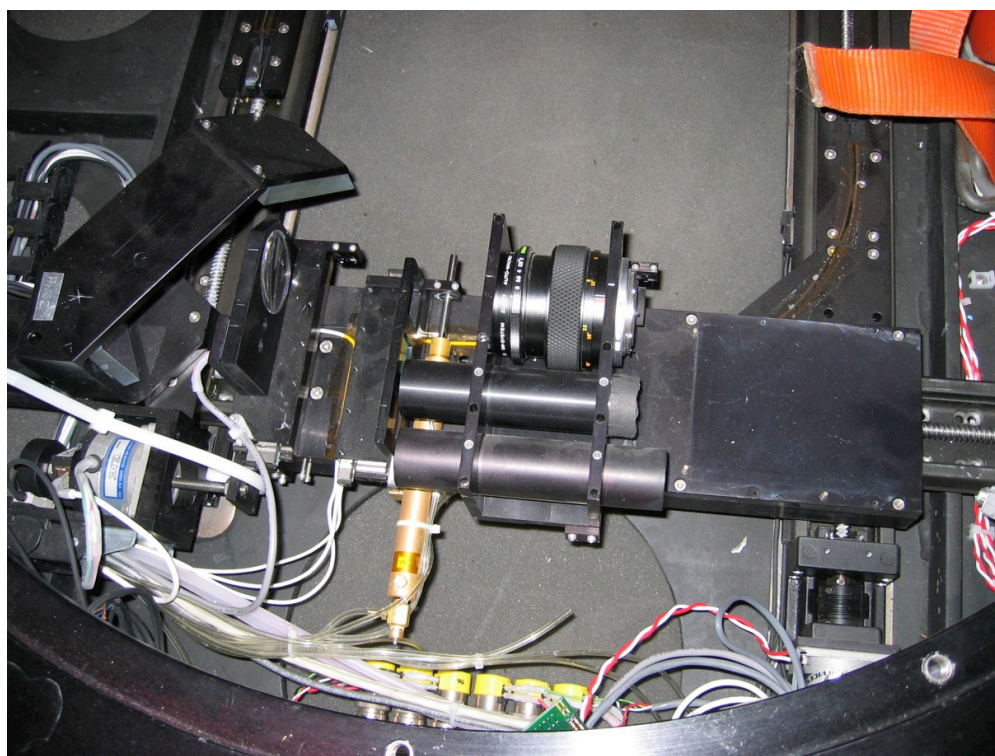


Figure 4.6 “Old” Magellan guider probe assembly. The off-the-shelf SLR wide-field lens is generally worse than seeing-limited on good nights.

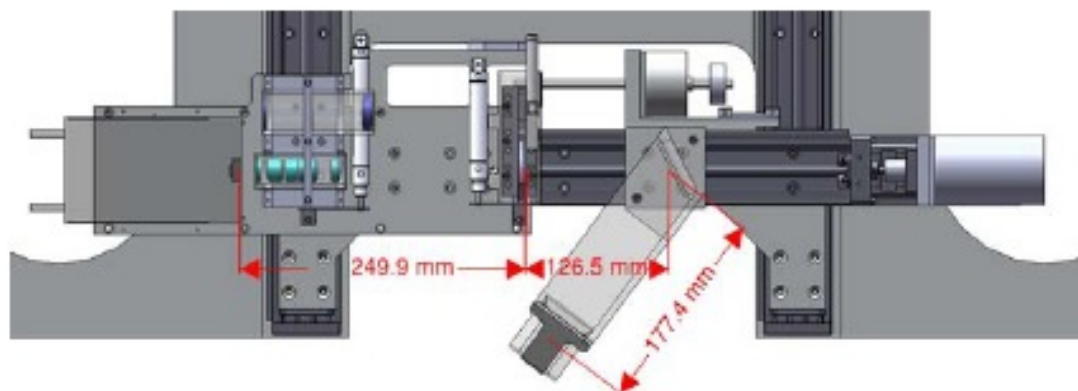


Figure 4.7 New guider model with custom wide-field lens.

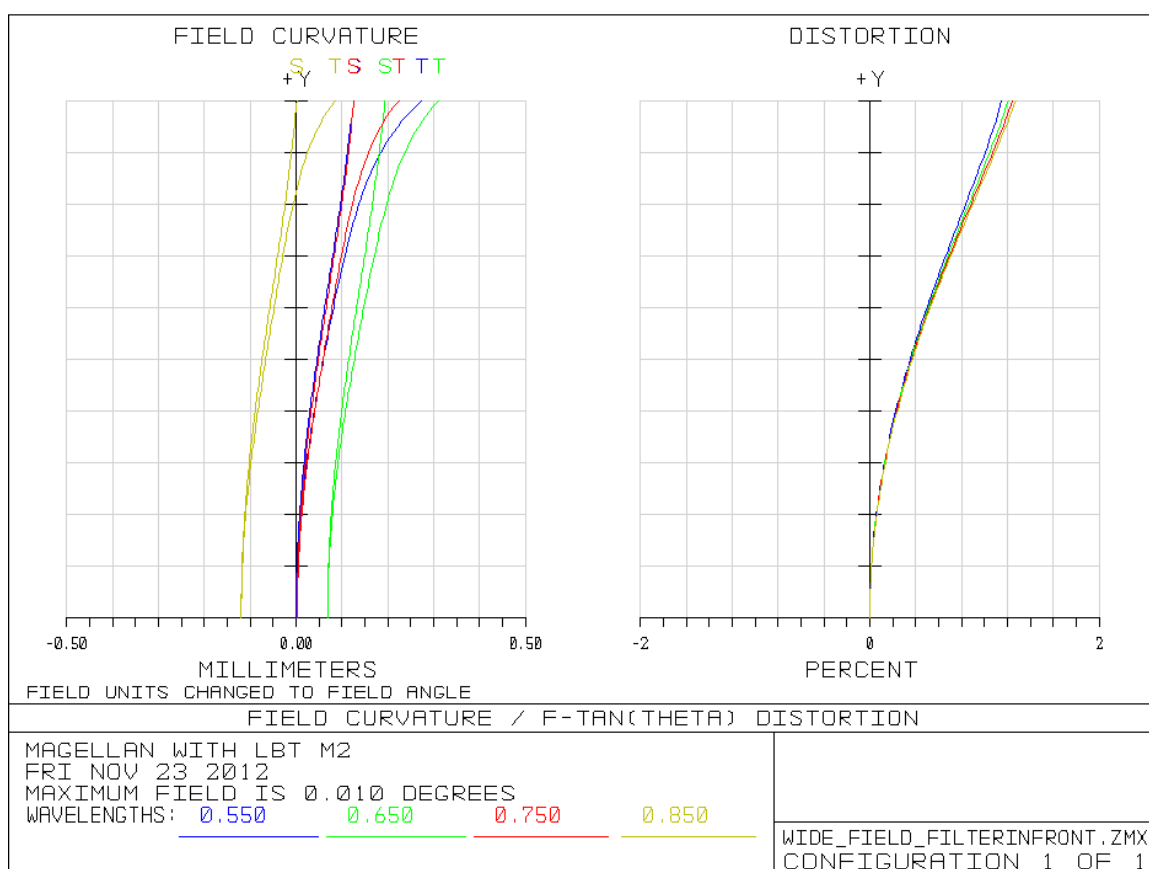


Figure 4.8 Field curvature and distortion of the wide-field guider lens. The lens has low distortion, low field curvature, and ~0.1" image quality, significantly better than seeing-limited.

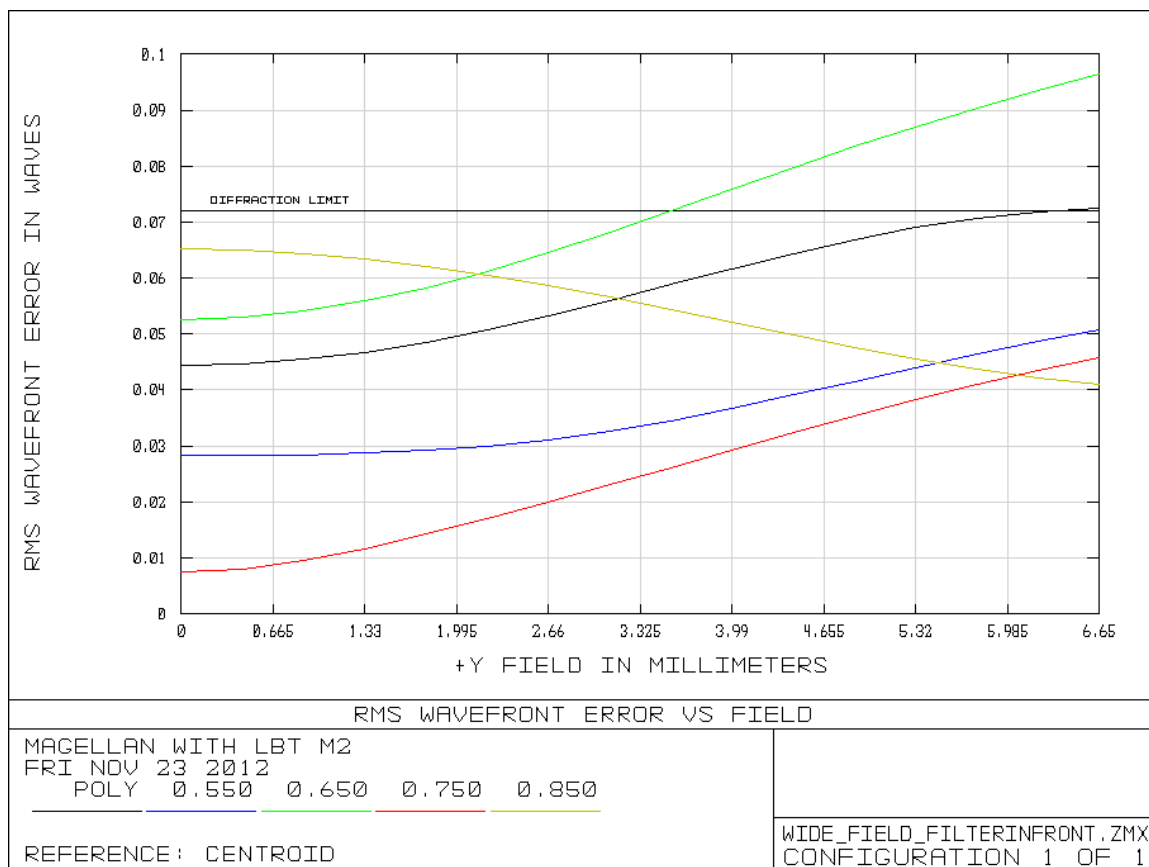


Figure 4.9 The rms wavefront error over the full 50 arcsec field of view and the wavelength band 550-850 nm. The horizontal black line is the diffraction limit and it is higher than all the wavelengths and field angles, except for 650 nm at the very edge of the field. The image quality at all wavelengths and field angles is better than the seeing limit.

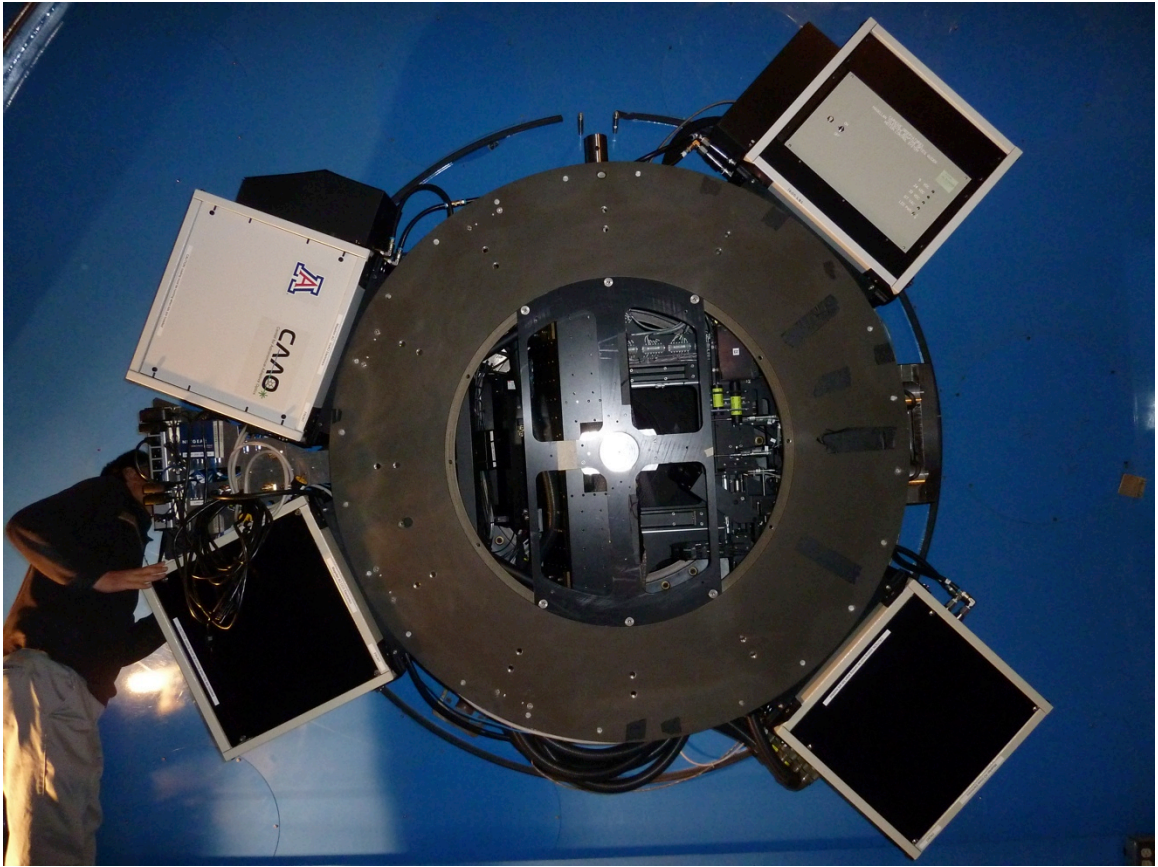


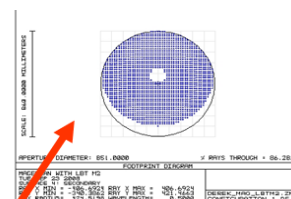
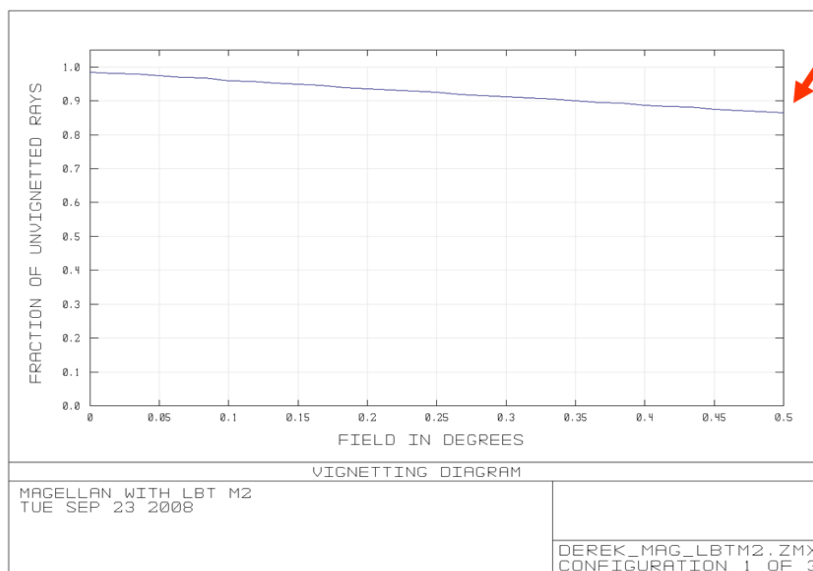
Figure 4.10 Fully assembled NAS with the W-Unit and guider assembly installed and mounted on the Magellan telescope.





Figure 4.11 Zoom in of Figure 4.10 showing the guider assembly. The wide-field lens and SH tubes are shown in yellow.

## Critically sized secondary: Vignetting vs field angle



At the very edge of the Magellan field (30' off-axis) there will be ~10% of SH spots on the guider not illuminated.

NB: For IMACS SH is >20% vignetted

Figure 4.12 Vignetting as a function of field angle for the guider probe.

## CHAPTER 5

### THE CALIBRATION RETURN OPTIC TOWER TEST

*This chapter contains work originally published by Kopon et al. in the 2009 and 2012 Proceedings of the SPIE and in the MOAP-004 Magellan CDR design document. Our collaborators at Arcetri designed the CRO itself and the double pass optical test. My contribution was to recognize the difference between the LBT and Magellan secondary mounting schemes and to identify the need for the CRO truss, the gun-laser alignment scheme, and the remotely actuated CRO stage. The CRO truss, the gun laser alignment scheme, and the CRO remotely actuated magnetic kinematic mount are my original designs.*

As noted in Chapter 3, because the ASM is a concave ellipsoid, its surface can be tested by placing an interferometer or calibration source at the far focus and a retro reflector, which we call the calibration return optic (CRO), at the near focus (Figure 5.1). This interferometric measurement can be used to calibrate the interaction matrix of the system and determine the best actuator settings that “flatten” the mirror (i.e. make it into as perfect an ellipsoid as possible, see Figure 5.2). The CRO test can also be used with a white-light fiber source and the pyramid wavefront sensor, instead of the interferometer, in order to run the ASM and wavefront sensor in closed loop (without the need for natural star light).

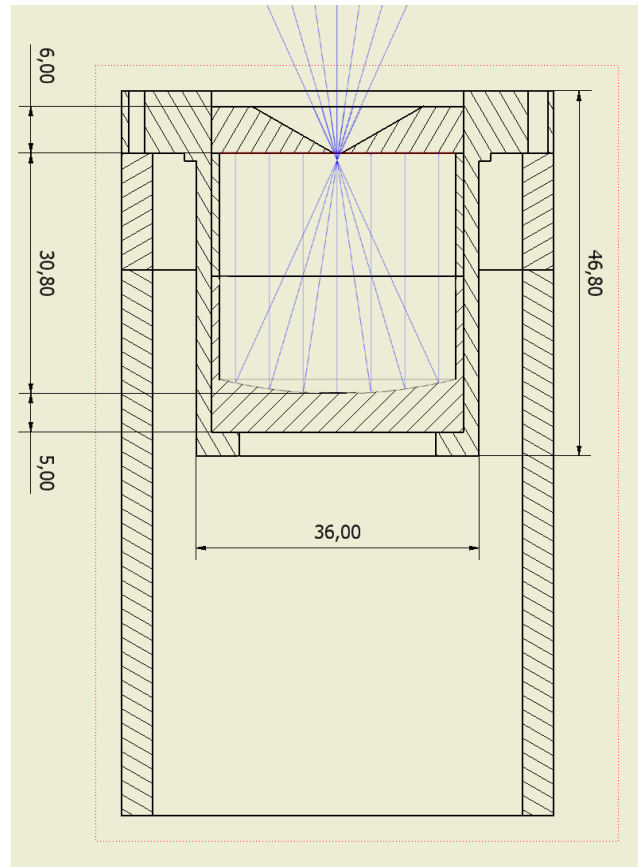


Figure 5.1 Raytrace of the CRO. The incoming F/1.25 beam is collimated by an on-axis paraboloid, reflected off of a flat, and then returned to the secondary. Dimensions in mm.

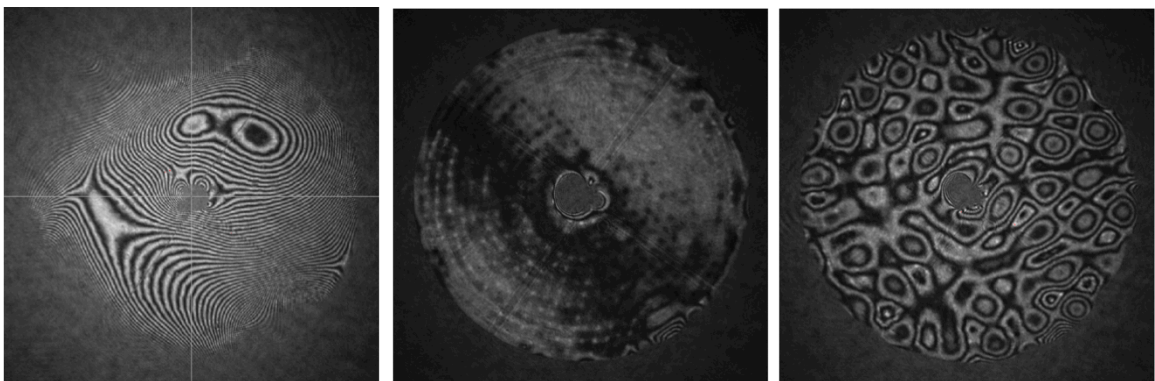


Figure 5.2 Fringes off the LBT ASM from the simultaneous phase-shifting interferometer. The CRO is used for a double-pass optical null test. Left: The shell before flattening. The surface is so far from its nominal shape that fringe coherence does not extend to the edge of the optic. Center: The ASM after being flattened. Right: An example of a higher order mode being applied to the ASM. Courtesy of Armando Riccardi.



## 5.1 Test Setup and Design Challenges

The  $\sim 13:1$  focal ratio between the near and far ellipsoidal conjugates means that the near focus is extremely sensitive. A  $1\text{ }\mu\text{m}$  movement at the near focus results in a  $13\text{ }\mu\text{m}$  movement of a reimaged point at the far focus. Because of this, the retro-reflecting optic (the CRO) is extremely sensitive and must be precisely aligned.

This double-pass CRO test was performed initially during system calibration at the solar test tower at the Arcetri Observatory (Figures 5.3 and 5.4). We also plan to retain the ability of performing this test on the Magellan telescope, particularly during commissioning. In the Arcetri tower, the CRO is stationary with respect to the tower and the ASM is aligned to the stationary CRO using a hexapod identical to the hexapod used on the LBT (Figure 5.5). Likewise, at the LBT, the CRO is stationary with respect to the telescope structure and the ASM can be moved by its hexapod. Because we will not have a hexapod at Magellan that can move the ASM relative to the CRO, it is necessary to build in the added functionality of moving the CRO remotely in order to align it to the ASM (see Figures 5.6 and 5.7). We fabricated a structure that attaches to the windscreen surfaces on the ASM that can hold the CRO near the focus (Figure 5.8). The structure also supports a 5-axis (XYZ,  $\theta X$ ,  $\theta Z$ ) remotely controlled fine adjustment stage ( $2\text{ }\mu\text{m}$  over  $3\text{ mm}$ ) that can move the CRO relative to the ASM. The CRO and its stage will be repeatably kinematically removable in order to allow us to easily switch back and forth between the CRO test and an on-sky test during commissioning.

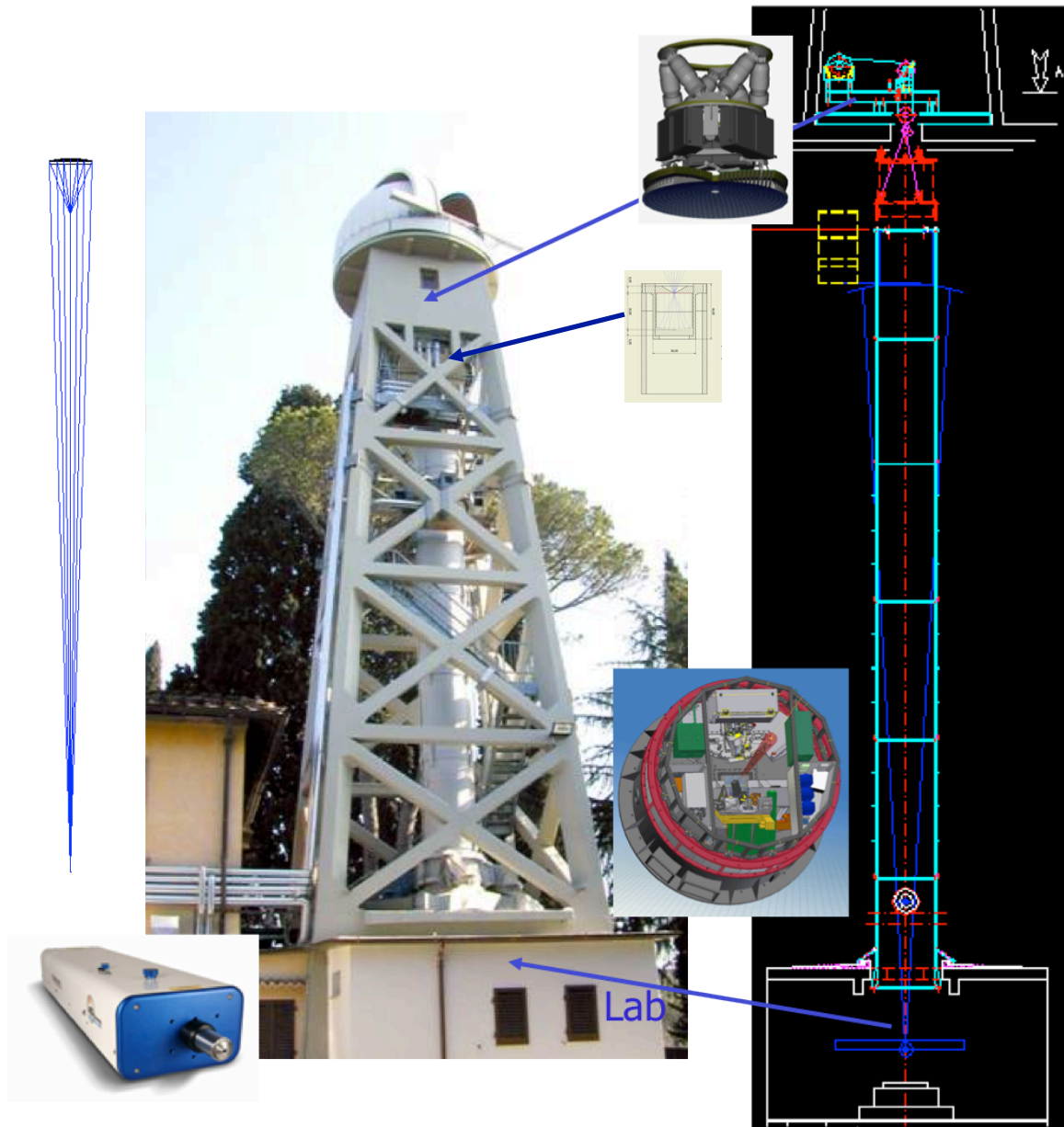


Figure 5.3 The Arcetri test tower. The ASM is raised up through the tube from the lab at the base with the CRO attached to it by the CRO truss. Inset left: the 4D simultaneous phase-shifting interferometer, which is used for shell verification and flattening.



Figure 5.4 The view looking up the tower from the base to the ASM. Because the viewer is located close to the far ellipsoidal conjugate, our view is conjugated to the surface of the CRO. The large “hole” that is imaged in the secondary is the entrance to the CRO, which is actually only a few mm in diameter.



Figure 5.5 The LBT hexapod that is used to align the ASM to a stationary CRO. We will not have such a luxury at Magellan.



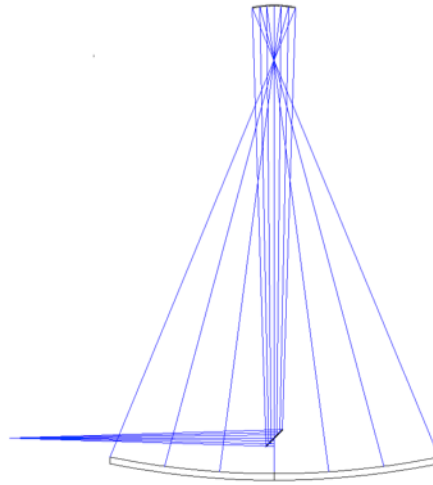


Figure 5.6 Raytrace of the Magellan telescope. When the CRO is removed, light from a star can pass through the telescope to the focal plane.

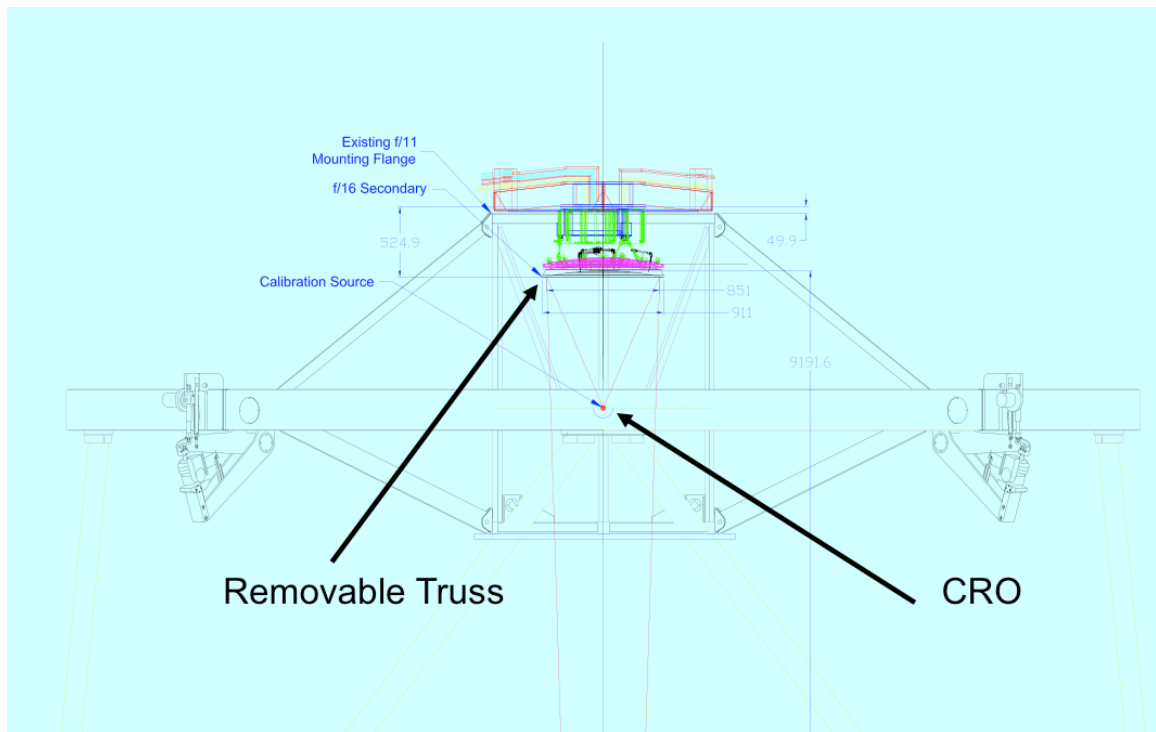


Figure 5.7 The ASM mounting structure at the Magellan telescope. Because the secondary does not have a hexapod like that of the LBT, the CRO must be remotely adjustable in order to align it to the ASM.

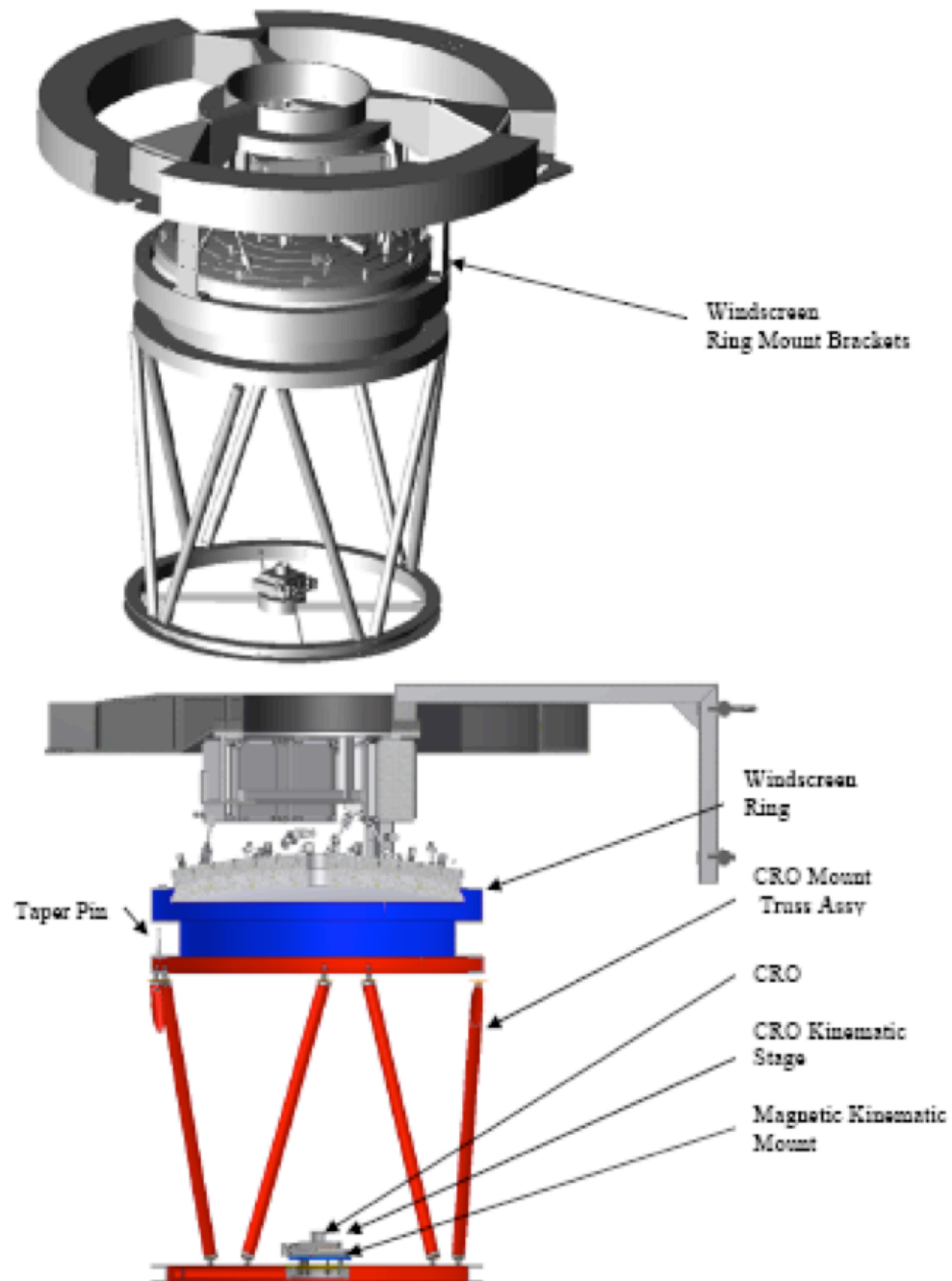


Figure 5.8 The ASM and CRO truss assembly. This setup is unique to the Magellan system and contains a remotely actuated CRO that can be aligned to the ASM optical focus to micron-level precision.

Another challenge posed by the Magellan CRO test is that the windscreen, CRO truss structure, and ASM L-brackets do not have repeatable interfaces. Therefore, after we achieve our exquisite  $2\text{ }\mu\text{m}$  alignment in the Arcetri test tower, that alignment will be completely lost once the structure is disassembled and shipped to Chile. In order to overcome this obstacle, we designed a rail-mounted laser fiducial that both retains the information of the CRO alignment and serves as a boresight reference for use during commissioning at the telescope.

## 5.2 CRO Cup and Mount Design

As stated earlier, the CRO is very sensitive optic and must be aligned to better than  $\sim 2\text{ }\mu\text{m}$ . In addition to achieving this precise alignment, we desire the ability to remove and repeatably replace the CRO so that we can go back and forth between the off-sky artificial source test and looking at a star on-sky.

To that end, we designed a layered stage that holds the CRO and meets all of these design requirements. The CRO sits in a cup, which mounts to a 5-axis piezo stage that can be remotely actuated to achieve the fine alignment (Figure 5.9). The 5-axis stage bolts to a steel plate, which in turn bolts to another steel plate that mounts to the CRO truss structure. The interface between the piezo stage and the first steel plate has slotted holes for coarse adjustment in one direction. The first and second steel plates interface via over-sized holes and large washers that allow coarse adjustment in the plane of the mount. Finally, the second steel plate interfaces with the CRO truss via 3 steel tooling balls that sit in 3 grooves (Figure 5.10). The three grooves are oriented  $120^\circ$  apart and provide a repeatable 6-point kinematic mount in order to minimally constrain the six



Figure 5.9 The precision 5-axis piezo stage. The CRO cup mounts directly to the stage, which in turn mounts to a series of plates that provide coarse adjustment over a larger range.

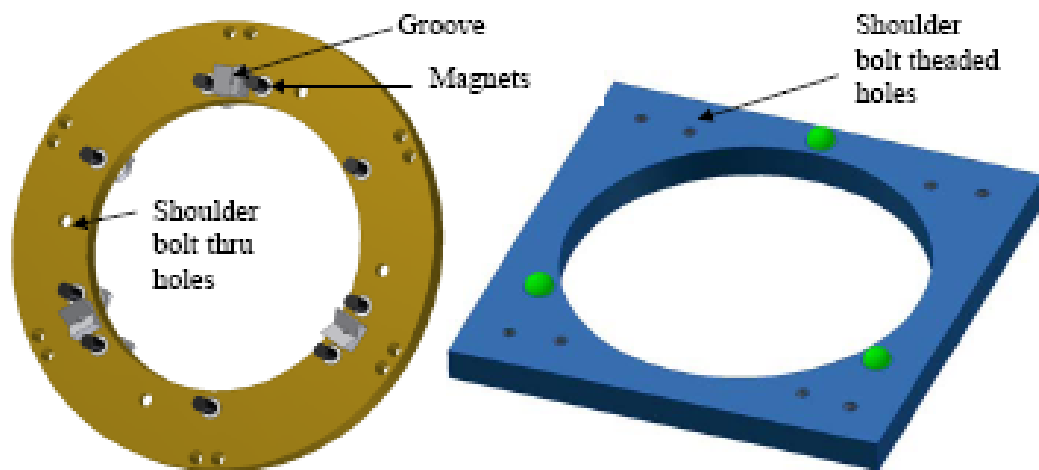


Figure 5.10 Magnetic kinematic ball-and-groove interface plates for repeatable CRO installation and removal. The 6 points of contact between the balls and grooves minimally constrain the CRO orientation and the magnets provide a repeatable loading force, independent of torques on screws. The shoulder bolts ensure that the plate does not fall off if it loses contact with the magnets.



degrees of freedom of the CRO (of which only the three degrees of translation are critical).

Six magnets that attract the adjacent steel plate provide the loading force for our ball-and-groove interface. This repeatable loading force and kinematic ball/groove interface allow us to achieve a highly repeatable interface by simply removing and replacing the CRO plate without realignment after each iteration. The mount is repeatable to our measurement accuracy, which is approximately 0.5 mm. When the CRO plate is removed, a hole in the CRO truss structure allows light from a real star to pass through the intermediate focus.

### 5.3 Gun Laser and Alignment in the Tower

The 5-axis piezo stage has a very limited travel range of only a few mm. If the CRO is not already aligned to within a mm or two when the CRO is installed, then the alignment cannot be achieved. During the shipping from Arcetri to Chile, the entire truss assembly was removed from the ASM wind screen, with several bolted interfaces removed that were not designed to necessarily be repeatable upon reassembly (Figure 5.11 shows a photo of the reassembled CRO truss and ASM in Chile). Therefore, in order to maintain some fiducial of the precision CRO alignment that we had achieved in the Arcetri test tower, we designed a very compact mount for a small (U.S. quarter-sized) laser (Figure 5.12). This laser had to be small, robust, have internal adjustable tip/tilt that would keep its alignment when bumped, be battery powered, and be rail mounted. These are coincidentally the same design requirements as a handgun laser, which is what we ultimately decided to use.



Figure 5.11 The ASM with the CRO truss assembly attached in Chile. The delrin cap in the center of the ASM is the mounting place for the boresight gun laser. The CRO has been removed, so the ellipsoidal conjugate is unobscured and light can pass through the hole in the center of the truss spider.

This laser mounts to a delrin surface at the very center of the ASM itself, in the region shadowed by the telescope's central obscuration. The laser beam fires straight down the optical axis from the center of ASM, where the vertex would be, to the short ellipsoidal conjugate (Figure 5.13). When the CRO is in place, the laser enters to the entrance to the CRO cup. At the telescope during commissioning, the laser will also be used as a convenient boresight reference during the installation of the ASM.

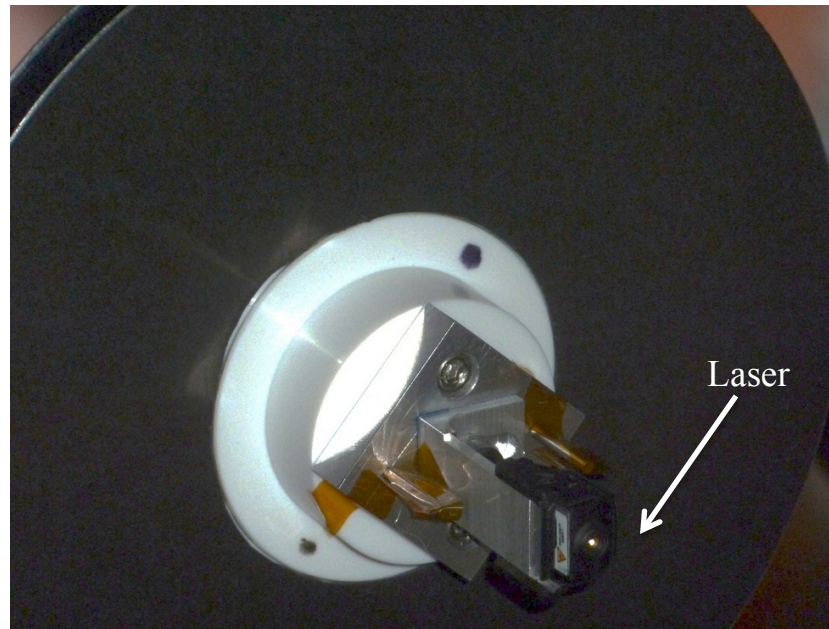


Figure 5.12 The LaserMax rail mounted handgun laser mounted to a delrin cap at the center of the ASM. The laser acts as an optical axis boresight reference and is also used to verify the location of the CRO after truss removal and installation.



Figure 5.13 The CRO cup mounted to its piezo stage and magnetic kinematic mount. The boresight laser is shining directly into the hole in the CRO return flat, indicating a good alignment. This view is the reflection in the ASM. The author is adjusting the coarse alignment bolts on the CRO stage.

## CHAPTER 6

### DESIGN OF A 20 MAS FIBER ARRAY IFS FOR THE VISAO CAMERA

*This chapter contains work that was originally published in the Proceedings of the SPIE Volume 7736 in 2010 by Kopon, D., Close, L.M., Males, J., Gasho, V., and Follette, K. All optical designs presented in this section are my original work.*

A possible future upgrade path for the Magellan AO system is the addition of a visible wavelength Integral Field Spectrograph at the VisAO focal plane. With this upgrade, the VisAO camera will be able to operate as either an imager, using the CCD47 with 8.5 mas pixels, or as an IFS, using a custom fiber array at the focal plane with 20 mas elements in its highest resolution mode. In imaging mode, the VisAO camera will have a full suite of filters, coronagraphic focal-plane occulting spots, and SDI prism/filters. The imaging mode should provide ~20% mean Strehl diffraction-limited images over the band 0.5-1.0  $\mu\text{m}$ . In IFS mode, the VisAO instrument will provide  $R \sim 1,800$  spectra over the band 0.6-1.05  $\mu\text{m}$ . Our unprecedented 20 mas spatially resolved visible spectra would be the highest spatial sampling achieved to date, either from the ground or in space.

#### 6.1 Introduction: Magellan Visible Adaptive Optics, Imaging, and IFS

Visible light reflected by the focal plane dichroic is sent to the W-Unit, which holds both the pyramid WFS and the VisAO camera/IFS. The VisAO imaging mode is designed to work from 0.5-1.0  $\mu\text{m}$  and the IFS from 0.6-1.05  $\mu\text{m}$ .

The high actuator count of our ASM will allow us to obtain modest Strehls ( $\sim 20\%$ ) in the visible ( $0.5\text{-}1.0\ \mu\text{m}$ ). Because the Vis AO camera is integrated into the WFS stage, we can select a beam splitter to steer a percentage of the WFS visible light into the Vis AO camera with  $8.5\ \text{mas}$  pixels. This capability allows us flexibility in choosing how much light to send to either the VisAO camera or the WFS, depending on guide star magnitude, seeing conditions, and science goals, while simultaneously observing in the IR with BLINC/MIRAC4 or CLIO2. The visible science light can either go to the CCD47 for imaging or 99% can be directed to a fiber bundle that has both coarse and fine plate scales for IFS spatially resolved spectroscopy. See Figure 6.1 for the fiber bundle schematic.

The VisAO camera will have the option either to make visible AO images with the CCD47 and  $8.5\ \text{mas}$  pixels, or to take spatially resolved spectra in IFS mode with  $20\ \text{mas}$  fiber elements. In either case, IR science can simultaneously be performed with the CLIO2 instrument. The fine spatial and spectral ( $R\sim 1,800$ ) resolution of the fiber-fed IFS will open a window to a panoply of science, such as studying emission lines in the visible in the inner regions of Herbig Ae/Be disks, resolving tight astrometric binaries, mapping the surface of Titan, etc. For a more detailed discussion of the science capabilities and motivations for the VisAO IFS, see Follette et al. 2010.

## 6.2 The Integral Field Spectrograph Design

Our IFS design takes advantage of our  $4\text{-}8\ \text{arcsec}$  diameter AO corrected isoplanatic patch. A removable beamsplitter will direct light towards a custom  $26\times 26$  array of multi-mode optical fibers spaced with  $160\ \mu\text{m}$  pitch (Figure 6.1). A microlenslet array

positioned in front of the bundle will improve our fiber coupling efficiency and give us a fill-factor of  $\sim 99\%$ . These fibers will transmit  $0.6\text{--}1.05\ \mu\text{m}$  light from the AO corrected focal plane to LDSS3, a wide-field red-sensitive Magellan facility spectrograph (Figure 6.2).

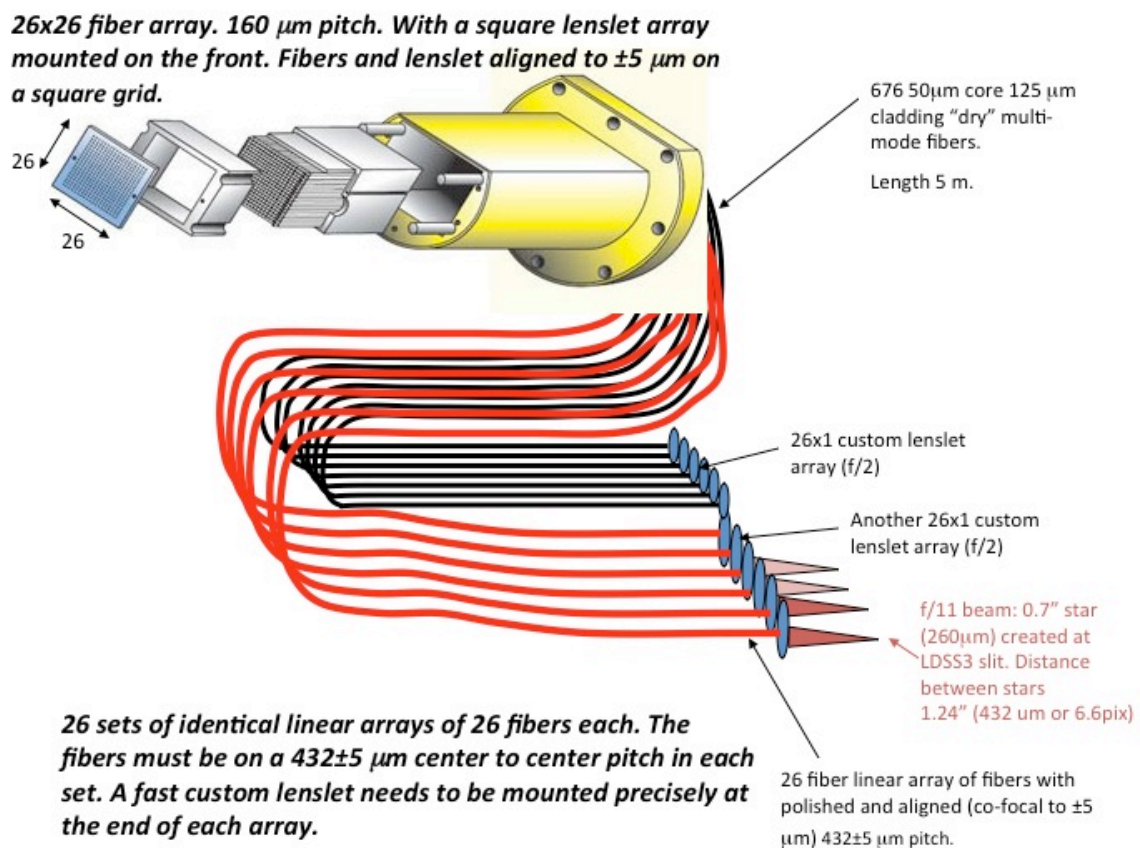


Figure 6.1 IFS Schematic. A 26x26 array of fibers takes light from the VisAO focal plane to the LDSS3 spectrograph where the fibers are coupled to the wide-field LDSS3 slit. Figure courtesy of Laird Close.



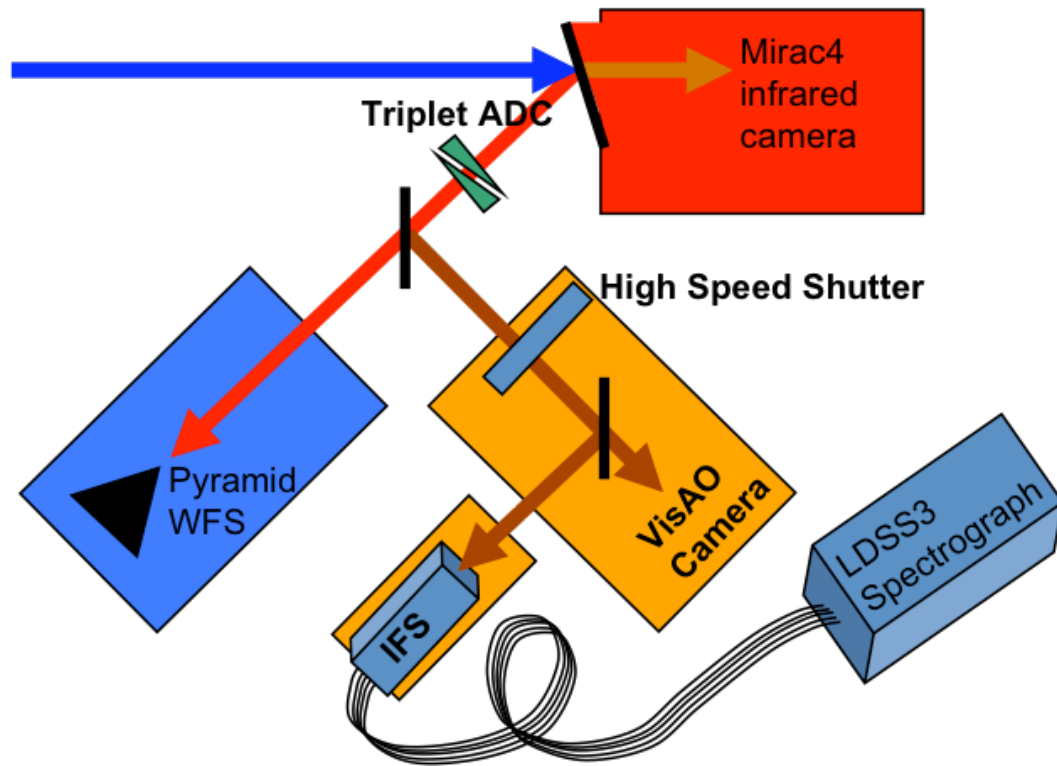


Figure 6.2 IFS and VisAO block layout. AO corrected light is split by a dichroic and a beamsplitter between the MIRAC4 IR science camera, the pyramid WFS, and the VisAO science instrument that has the option of sending light to the fiber-fed IFS.

The IFS mode will have two different plate scales: 20 mas/pixel and 105 mas/pixel. In order to slow the beam down enough to transition from 105 mas/pix to 20 mas/pix (F/49 to F/225) we have designed two custom triplet lenses that will swing into the beam when fine 20 mas spectral imaging is desired (see Figure 6.3). The first triplet will be interchangeable with and in the same location as the Wollaston prism. The second triplet will be captured inside the baffle tube that holds the beamsplitter that folds the beam up to the fiber bundle. These two optics acting together will allow us sufficient optical leverage to slow the beam down enough to reach our desired plate scale while still

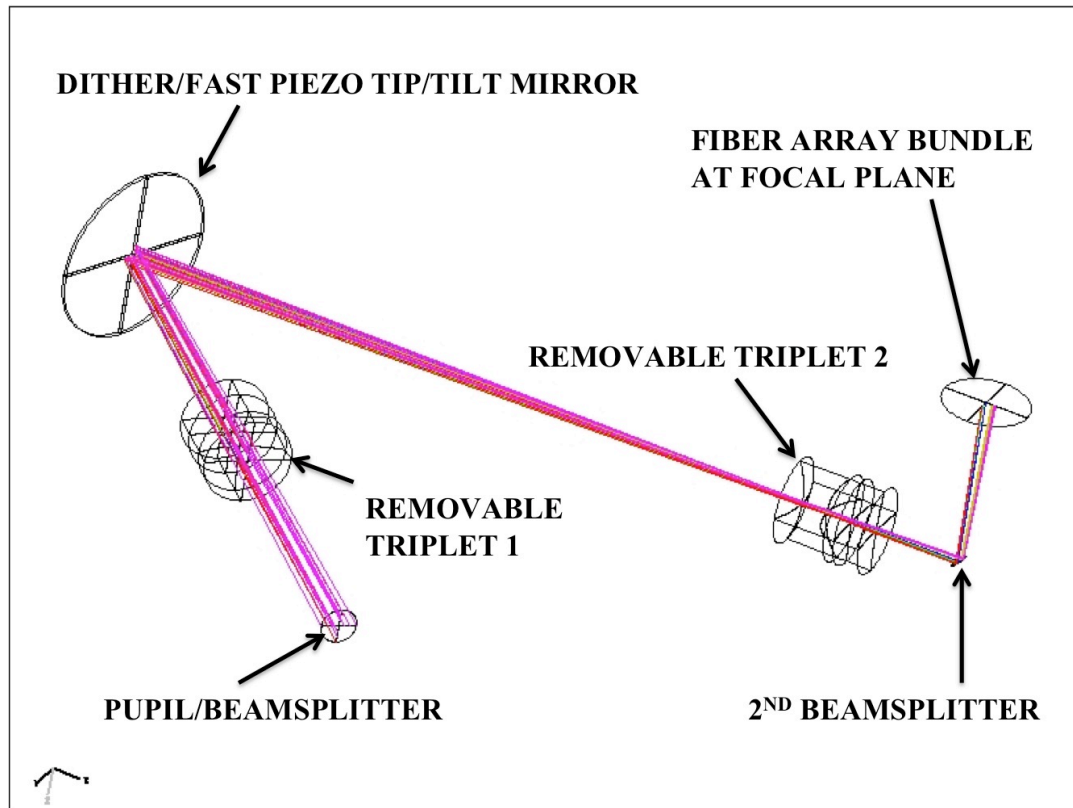


Figure 6.3 Raytrace of the 20 mas mode of the VisAO IFS from the W-unit beamsplitter to the IFS fiber focal plane. The first and second triplets can move in or out of the beam to switch between the F/225 20 mas mode and the F/49 105 mas mode.



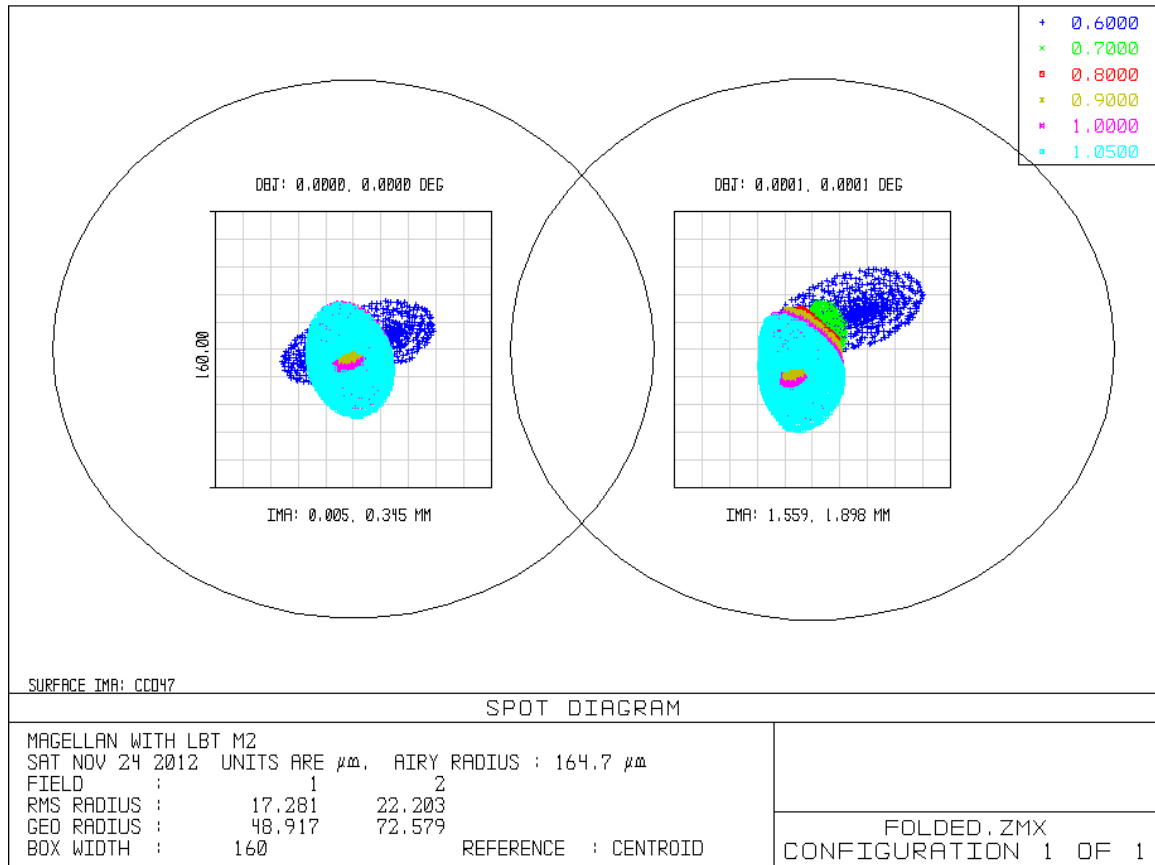


Figure 6.4 Spot diagrams of the VisAO focal plane (fiber entrance) in 20 mas mode. The slightly elongated ellipses are the first Airy minimum at 600 nm and the squares are the size of a lens element (160  $\mu\text{m}$  x 160  $\mu\text{m}$ ). The first airy minimum at 600 nm is slightly elliptical because of the elongation of the PSF due to astigmatism. The spot diagram on the left is on-axis and the right is the edge of the field (corner of the 26x26 square array) at 367.7 milliarcsec.

keeping optical and chromatic aberrations below the diffraction limit over the full waveband. For the raytrace and spot diagrams of the two-triplet fine plate scale optical design, see Figures 6.3 and 6.4. The 20 mas/pix mode will be the highest resolution visible IFS instrument in the world. The coarser 105 mas/pixel plate scale will be used as a “faint object” mode for science targets too faint to be detected in the 20 mas/pixel mode.

Another optical design challenge presented by the VisAO IFS is the coupling of the output end of the fibers with the input slit of LDSS3. Typical high numerical aperture fibers have an output f-ratio of  $\sim F/2-3$ . The LDSS3 slit has an input focal ratio of  $F/11$ . In order to couple this fast fiber output with the slower slit input, we have designed a two-sided aspheric lenslet array. This lenslet array is made of fused silica and is within reasonable lithographic fabrication constraints, which are chiefly governed by the maximum sag of the lens profile. The raytrace of an element of our custom aspheric lenslet array is shown in Figure 6.5.

The IFS will be the focus of an MRI proposal in 2014.

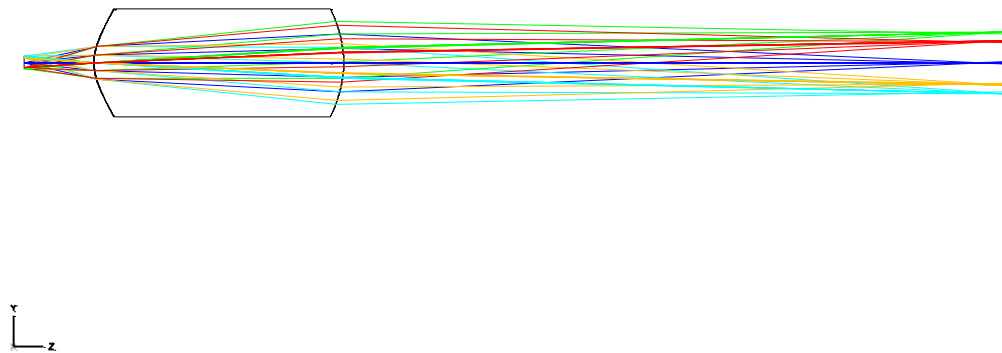


Figure 6.5 Our custom aspheric output lenslet design that will couple the  $\sim F/2.5$  output of the IFS fibers to the  $F/11$  LDSS3 slit. This design helps us to avoid Focal Ratio Degradation (FRD) issues with the fiber output.

## APPENDIX A

### STRAY LIGHT ANALYSIS AND MITIGATION

*This section contains work presented in the MOAP-004 Magellan CDR design document.*

#### A.1 W-Unit and VisAO Ghosts

All of the refractive optics in the VisAO arm of the W-unit are potential sources of ghosts. This includes the input lens, the ADC, the beamsplitter, the filters, and the coronagraphic spots. The input lens, the ADC, and the coronagraphic spots will be AR coated to better than  $R < 0.01$ . In addition, ghosts originating in the ADC or the input lens will be out of focus by  $2\times$  the thickness of the element, which for both elements is on the order of  $\sim 20\text{mm}$ . Hence, any ghosts should not be focused point sources. However, our analysis shows that all bright ghosts can be blocked by our  $1.0''$  diameter coronagraphic spot.

The filter wheel will be tilted sufficiently to move any filter ghosts far outside of the FOV. The ghost from the beamsplitter could be mitigated by using a wedge. However, past experience has shown that a focused, well-understood beamsplitter ghost can be useful for astrometry and photometry since the central bright star will be obscured by the coronagraphic spot. Having a beamsplitter ghost of the central bright target star near the edge of the VisAO FOV is somewhat analogous to using an ND3 neutral density filter. This off-axis source can then be used to perform accurate astrometry on the central star when it is saturated (or behind the coronagraphic mask). The coronagraphic spot will be

chrome deposited on the side of the glass facing the CCD47 (for more on the fabrication of such spots see Park & Close 2006).

In summary, all “in-focus” ghosts will be hidden behind our coronagraphic spot while out-of-focus ghosts larger than 1.0” will be  $>10,000\times$  fainter than the halo level past the spot --and so they will be too faint to be a significant source of noise.

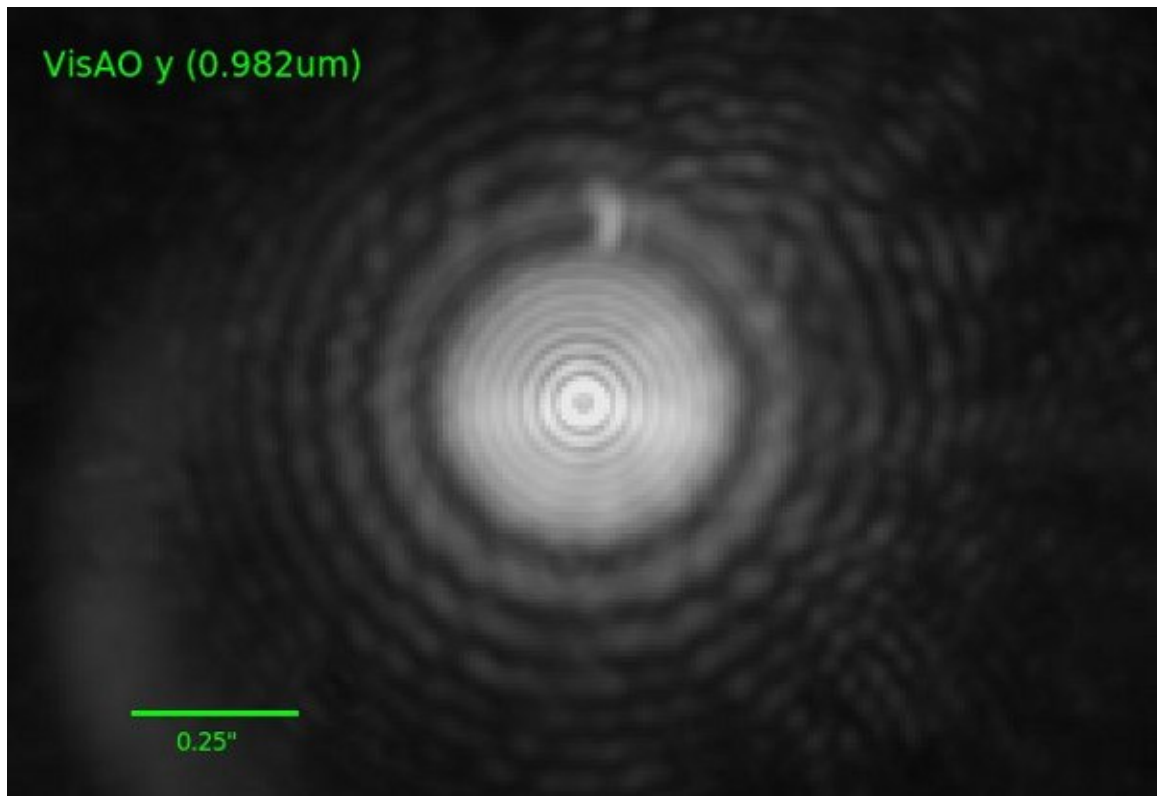


Figure A.1 Image taken with coronagraphic occulting spot blocking the y-band PSF.

## A.2 Baffling

The entire W-unit will be shrouded in lint-free synthetic black cloth that will block external stray light, such as moonlight. In addition, tubes, vanes, and snouts will be used wherever possible, particularly near the CCD47, to reduce stray light. The coronagraphic

spots will be tilted by 5 degrees to send the blocked (reflected) light into the optical baffle near the shutter. The unit has proven to be light tight at the telescope.

### A.3 Detailed Ghosting Analysis

We performed a full ghosting evaluation of the W-unit optics in the CCD47 optical channel at 750 nm wavelength using the Zemax ghost focus generator. The ghost focus generator calculates the double and single-bounce ghosts produced by light reflected off of refractive elements. Our analysis looked at all double bounce ghosts off of all refractive elements surfaces and interfaces. For each potential ghost a new Zemax model was created that could be used to generate spot diagrams, ghost location, F/#, etc. In order of first to last in the optical path, the relevant refractive optics are the telecentric lens, the input lens, the two ADC elements, the flat piece of glass that contains the coronagraphic spots, and the first surface of the CCD. Other refractive optics, such as the filters, are not considered, since these elements can be tilted easily so that the ghost does not fall on the detector. Ghosts whose first or second bounce included one of the tilted surfaces in the ADC were not considered, since these ghosts are also reflected well away from the detector.

Table A.1 lists all of the possible permutations of double bounce ghosts. The location of the ghost focus relative to the detector along the optical axis is given in mm. The rms spot size of the ghost on the detector surface is given in mm. An 'X' is placed next to any ghost sufficiently in focus to merit a second look. No significant ghosts are generated that have either the Telecentric or input lens as the first or second bounce. A few ghosts are generated between the flat front and back of the ADC elements. These

ghosts can be mitigated by slightly tilting the ADCs. Focused ghost are generated by the coronagraphic plate, which is modeled in Zemax by a flat piece of BK7. However, in actual practice, the coronagraphic spots themselves will block any these “X” ghosts. Indeed, our design will use these ghosts to align each element to be true to the optical axis. In this manner a bright star will have all its “in-focus” ghosts blocked by the coronagraphic spot.

All of the refractive optics in the CCD47 arm of the W-unit will have the Optimax “precision quality” broad-band optical anti-reflection coating, which has a reflectance of  $R < 0.5\%$ . Therefore, any in-focus double-pass ghost would have an intensity of 0.0025% at the detector (out of focus ghosts quickly become undetectable). Indeed, all of the ghosts are out of focus to some extent at the detector, so the attenuation is even greater. Any ghost large enough to surpass our 1.0” spot will have just  $1 \times 10^{-8}$  the intensity of the central pixel. This is a very light level, the halo flux level 0.5” off axis is  $\sim 10,000\times$  brighter than ghost intensity/pixel.

There is one ghost that cannot be hidden behind the coronagraphic mask. That is the off-axis ghost created by an internal reflection inside the 5mm thick 22.5 degree beamsplitter. This  $\sim 2.5$ ” off-axis ghost will actually be a useful astrometric tool when the guide star is behind the spot or is badly saturated, it will be typically  $\sim 1 \times 10^{3-4}$  times fainter than the central star. The absence of ghosts is now verified by our tower test results, such as the image shown earlier in Figure 3.14.

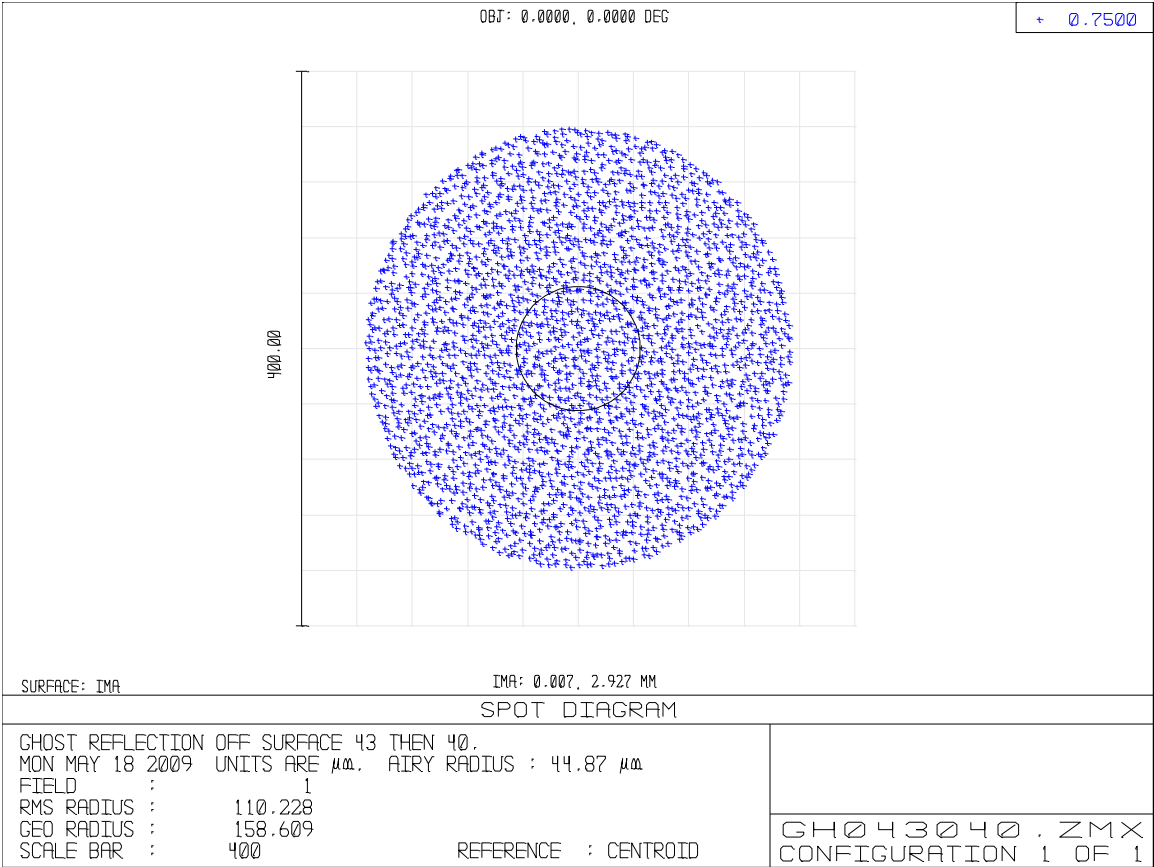


Figure A.2 Example of an out-of-focus ghost at the focal plane generated by the double-bounce reflection between the front and back of the first ADC element. Note that the final “image” of the spot has been reduced in pixel intensity to  $\sim 1 \times 10^{-7}$  that of a central pixel of the original image on the same detector plane. Also note that this Ghost image has a rms radius of just 0.110 mm (0.071”) and so it will be 100% blocked by our 1.0” coronagraphic spot that will needed to make any high dynamic range image.

Table A.1 VisAO Ghosts

surface names:

- 31 telecentrica front
- 32 telecentrica back
- 34 input lens front
- 35 input lens interface
- 36 input lens interface
- 37 input lens back

- 40     ADC1 front  
 41     ADC interface  
 42     ADC interface  
 43     ADC1 back  
 46     ADC2 front  
 47     ADC interface  
 48     ADC interface  
 49     ADC2 back  
 52     coronagraph front  
 53     coronagraph back  
 54     detector face  
 X     indicates a focused ghost

First Bounce Surface	Second Bounce Surface	Z-distance from image surface [mm]	Rms spot radius at focal plane [mm]	notes
----------------------	-----------------------	------------------------------------	-------------------------------------	-------

32	31	122.9882	1.12E+00	
34	31	1.36E+04	9.23E+00	
	32	1544.664	1.25E+01	
35	31	687.167	8.37E+01	
	32	641.5505	9.44E+01	
	34	532.3969	1.63E+02	
36	31	300.7009	7.09E+00	
	32	275.2925	5.68E+00	
	34	469.8544	2.99E+01	
	35	541.3881	1.70E+02	
37	31	645.9873	4.68E+01	
	32	612.1133	5.18E+01	
	34	524.7565	9.12E+01	
	35	562.72	5.30E+01	
	36	505.9583	8.47E+01	
40	31	519.5109	1.48E+01	
	32	509.8484	1.54E+01	
	34	502.8744	3.55E+01	



	35	544.6016	8.51E+01	
	36	469.2981	2.06E+01	
	37	562.7407	3.65E+01	
43	31	520.5071	1.43E+01	
	32	510.7328	1.49E+01	
	34	503.0381	3.41E+01	
	35	544.6358	8.12E+01	
	36	469.7192	1.99E+01	
	37	562.935	3.48E+01	
	40	14.1978	1.08E-01	X see Fig. A.1
46	31	520.7018	1.42E+01	
	32	510.9055	1.47E+01	
	34	503.0701	3.38E+01	
	35	544.6425	8.05E+01	
	36	469.8012	1.97E+01	
	37	562.9734	3.45E+01	
	40	16.9978	1.29E-01	X
	43	1.9725	2.03E-02	X
49	31	521.8003	1.36E+01	
	32	511.8789	1.42E+01	
	34	503.2507	3.24E+01	
	35	544.6807	7.67E+01	
	36	470.2614	1.90E+01	
	37	563.1922	3.28E+01	
	40	32.0231	2.37E-01	X
	43	16.9978	1.29E-01	X
	46	14.1978	1.08E-01	X
52	31	476.9934	1.82E+01	
	32	470.7705	1.84E+01	
	34	496.0105	4.80E+01	
	35	543.4491	1.51E+02	
	36	447.9243	2.24E+01	
	37	556.6503	6.59E+01	
	40	887.3738	6.40E+00	
	43	872.3485	6.29E+00	
	46	869.5485	6.27E+00	
	49	854.5232	6.16E+00	
53	31	476.8977	1.81E+01	
	32	470.6795	1.83E+01	
	34	495.9953	4.77E+01	
	35	543.447	1.50E+02	
	36	447.8673	2.23E+01	

	37	556.6402	6.55E+01	
	40	884.728	6.38E+00	
	43	869.7027	6.27E+00	
	46	866.9027	6.25E+00	
	49	851.8774	6.14E+00	
	52	-3.4733	1.92E-02	X
detector face (54)	31	476.5267	1.77E+01	
	32	470.3267	1.79E+01	
	34	495.9364	4.67E+01	
	35	543.439	1.47E+02	
	36	447.6458	2.18E+01	
	37	556.6009	6.44E+01	
	40	874.728	6.31E+00	
	43	859.7027	6.20E+00	
	46	856.9027	6.18E+00	
	49	841.8774	6.07E+00	
	52	-13.4733	9.12E-02	X
	53	-10.8275	7.21E-02	X

## APPENDIX B

### ALTERNATIVE WIDE-FIELD LENS DESIGN

*This design was first presented by Kopon et al. in the Proceedings of the SPIE 2008.*

In the early design phase of the VisAO channel of the W-Unit, we designed a wide-field lens tube that could be placed in between the tip/tilt dither mirror and CCD47 in order to widen the field of view for acquisition or wide-field science. Because the pupil and its surrounding area were already crowded with many optical elements (such as the ADC, beamsplitters/dichroics, the Wollaston prism, etc.) we were forced to locate the lens tube farther from the pupil and nearer the CCD47. In addition, we required that the lens tube be affordable to fabricate and create no focus shift because of the limited range of our CCD47 focus stage. After much iteration, we were able to meet all the design requirements. Ultimately, we chose to occupy this space on the W-unit board with other important components, such as the fast shutter. We opted to instead use the guider probe design presented in Chapter 4 for 50'' wide-field capability. However, we present the design here for completeness.

In this design, the EEV CCD47 of the W-unit will serve as both a narrow field (8.6'' FOV) science camera for visible AO and a wide field (28.5'' FOV) acquisition camera. Because of the fixed position of the CCD47 and the tight geometry of the W-unit board (Figure 2), we were forced to design a removable lens that would fit between the final fold mirror and the focal plane. Typically, a lens of this type is more naturally located

near a pupil. Because of the large distance from the pupil, our lens elements must have large (3") diameters and higher curvatures than most stock lenses.

Our wide-field design is diffraction limited over the band 0.8-1.0  $\mu\text{m}$  in the inner  $\sim 20''$  diameter circle of the CCD, which is the largest possible isoplanatic patch we would ever expect to have at 1.0  $\mu\text{m}$ . The field over the rest of the CCD outside of this well-corrected inner patch is not diffraction limited, yet is still much better than a seeing-limited spot of  $1''$ . By relaxing the image requirements on this outer portion of the field, we were able to generate a relatively inexpensive design that makes use of two stock Melles Griot achromats along with a custom negative doublet. The distortion of the lens is also small, with a maximum of 1.3% at the edge of the field. The wide field lens will be on a movable mount that will lift the lens into and out of the beam without requiring a focus shift at the detector. However, the CCD will be on a small precision translation stage with  $\pm 5$  mm travel in the z-direction in order to allow us to adjust focus. Figure B.1 shows the Zemax design of the Vis AO camera in wide-field mode, with the lens elements in place. Figures B.2 and B.3 show the spot diagrams of the Vis AO camera in both the wide-field mode and narrow-field mode at low zenith angle.

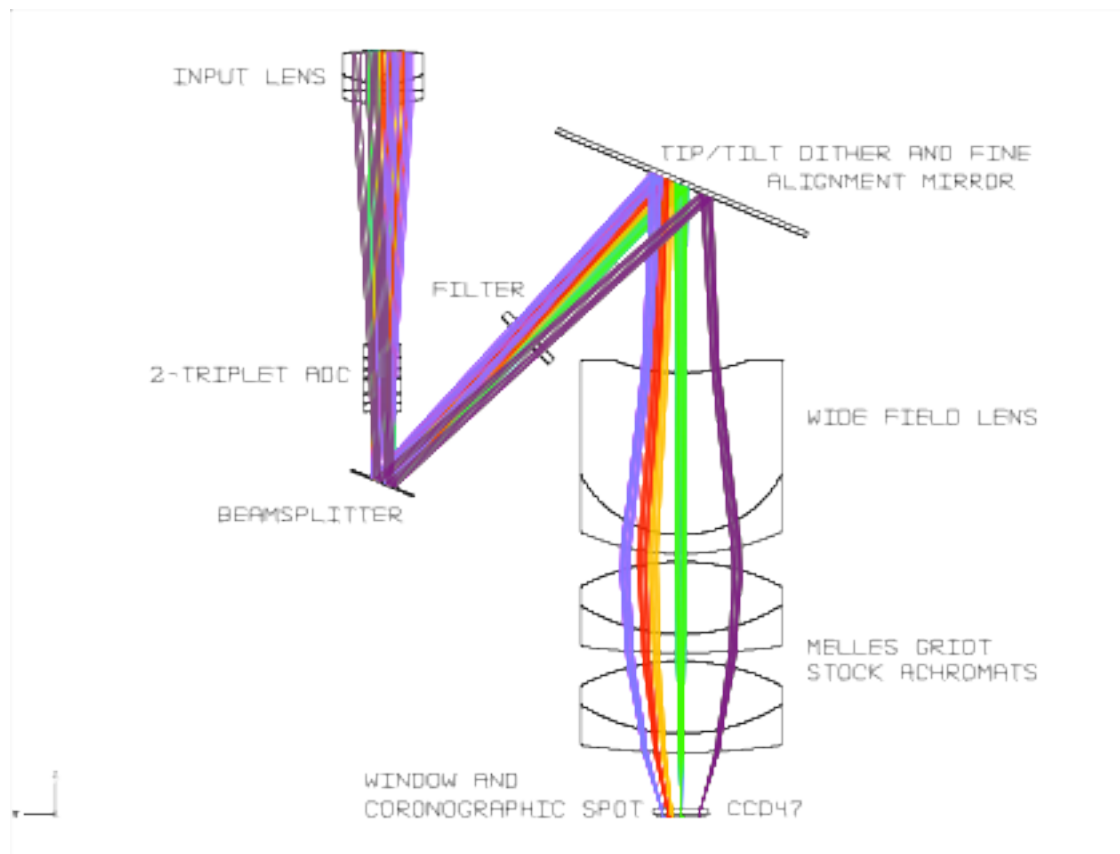


Figure B.1 The VisAO camera will have a three element removable wide field lens that can increase the FOV from 8.6" to 28.5". Two of the three elements are identical Melles Griot stock achromats.

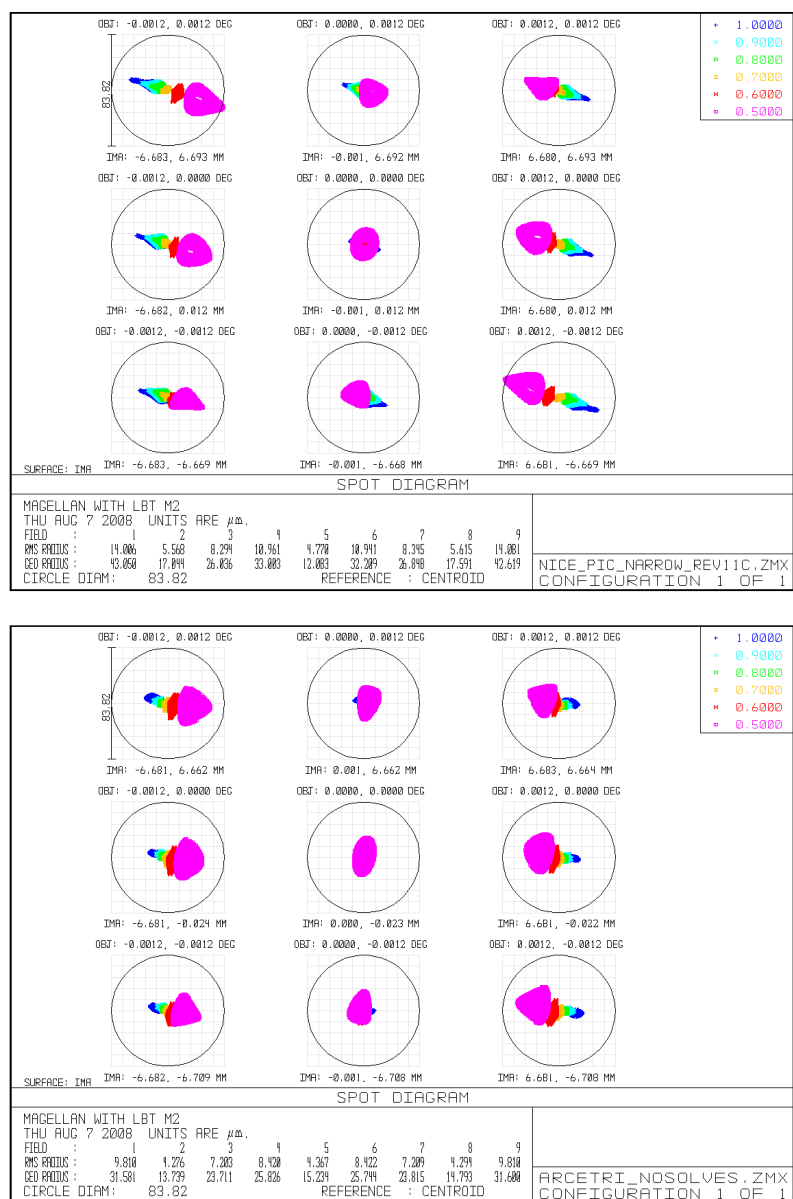


Figure B.2 The spot diagrams for the Vis AO CCD47 in narrow-field (8.6'' FOV) mode. The box at top contains the center and edge spots produced with the 2-triplet ADC design. The box at bottom contains the center and edge spots for the 2-doubling design. The variation in chromatism across the field is a residual caused by the ADCs themselves and does not vary with zenith angle. Both spot diagrams were made at 5° zenith to avoid zenith spike artifacts at 0° zenith. The circle shown is the diffraction limit for 0.7  $\mu\text{m}$ , which is the shortest wavelength at which we expect our AO system to be diffraction limited. While the spot diagrams for the 2-doubling ADC are slightly better than those of the 2-triplet design at this low zenith angle (see figure 7), the 2-triplet design outperforms the 2-doubling design at higher zenith angles and is therefore the design of choice for the Magellan AO system.

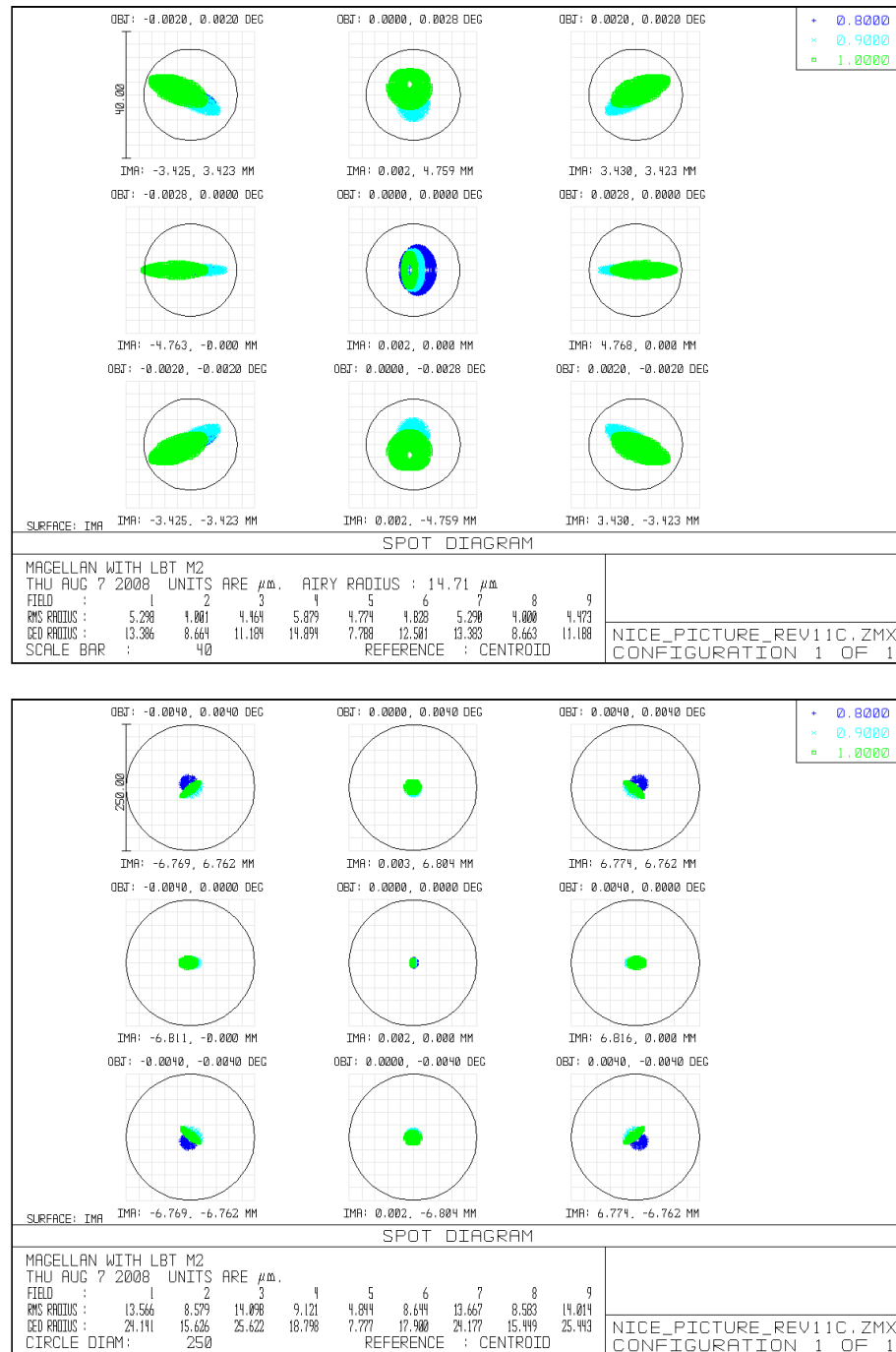


Figure B.3 The spot diagrams for the CCD47 in wide-field (28.5'') mode. The spot diagrams to the left are the center and edges of the inner 20'' circular patch, which is the largest possible isoplanatic patch on a good night. The circles are the diffraction limit at 0.8μm. The spots to the right are the center and edges of the entire 28.5'' FOV of the CCD47 with a 0.5'' diameter (250μm) seeing-limited circle for comparison. These plots were made with the 2-triplet ADC in place at 0° zenith angle.

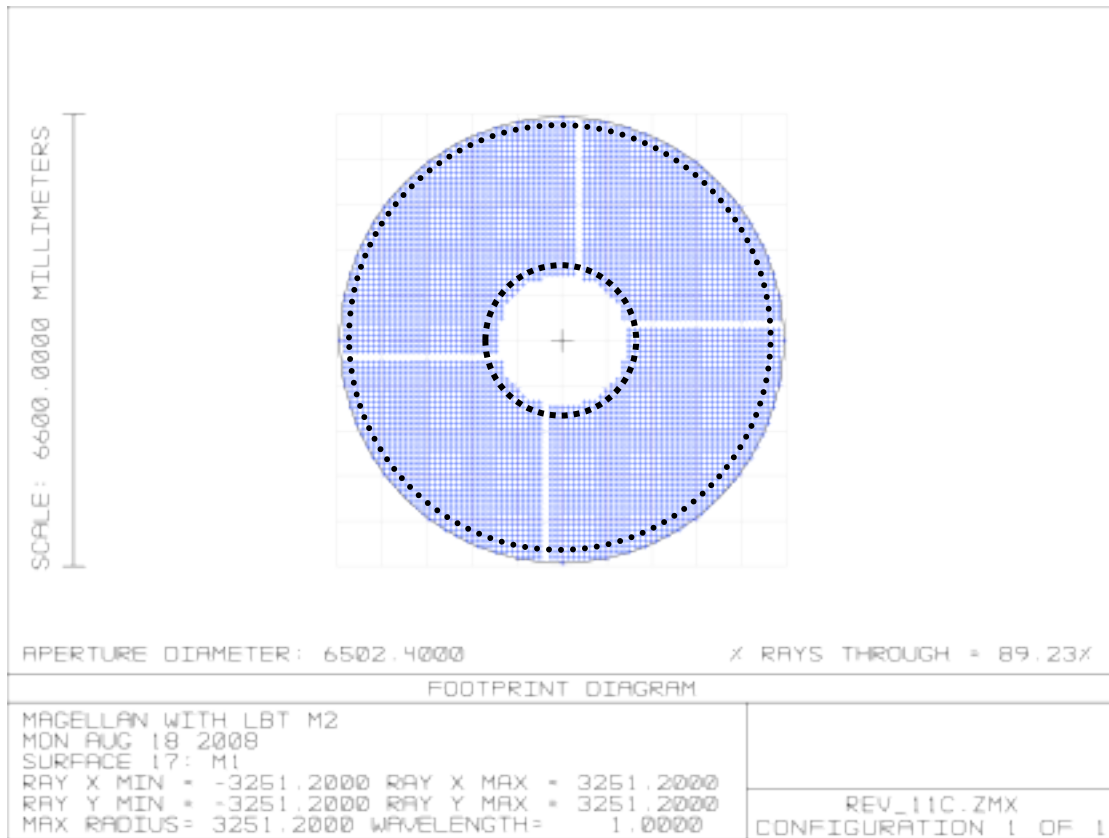


Figure B.4 Footprint diagram of the primary mirror, illustrating the shape of the telescope pupil. The central obscuration caused by the secondary cage and baffles is a circle with a diameter of 1.9 meters and the four spider vanes have a width of 12 mm (vanes shown thicker --not to scale). Dotted lines mark edges of the 5% undersized cold MIRAC pupil stop, which will limit system emissivity to only 1% above that of a sky baffled secondary.



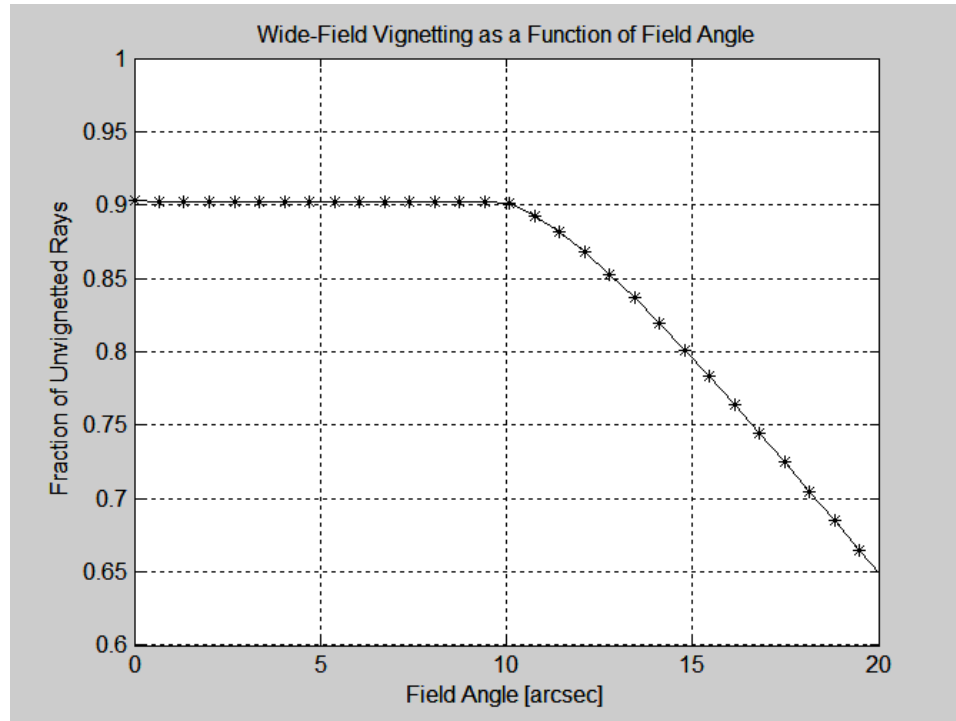


Figure B.5 The unvignetted CCD47 FOV is  $\sim 20''$ ,  $>2\times$  larger than required for the  $8.5''$  FOV of the Vis-AO camera .

## APPENDIX C

### QUARTZ AND CALCITE WOLLASTON DESIGNS

The tight geometry of the VisAO optical layout determined the location of the Wollaston prism, with very little room to maneuver. This location, combined with the size of the CCD47, mandated that we design a custom Wollaston with a  $1.15^\circ$  beam deviation angle. Any Wollaston prism will necessarily introduce both astigmatism and chromatic aberration into the beam. Our goal was to minimize these effects.

#### C.1 Introduction

A Wollaston prism is made from two birefringent crystals that have been cemented together such that their optical axes are perpendicular. A randomly polarized beam entering the prism will be split into two perpendicularly polarized beams whose angular deviation is determined by the material and cut angle of the prism.

Because the beam deviation angle is determined by both the cut angle of prism and the birefringence of the material, a given beam deviation angle can be met with either a weakly birefringent material and a large cut angle, or a strongly birefringent material and a shallow cut angle. We present designs for both scenarios: a quartz weakly birefringent ( $n_e - n_o = 0.009$ ) prism with a large ( $\sim 45^\circ$ ) cut angle and a calcite strongly birefringent ( $n_e - n_o = -0.172$ ) prism with a shallow ( $3.3^\circ$ ) cut angle.

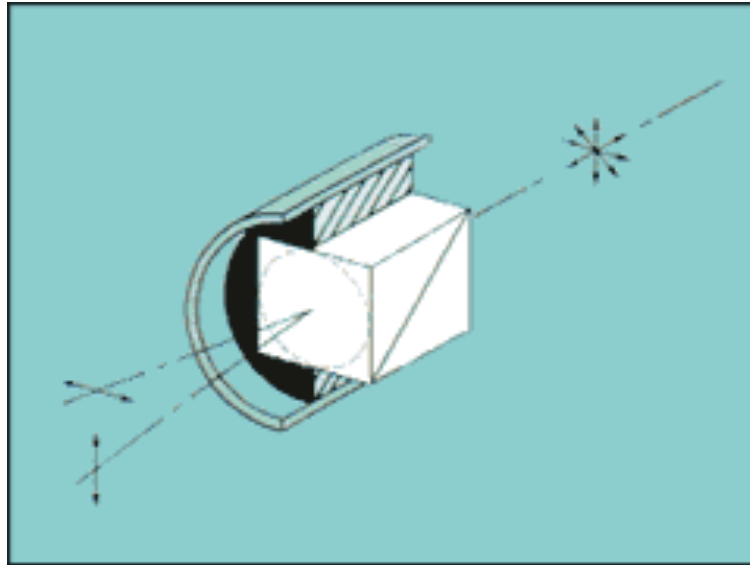


Figure C.1 An unpolarized beam enters from the right, passes through the Wollaston prism and is split into two perpendicularly polarized beams with a certain beam deviation angle. Figure taken from the [adphotonics.com](http://adphotonics.com) website.

## C.2 The Quartz Design

From a fabrication perspective, quartz is one of the easier birefringence crystals to work with, so there is some incentive to use this material, if possible. We designed a custom quartz Wollaston to fit our beam size. A photograph of this prism on its elevator mount is shown earlier in Figure 3.7.

The drawback of the quartz design is that the low level of birefringence in the material requires a large cut angle in order to meet our beam deviation spec. A large cut angle necessarily introduces astigmatism into the beam. In addition, the large cut angle requires the Wollaston to be thick (20 mm), which means that there will be a focus shift of several mm at the CCD47 focal plane when the Wollaston is raised into the beam. As Figure C.3 shows, the astigmatism is generally not the same for the two beams at a given

focal position and is not the same at the best focus. The astigmatism is roughly the same size as the diffraction limit and has a significant impact on the PSF.

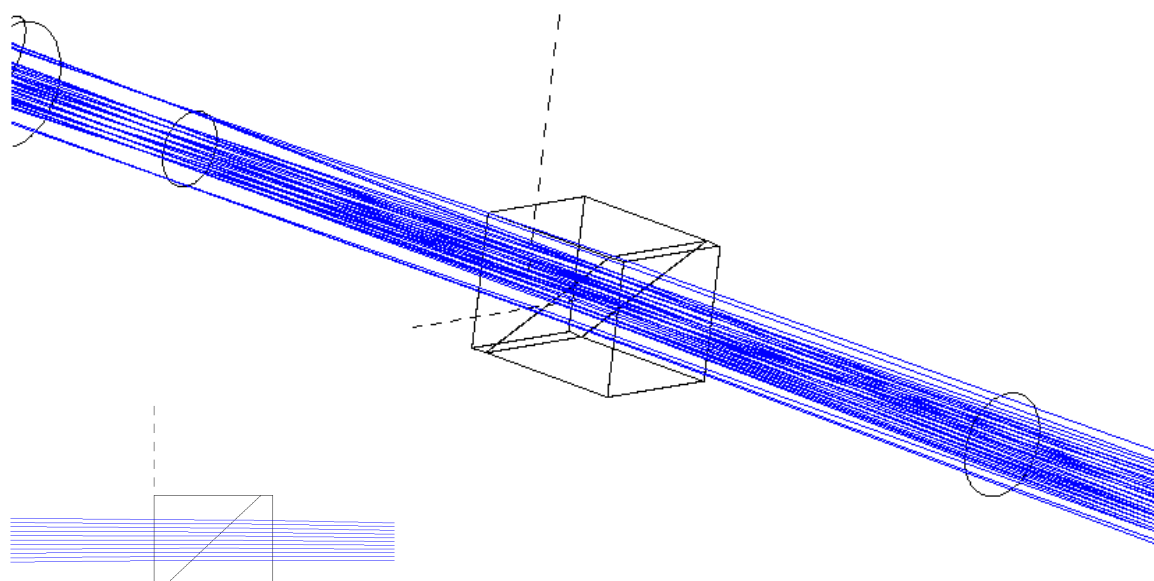


Figure C.2 Raytrace of the quartz Wollaston.

### C.3 The Calcite Design

The high birefringence of calcite allows for a design with less astigmatism, though more expensive and difficult to fabricate. The calcite design achieves the same beam deviation angle with a cut angle of only  $3.3^\circ$  compared to the  $\sim 45^\circ$  cut angle of the quartz Wollaston. In addition to reducing astigmatism, this shallow cut angle allows for a much thinner design and a correspondingly smaller focal shift at the CCD47. We went with a 6

mm thick design for fabrication purposes, but we could have gone even half that thickness in theory (although at greater fabrication risk and expense).

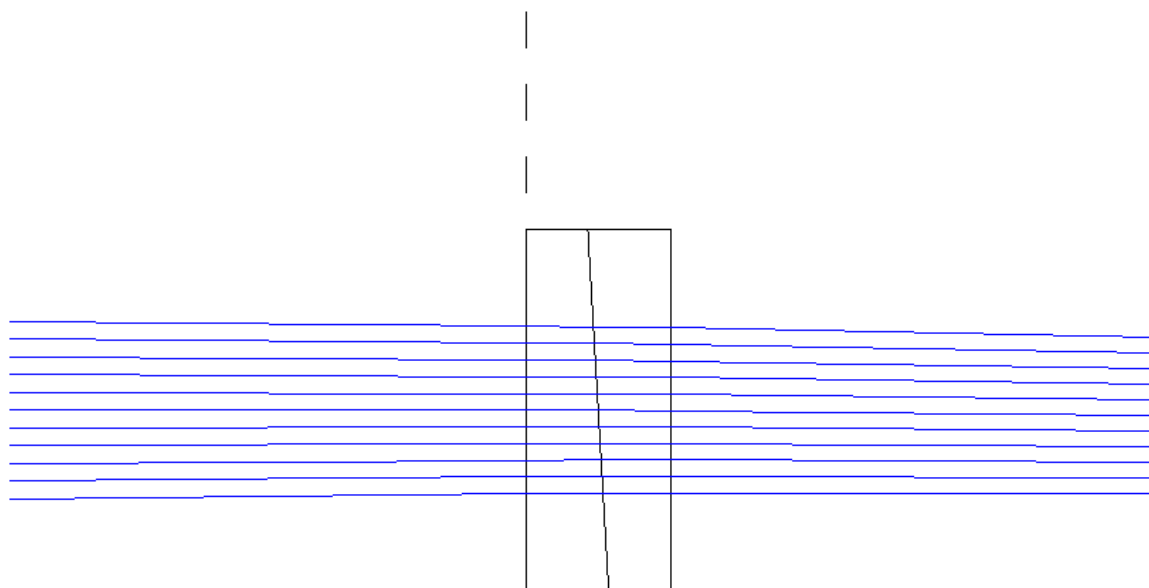


Figure C.4 Raytrace of the calcite Wollaston design.

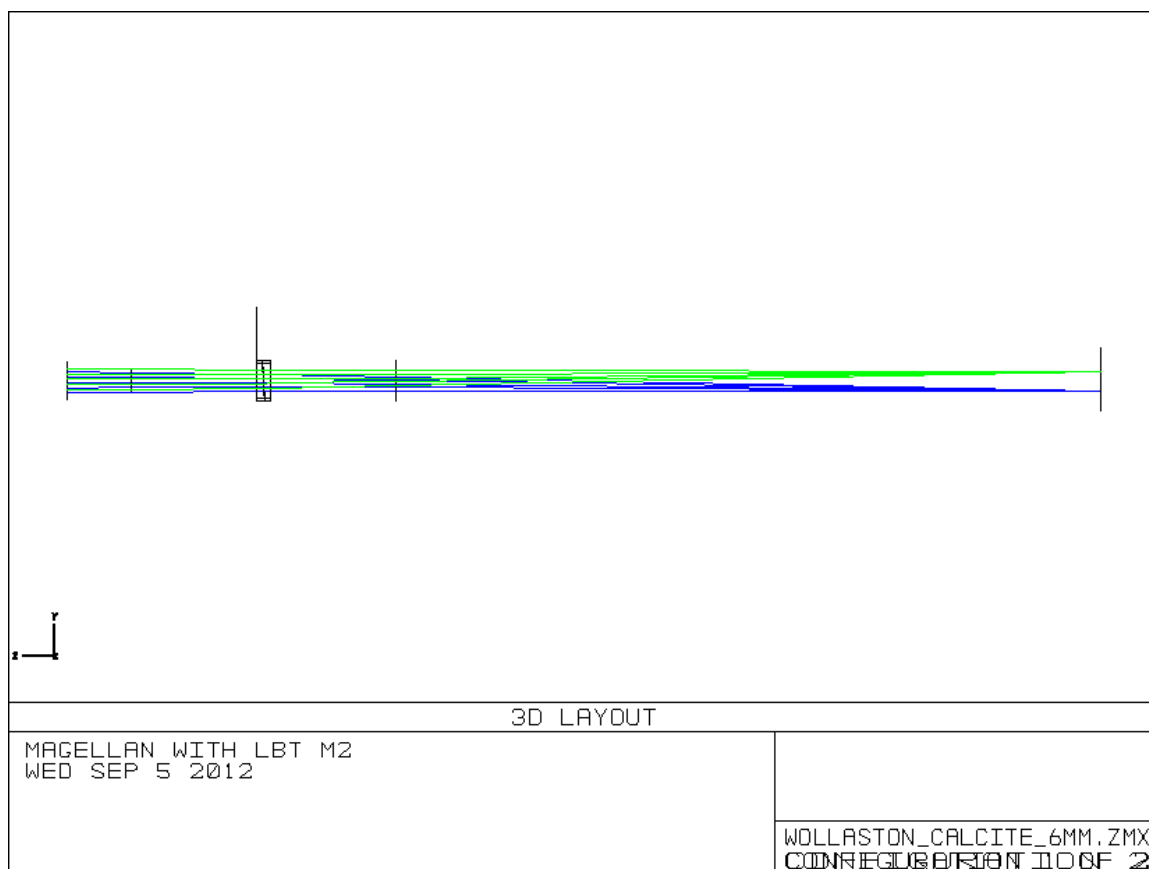


Figure C.5 Raytrace of the calcite Wollaston design showing both beams of opposite polarization. Light enters from the left, the CCD47 focal plane is at right.

#### C.4 Conclusion

The calcite design ultimately gives the better optical performance, but is costlier and much more difficult to fabricate than the quartz design. Because of this, we first procured an AR coated quartz Wollaston from a German company called Halle. The prism was made to spec and performed as expected, achieving the desired beam deviation but introducing a non-trivial and ultimately unacceptable amount of astigmatism into the beam.

After about a half-dozen no-bids, we finally found a British company, Leysop, that agreed to attempt to fabricate the calcite design on a best-effort basis. Because of its crystal structure, calcite can be difficult to polish and can change shape during the bonding required for a Wollaston. Leysop did eventually produce two pieces that were acceptable for our system. One of these is currently installed in the VisAO camera (see Figure C.7).

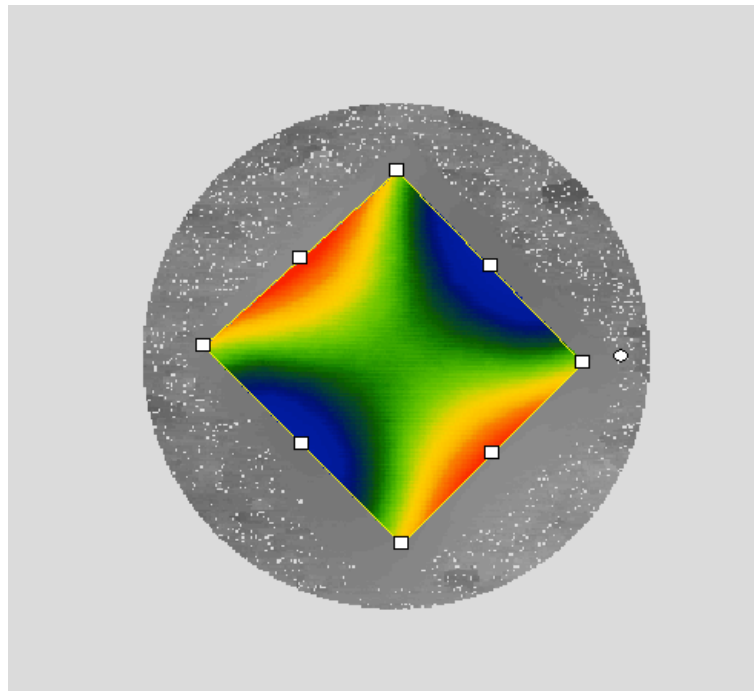
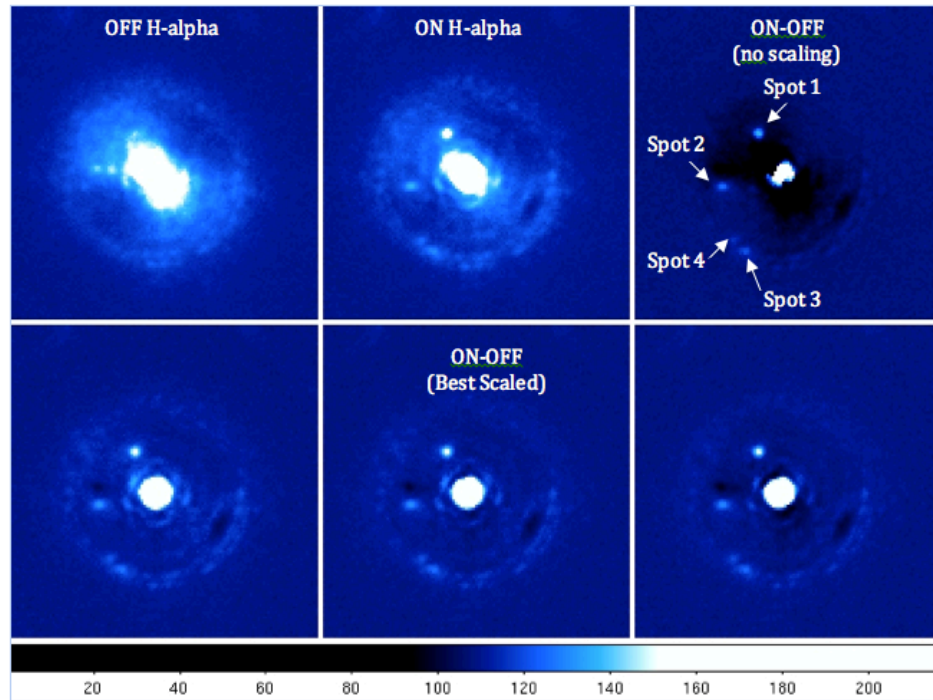


Figure C.6 Interferometric reflected surface map of one of the calcite Wollastons delivered by Leysop. There is significant ( $\sim 2/3$  of a wave P-V) astigmatism due to bonding stress. This is the worse of the two and is our spare. The other one is currently installed in the VisAO system and gives excellent images despite the bonding stress aberrations because of the small beam footprint and the fact that the optic operates in transmission.





	Spot 1	Spot 2	Spot 3	Spot 4
<b>H-alpha raw</b>	116	53	41	32
<b>ON-OFF Counts</b> (no scaling)	55	32	23	14
<b>% of raw H-alpha flux</b>	47%	60%	56%	44%
<b>ON-OFF Counts</b> (best scaled)	85	42	32	23
<b>% of raw H-alpha flux</b>	73%	79%	78%	72%
<b>Distance in pixels</b>	17.5	22	33	32
<b>Distance in arcsec</b> (1 pix=0.008'')	0.14''	0.18''	0.26''	0.26''
<b>Distance in AU</b> (@140pc 1pix=1.1AU)	19AU	24AU	36AU	35AU
<b>Contrast</b> (in magnitudes)	4.9	6.0	6.3	7.5

Figure C.7 SDI H $_{\alpha}$  images made with the calcite Wollaston showing contrast levels and simulated planets. Courtesy of Kate Follette.

## REFERENCES

- Biller, B., et al. 2007, ApJS, 173, 143
- Carbillet, M., et al. 2003, Proc. SPIE, 4839, 131
- Carbillet, M., et al. 2005, MNRAS, 356, 4
- Close, L.M., et al. 1995, ApJ, 439, 682
- Close, L.M., Gasho, V., Kopon, D., & Hare, T. 2009, MOAP-004 Optical Design Document for the Magellan Adaptive Optics System CDR
- Close, L.M., et al. 2005b, NATURE, 433, 286
- Close, L.M., et al. 2008, Proc. SPIE, 7015, 70150Y
- Close, L. M., et al. 2010, Proc. SPIE, 7736, 773605
- Close, L.M., et al. 2012, Proc. SPIE
- Esposito, S., et al. 2000, Proc. SPIE, 4007, 416
- Esposito, S., et al. 2001, A&A, 369, L9-L12
- Esposito, S., et al. 2008, Proc. SPIE, 7015, 70151P
- Esposito, S., et al. 2010, Proc. SPIE, 7736, 773609
- Esposito, S., et al. 2010, AO, 49, G174
- Fellowes, D. , 2006, “Kinematic and Quasi-Kinematic Constraints: What They Are & How They Work,” UA OPTI 521 course notes,  
<http://www.optics.arizona.edu/optomech/student%20reports/tutorials/FellowesTutorial11.pdf>
- Follette, K. B., et al. 2010, Proc. SPIE, 7735, 77351P
- Goncharov, A.V., Devaney, N., & Dainty, C., 2007, Optics Express, 15, 4

- Haubois, X., et al. 2009, A&A, 508, 923-932
- Kopon, D., et al. 2008, Proc. SPIE, 7015, 70156M
- Kopon, D., et al. 2009, Proc. SPIE, 7439, 74390Y
- Kopon, D., et al. 2010, Proc. SPIE, 7736, 77362V
- Kopon, D., et al. 2012, Proc. SPIE, 8447, 84473D
- Kopon, D., et al. 2012, PASP submitted
- Law, N.M., et al. 2006, A&A, 446, 739-745
- Law, N.M., et al. 2009, ApJ, 692, 24L
- Males, J.R., et al. 2010, Proc. SPIE, 7736, 773660
- Males, J.R., et al. 2012, Proc. SPIE, 8447, 844742
- Marois, C., et al. 2006, Proc. SPIE, 6269, 62693M
- Natta, A., et al. 2001, A&A, 371, 186
- Park, R., et al. 2006, PASP, 118, 159
- Perrin, G., et al. 2004, A&A, 418, 675
- Phillips, A.C., Miller, J., Cowley, D., & Wallaca, V., 2006, Proc. SPIE, 6269B, 62691O
- Racine, R., et al. 1999, PASP, 111, 587
- Riccardi, A., et al. 2008, Proc. SPIE, 7015-37
- Roggemann, M.C., & Meinhardt, J. A., 1993, JOSA, 10, 9
- Roddier, F. & Roddier, C., 1988, ESO Conference on Very Large Telescopes and the  
Instrumentation, 2, 667
- Schechter, P., et al. 2002, Proc. SPIE, 4837
- Schwarzschild, M., 1975, ApJ, 195, 137

- Sivanandam, S., et al. 2006, Proc. SPIE, 6269, 62690U
- Skemer, A.J., et al. 2009, PASP, 121, 882
- Tuthill, P.G., et al. 1997, MNRAS, 285, 529T
- Veran, J.P., et al. 1997, JOSA, 14, 11
- Wallner, E. & Wetherell, W., 1980, “Atmospheric Dispersion Correctors with Broad Spectral Bandpass for Large Telescopes,” in *Optical and Infrared Telescopes for the 1990's*
- Wynne, C.G., 1997, MNRAS, 285, 130